Nanopatterning of graphene guided by block copolymer self-assembly

Wang, Zhongli

Publication date:
2017

Document Version
Publisher's PDF, also known as Version of record

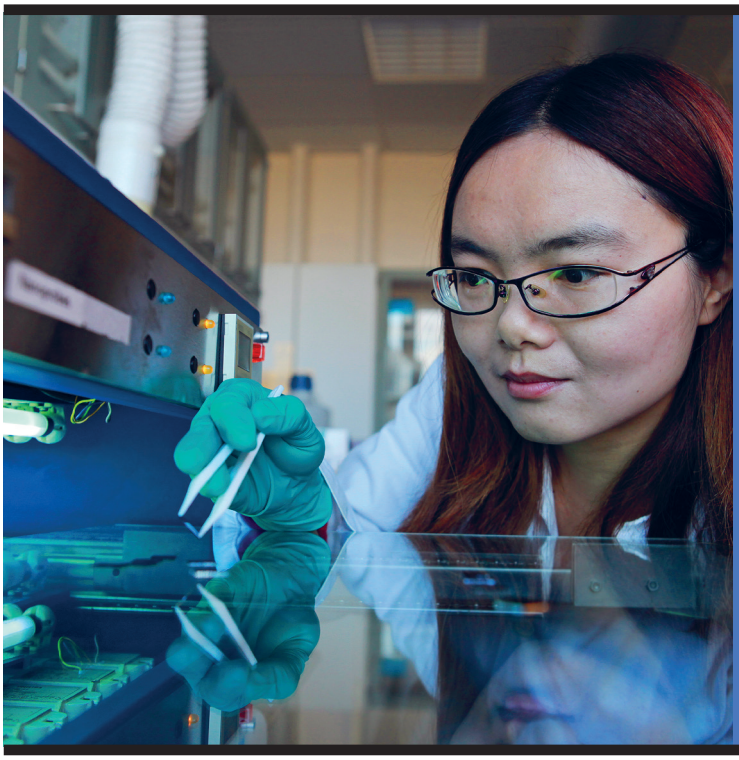

Nanopatterning of graphene guided by block copolymer self-assembly

Zhongli Wang
PhD Thesis November 2017

DTU Nanotech
Department of Micro- and Nanotechnology

Abstract

Motivated by the unique and superior properties of graphene, including transistors, integrated circuits, displays, sensors, nanocomposite materials and optical applications, we have pioneered advances in the emerging field of nanopatterned graphene. This PhD project is a part of Center for Nanostructured Graphene (CNG) activities. As compared to pristine graphene, nanopatterned graphene creates a band gap suitable for transistor logic applications, enables functionalization of graphene edges, creates novel magnetic and optical properties, and could be utilized in ultrathin, high-flow filtration applications.

The main purpose of this PhD project is to explore and develop block copolymer self-assembly for generating highly ordered nanostructure graphene with as small as possible neck width and period sizes, which can be utilized in many important applications such as sensors, transistors and optoelectronic devices. Here, we use a novel block copolymer (BCP) self-assembly method for nanolithography. This procedure significantly simplifies the traditional BCP lithography process, showing a wide substrate tolerance and allowing for efficient pattern transfer. Afterward we fabricated uniform suspended nanomesh graphene with the pore size of 24 nm and neck width of 14 nm by using this BC lithography process, combing local photocatalysis. We also achieve large-area fabrication of nanoscale graphene disk and nanomesh arrays, which support plasmon resonances in the near-infrared regime. In the end of this thesis, we functionalize graphene chemically in the presence of the nanoporous mask.

These bottom-up BC lithography methods allow the fabrication of arbitrary geometries, with rational control over the graphene nanostructure's placement, orientation, size, and lateral extent, which paves ways for numerous applications.

Dansk resumé

Grafen er en et-atom tyk 2D kulstof materiale med unikke egenskaber, som kan finde anvendelse i en række områder, herunder fremstilling af transistorer, integrerede kredsløb, skærme, sensorer, nanokomposit materialer og optiske komponenter. Mange af disse applikationer kræver nanostrukturering af grafen, hvilket har været hovedmotivationen for PhD projektet. Projektet indgår som en del af forskningsaktiviteterne indenfor Grundforskningsfondens Center for Nanostructured Graphene (CNG) på DTU. Nanostrukturering tilfører grafen nye egenskaber, f.eks. der åbnes et elektronisk båndgap i grafen, som er nødvendigt for at bygge transistorer; nye magnetiske og optiske egenskaber opstår som kan tunes ved kontrolleret kemisk funktionalisering af grafenkanterne og som er relevante ifm. mange applikationer i optik og sensorteknologi; de ultratynde og mekaniske stærke grafenmembraner kan også anvendes i en række højstrømningsfiltreringsapplikationer.

Hovedformålet med dette ph.d.-projekt er at undersøge anvendelsen af de selvorganiserede nanostrukturer dannet af blokcopolymerer (BCP) som skabeloner til fysisk og kemisk nanostrukturering af grafen. Under kontrolleret eksperimentelle betingelser er det muligt at fremstille velordnede BCP skabeloner over arealer på 1-500 cm^2 som består af periodiske strukturer med karakteristiske længde-skalaer på 5-50 nm. Denne type skabeloner fremstillet i form af 10-50 nm tynde film kan anvendes som masker til nanolitografi; BCP strukturmønstret kan derefter overføres til substratet under masken, som kan være silicium eller grafen. Vi har udviklet en procedure der væsentligt forenkler state-of-the-art BCP litografi processen, samtidig med at den viser bred substrat-tolerance og giver mulighed for effektiv mønsteroverførsel. Ved kontrolleret annealing under dampe af selektive opløsningsmidler organiserer blok-copolymeren sig spontant i ensartet heksagonal pakket cylinder eller sfære morfologier; maskdannelsen kan fuldføres direkte på substratet, uden forbehandling af substratets overflade. BCP masken bruges direkte til

nanostrukturering af grafen vha. lt ætsning, eller til at danne fotokatalytiske nanostrukturer som derefter bruges til fremstilling af ensartet suspenderet nanomesh-grafen, dvs. grafen punkteret efter et heksagonalmønster. I sidste tilfælde har vi demonstreret fremstilling af nanomesh grafen med porestørrelse på 24 nm og halsbredde på 14 nm. Vi har også demonstreret fremstilling vha. ilt ætsning af grafen nanodisk eller nanomesh arrays, som over store overflader understøtter plasmon resonanser i det nær-infrarøde regime. Plasmon aktiviteten er grundprincippet for mange optiske og opto-elektroniske enheder og sensorer, mens nær-infrarød området er attraktiv for at opnå integrering af disse enheder i kommercielle telekommunikations netværk. I slutningen af afhandlingen beskrives de resultater vi har opnået om kemiske funktionalisering af grafen ved at bruge forskellige nanoporøse BCP masker som skabelon.

De beskrevne bottom-up BCP litografi metoder tillader fremstilling af forskellige grafen mønstrer i nanoskala, med rationel kontrol over grafen nanostrukturets placering, orientering, størrelse og lateral udstrækning, hvilket forventes at øge muligheden for fremtidige teknologiske anvendelser af disse nanostrukturer.

Acknowledgement

The project presented here as a PhD thesis was carried out at the Center for Nanostructured Graphene (CNG) in Department of Micro- and Nanotechnology at the Technical University of Denmark (DTU) from 2014 to 2017. Block copolymer lithography and nanopatterned graphene fabrication were performed at the National Center for Micro- and Nanofabrication DTU Danchip. Nanopatterned graphene plasmonic was finished at the Department of Photonic Engineering in DTU. The overall project was financed by CNG and DTU.

I am very grateful for all the support I have been given during my time at the Technical University of Denmark. This thesis would not be possible without the help of many people, some of whom I will list here.

First I thank my supervisor Sokol Ndoni who gave me the endless patience, massive encouragement and help me during my entire PhD process. I am very grateful for his constant inspiration when I confront the difficult in my PhD project. I also thank Sokol who helped me to revise my manuscript.

I thank my co-supervisor – Professor Kristoffer Almdal for his continued support and many useful suggestions and guidance during my time at DTU. Thanks Lars Schulte for synthesized all the polymers I need in my PhD project. Thanks him for setting up the electrochemistry measurement and always providing the technique support as his best.

I thank associate professor Sanshui Xiao who is from the DTU Photonic. He guided and provided me with photonic measurement supports for my second published paper. I can't achieve this project without his help. I thank my colleague Tao who also help me a lot to optimize the mask fabrication and gave very useful suggestions for my each project activity. I thank him a lot and hope he can have a good research career in the future.

I thank Lene Gammelgaard, David Mackenzie, Bilong Luo, Bjarke Sørensen Jessen and Johanna Zultak who are from Professor Peter Bøggild's group. They provided me the support of Raman measurements, electrical measurements, CVD graphene and exploited hBN samples. I learned a lot from them.

I thank my other group members Sozaraj Rasappa, Lotte Nielson who support me in many ways. I also thank Sergey Chernyy who provided some interesting di block/Tri block polymers to me and we made a promising work together.

Lastly I thank my family and friends for their support during all these years.

Zhongli Wang

July 2017

List of Abbreviation

AFM	Atomic force microscopy
ALD	Atomic layer deposition
ASE	Advanced Silicon Etcher
BPO	Benzoyl peroxide
BCP	Block copolymer
CVD	Chemical vapor deposition
C	Cylinders
CPS	Closely packed spheres
DSA	Directed self-assembly
EA	Ethyl acetate
FWHM (2D)	Full width half maximum of the 2D peak
FET	Field-effect transistor
GNM	Graphene nanomesh
GPPs	Graphene-plasmon polaritons
GNDAs	Graphene-nanodisk arrays
G	Gyroids
GALs	Graphene anti-dots lattices
HEX	Hexagonally packed structure
ICP	Inductively coupled plasma
L	Lamellae
Mn	Molecular weight
NMR	Nuclear magnetic resonance
ODT	Order to disorder transition
OOT	Order-to-order transition
P2VP	polystyrene-block-poly(2-vinylpyridine)
P4VP	polystyrene-block-poly(4-vinylpyridine)
PDI	Poly dispersive index
PDMS	Polydimethylsiloxane
PEO	Polyethylene oxide
PLA	Polylactide
PMMA	Poly(methyl methacrylate)
PS	Polystyrene
PS-b-PDMS	Poly (styrene)-block-polydimethylsiloxane
PSF	Polysulfone
QCM	Quartz crystal microbalance
RIE	Reactive ion etching
S	Spheres
SD	Polystyrene-*b*-polydimethylsiloxanes
SVA	Solvent vapor annealing
SEM	Scanning electron microscopy
SSL	Strong segregation limit
SCMF	Self-consistent mean-field
Tg	Glass transition temperature
THF	Tetrahydrofuran

W	Neck width
WSL	Weak segregation limit

Contents

1. Introduction

1.1 Thesis structure

Graphene is a rapidly rising star on the horizon of materials science and condensed-matter physics. The huge carrier mobility, high optical transparency and high thermal conductivity make it a unique material to explore the 2D-physics for the fabrication of devices with wide range of electronic and optoelectronics applications. Despite its high potentials, several challenges still remain. These include intrinsic zero energy band gap, low reactivity and limited availability of well-defined pristine graphene, which have hampered the rapid development of graphene-based functional devices. Various physical and chemical methods have been developed for the nanopatterned graphene using top down and bottom-up processes. Many research groups have already showed the disadvantages in top-down lithography such us edge defects, complicated procedure, time-consuming and low output.

This thesis aims manufacturing nanopatterned graphene with controlled defects in large area-using bottom-up process, specifically block copolymer lithography. We explored and presented two main approaches, namely templated block copolymer nanolithography and nanoporous organic polymer template for chemical functional graphene. Both of these approaches are proved to be effective.

In chapter 1, the state-of-arts of block copolymer self-assembly is reviewed firstly. Then a background on graphene is given in details, following by the significance of nanopatterned graphene.

Chapter 2 summarizes several methods of block copolymers self-assembly on silicon substrate developed in this thesis. A novel block copolymer (BCP) nanolithography process with hexagonally packed cylindrical morphology by selective solvent vapor annealing has been demonstrated. Second we have shown that a simple reconstruction of the organic BCPs (PS-b-PVP BCPs) can provide etching contrast and allows the patterning of BCP masks for subsequent pattern transfer into the

underlying substrate. Finally we discuss a new block copolymer PF9MA-PFMMA ($PF9_{35k}F_{25}$), also of hexagonally packed cylinder morphology by using this efficient annealing method.

Chapter 3 introduces a novel method to fabricate uniform graphene nanomesh and nanoribbons using local photocatalysis of graphene sheet by the contact of vertically aligned TiO_2-covered nanopillars and nanowire arrays. And AFM and SEM images illustrated formation of the graphene nanomesh with the pore size of 24 nm and neck width of 14 nm. Graphene nanoribbons with a periodicity of 36 nm have also been fabricated in such a way.

In chapter 4 we demonstrate using well-ordered vertically oriented cylinder and monolayer packed sphere morphologies to pattern graphene, and so that We have used well-ordered vertically oriented cylinder and monolayer packed sphere morphologies to pattern graphene, and the dipole resonance of the GNDs plasmon polaritons has been pushed down to 2.0 μm and the GNMs plasmon polaritons has been pushed down to 1.7 μm, which is to the best of our knowledge the smallest value reported for the localized GPP resonance. With some further refinements, our results would facilitate graphene plasmons both for fundamental study and for potential applications in the telecommunication window.

Chapter 5 a chemical reaction on graphene was achieved in the presence of a nanoporous mask of hexagonal morphology; we have shown that graphene reacts with benzoyl peroxide under intense laser irradiation, producing significant defects in the basal plane. For the first time, we adapted chemical functionalization to the nanoporous mask at nano-scale size on top of graphene. Each pore in this case functioned as a nanoreactor for the heterogeneous chemical modification of the graphene at the bottom of the pore. We propose that a hot electron initiates an electron transfer from photoexcited graphene to the physisorbed benzoyl peroxide. This electron transfer produced a transient benzoyl peroxide radical anion, which irreversibly decomposes to produce the phenyl radical, which introduces sp^3 defect centers onto the basal plane of graphene.

Chapter 6 concludes this PhD thesis and gives future suggestions based on this project.

The overall thesis is based on my publications and the manuscripts in the appendices.

1.2 Block copolymers self-assembly

1.2.1 Basic information of block copolymers

Block copolymers are well-known soft-materials for their ability to self-assemble into well-ordered nanometer scale microdomians (*1, 2*). They are macromolecules with the different monomer segments organized into continuous blocks. Typical block copolymers are linear and contain two or three unique monomer chemistries organized into two or three blocks: AB, ABA, and ABC.

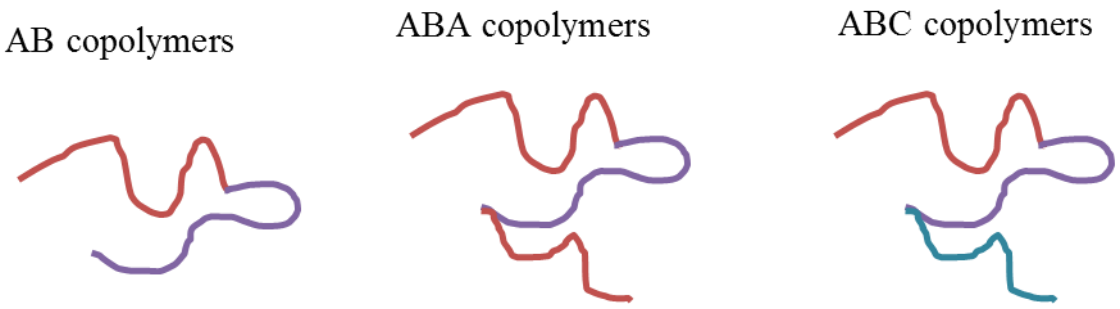

Figure 1.1 Structural illustrations of typical block copolymers.

Self-assembly of BCPs is a very broad and active research area. BCP self-assembly in bulk has been studied extensively since the 1960s and is well understood. Many books and reviews have already reported the theories (*1, 3, 4, 5, 6*). Microphase segregation of block polymers is a thermodynamically driven process that leads to periodic nanoscale structures. The phase diagram of the equilibrium morphology of BCP self-assembly has already been studied very well, as shown in Figure 1.2, where χ is the Flory-Huggins segmental interaction parameter, N is the total number of repeating units, i.e. the degree of polymerization, and *f* is the volume fraction of one block. In terms of χN, the so-called weak segregation limit (WSL) (χN<10) and the strong segregation limit (SSL)

(χN>>10) were introduced. To span the range, the self-consistent mean-field (SCMF) theory has been developed (*7-12*). With increasing *f* at a fixed χN above 10.5, the order-to-order transition (OOT) starts from closely packed spheres (CPS, which separates the disordered state and S phase), passing through body-centered cubic spheres (S), hexagonally packed cylinders (C) and bicontinuous gyroids (G), to lamellae (L). Morphological inversion takes place when the composition is inverted.

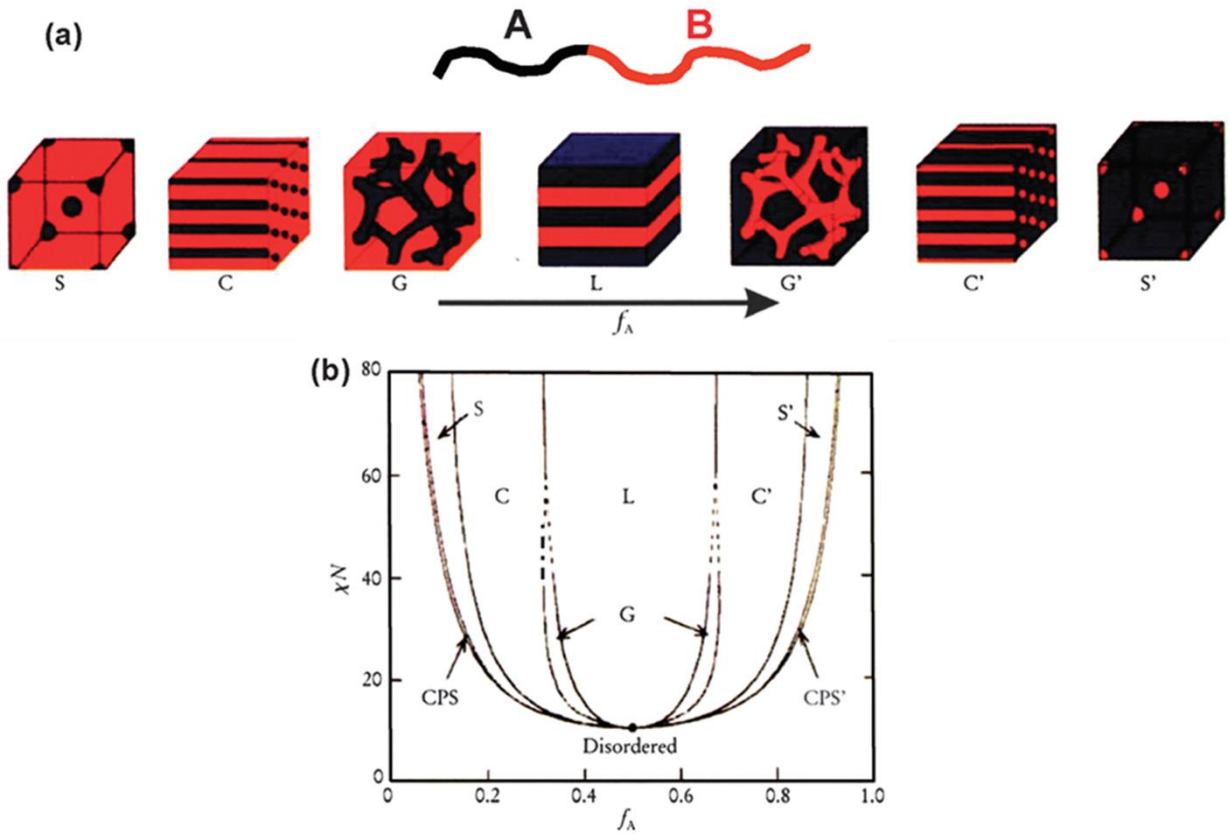

Figure 1.2 (a) Equilibrium morphologies of AB diblock copolymers in bulk: S and S' = body-centered-cubic spheres, C and C' = hexagonally packed cylinders, G and G' = bicontinuous gyroids, and L = lamellae. (b) Theoretical phase diagram of AB diblocks predicted by the self-consistent mean-field theory, depending on volume fraction (*f*) of the blocks and the segregation parameter, χN, where χ is the Flory–Huggins segment–segment interaction energy and N is the degree of polymerization; CPS and CPS' = closely packed spheres (*1*).

1.2.2 Thermal annealing and solvent vapor annealing

The most practical applications of self-assembled block polymers generally rely on thin film formation since this is the most appropriate form to create a surface pattern that can be transferred to a substrate for the creation of functional nanoscale devices. However many more parameters are critical in a thin film formation and the phase diagram become complex. The important parameters such as film thickness and interaction with each of the two interfaces for both blocks are considered. According to the self-consistent field theory, around 20 morphologies are considered to construct to the two-dimensional phase diagram with correlate to the volume fraction and the film thickness, while the interaction parameter χN and the surface preferences are fixed (Figure 1.3) *(13)*. The morphology of BCP is mainly depended on the parameters such as molecular mass and composition of BCP, film thickness, interaction between blocks and energies of interaction of each block with top and bottom interfaces.

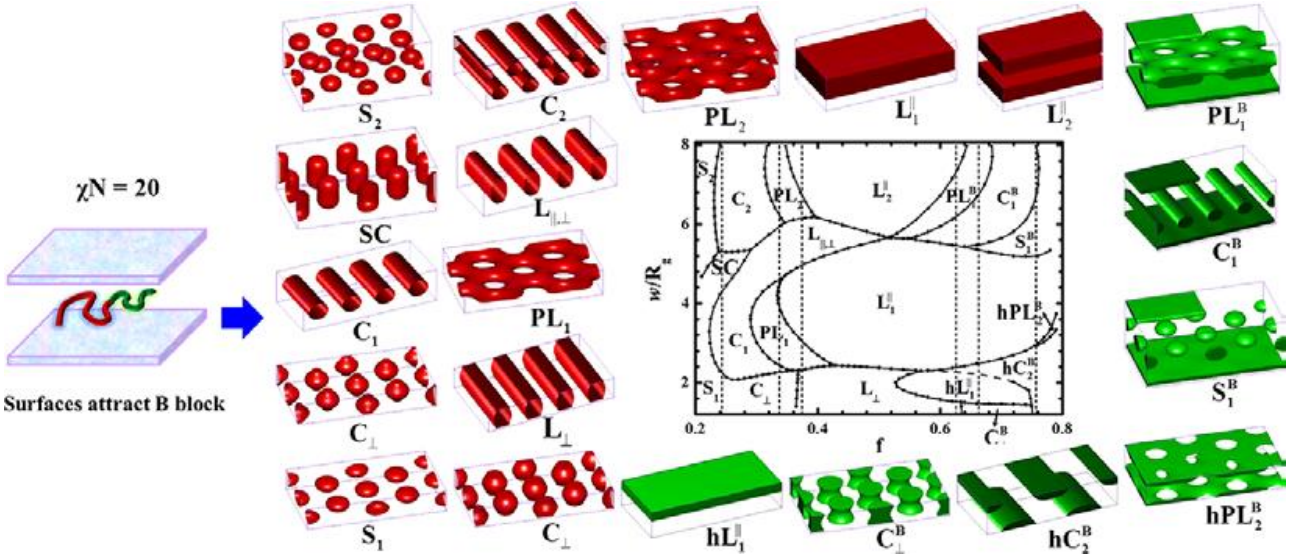

Figure 1.3 Phase diagram of AB diblock copolymers of fixed χN = 20 in a thin film with respect to the volume fraction of the A block and the film thickness, w, in units of radius of gyration (Rg) *(13)*.

When block polymer thin films are cast from a solvent onto a substrate, they generally become kinetically trapped in nonequilibrium and disorganized structures. To adopt the highly regular structures predicted at equilibrium, the mobility of the polymer chains must be sufficient to allow for structural reorganization. The annealing process used to promote microphase separation is key component of any application of BCPs in nanoscale pattern generation. In some systems, simple thermal treatments above the limiting glass transition temperature (Tg) of the system can be successfully used to facilitate the attainment of the equilibrium structure. In a typical thermal annealing process, BCP thin films are simply heated above its glass transition temperature of the respective blocks of the copolymer and hold at elevated temperature for a certain time, then cooled down to room temperature. For example, PS-b-PMMA BCPs are typically annealed at temperatures between 160 and 250 degrees depending on its molecular weight. However, for many high molar mass BCPs thermal treatments alone are not very effective and very long anneal times are often required (*14*). To combat such long annealing periods, another annealing process known as solvent vapor annealing (SVA) has been shown to be generally much more effective. Solvent vapor annealing (SVA) is the other very useful technique to anneal the BCPs thin films, when ODT of BCPs is difficult or even impossible to observe experimentally due to thermal stability limits, which are very common for BCPs with high χ or large molecular weight. One of the very first examples reporting an improvement in long-range order in block polymer films using solvents was by Albalak et al. in 1998 (*15*). In this work, solvent swollen roll-cast films of poly (styrene)-b-poly (butadiene)-b-poly (styrene) triblock polymers with cylinder and lamellar morphologies were studied upon preferential (toluene) and nonpreferential (methyl ethyl ketone (MEK) and hexane) solvent exposure using small-angle X-ray scattering. The microphase-separated pattern formed was found to be similar in structure and degree of order as seen by a thermal annealing approach but was achieved in significantly reduced times. They suggested that the SVA methodology favored

mobility of the polymers in the swollen state, allowing the system to reach the thermodynamically preferred, nanostructured arrangement. Despite the fact that SVA as a structure forming technique was not specifically highlighted in this landmark work, the complexity of the transition from a film of a block polymer solution toward a solid film was established. The block polymer films produced at more rapid solvent evaporation rates were "kinetically constrained" in a disordered arrangement since the evaporation rate of the solvent was fast compared to the diffusion of the macromolecules. In contrast, slow evaporation rate leads to an ordered organization with vertical (i.e., perpendicular to the surface plane) cylinders, and even slower evaporation rate gave in-plane (i.e., parallel) cylinders. Works published by Fukunaga et al. in 2000 (*16*) and Knoll et al. in 2002 (*17*) were also informative and important early examples demonstrating how solvent vapor exposure can enable morphological rearrangements from ascast disorganized states. Russell group reported a study by follow where cylindrical forming polystyrene-blockpolyethylene oxide (PS-b-PEO) BCP self-assembled into highly ordered hexagonally packed PEO microdomains in a PS matrix after solvent vapor annealed in THF vapor (*18*).

When preparing a block polymer thin film that will be used to SVA, there are several important factors that influence the final state of the film. All of the factors can impact the efficacy of the annealing process. The relative sensitivities, however, can vary dramatically; some aspects impact the overall process in a broad window, and other aspects are highly sensitive to even minor perturbations. It is therefore important to consider each of the factors when developing a new process or using new block polymer structures to reveal these sensitivities. A schematic depicting the overall process is shown in Figure 1.4 by Hillmyer group (*19*).

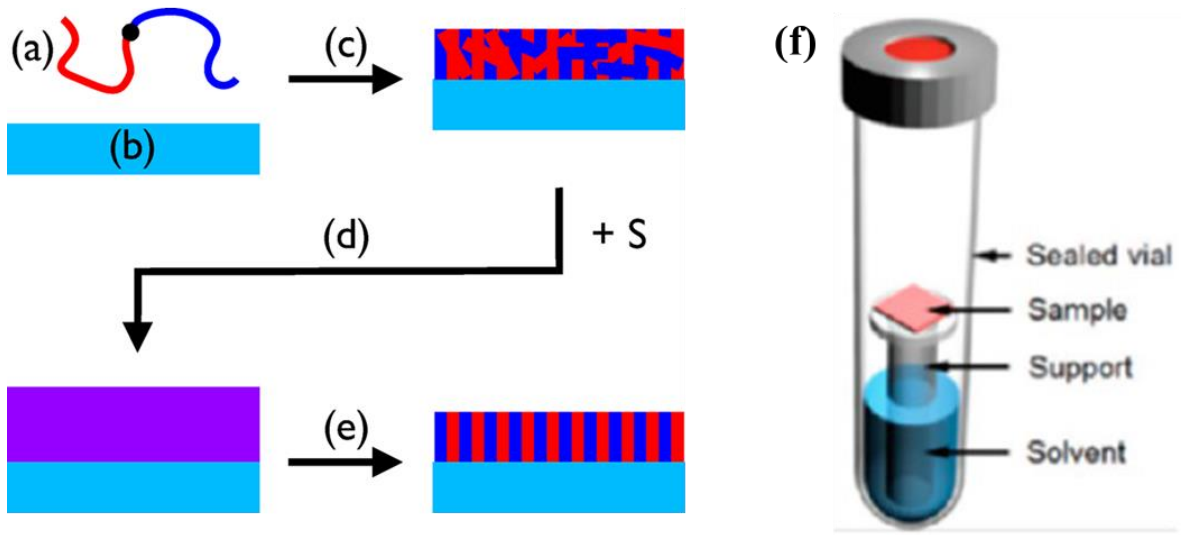

Figure 1.4 A schematic showing the main process for SVA of block polymer thin films: (a) block polymer selection, (b) substrate preparation, (c) film formation (S) solvent exposure, (d) a homogeneous, swollen film shown, (e) deswelling by solvent evaporation to a perpendicular cylindrical structure as an example and (f) set-up of the solvent vapor-annealing chamber.

However a comprehensive understanding of the solvent vapor annealing process has not established despite of the wide use of solvent vapor annealing. One of the reasons for lack of understanding the SVA process is that, morphology of the BCP films are typically characterized after solvents being removed from swollen film. Detailed studies on the effects of each of these parameters on the morphology of BCP thin films are scarce, yet they are essential for a controlled annealing and to obtain the desired morphology. There are many other factors affecting the morphology of a BCP film in the swollen state and after removal of solvent vapor, for example, selectivity of the solvent, amount of swelling given to BCP film, solvent removal rates, film thickness, humidity, and temperature. Thus in the following part of this thesis, detailed studies about the different factors will be discussed in experiments.

1.2.3 Block copolymer lithography

Due to the high-resolution and high-throughput at lower cost, large area BCP lithography has great potential to semiconductor manufacturers. To take full advantage of the nanostructures offered by the self-assembly of BCPs, highly selective pattern transfer techniques with high fidelity are required. Typically, a two-steps etching process is needed to transfer the self-assembled BCP pattern to other functional materials. In the first step, one block of the BCP is selectively removed to make an etch mask; and then the etch mask is further pattern transferred to other functional materials in the second step.

Selective removal of block A from diblock copolymer A-B template is not a simple task. For the BCPs contains inorganic elements which have large etching contrast and high Flory-Huggins parameter, simple oxygen RIE treatment can remove one block and convert the left block into the inorganic oxides. For example, PS-b-PDMS and PS-b-PFS were reported to form their respective inorganic oxides replicates the inorganic containing block, which can act as etch mask for the following etching step (*20-22*).

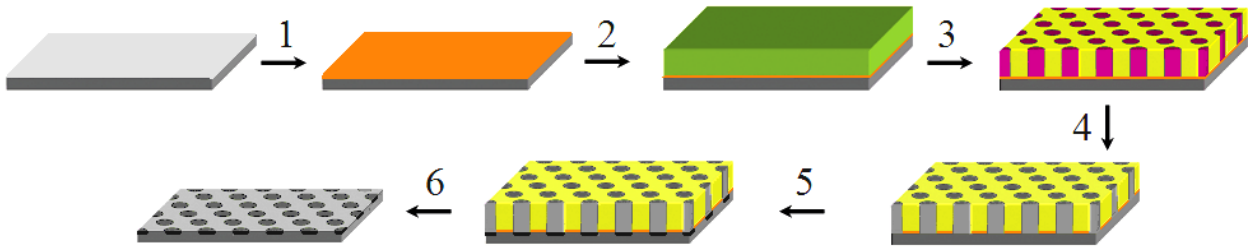

Figure 1.5 Illustration of the typical process of conventional BCP lithography: (1) random brush grafting; (2) spin-coating of the BCP film; (3) thermo/Solv annealing; (4) etching of the mask; (5) etching of the underlying substrate; (6) mask removal (*23*).

However most BCPs are made of organic materials, where it lacks etching contrast between different blocks. Simple oxygen RIE removes both organic polymer blocks at a similar rate, leaving a flat film that unsuitable for further pattern transfer. Thus, different methods, depending on the chemical structure of BCP, have been to selectively remove minor block but not the other. For PS-

b-PMMA BCP, a UV light selectively degrades the PMMA block and crosslinks the PS block at the same time (*24*). For polystyrene-block-poly(lactide) (PS-b-PLA) BCP, a weak acid or base is used to selective degrade PLA block using a hydrolysis reaction, thus selectively removes PLA block leaving PS domain as etch mask(*18, 25*). But as for other organic BCP systems, PS-b-PEO and PS-b-P2VP/PS-b-P4VP BCPs, a reconstruction process is needed to enhance the etch contrast between two organic blocks (*18, 26, 27*).

1.3 Background on Graphene

Graphene is a two-dimensional material consisting of either a flat monolayer or few layers of carbon atoms arranged in a honeycomb lattice structure (Figure 1.6) (*28, 29*). Because of its unique electrical, optical, thermal, and mechanical properties, graphene has attracted much interest for its potential in various applications (*30-34*).

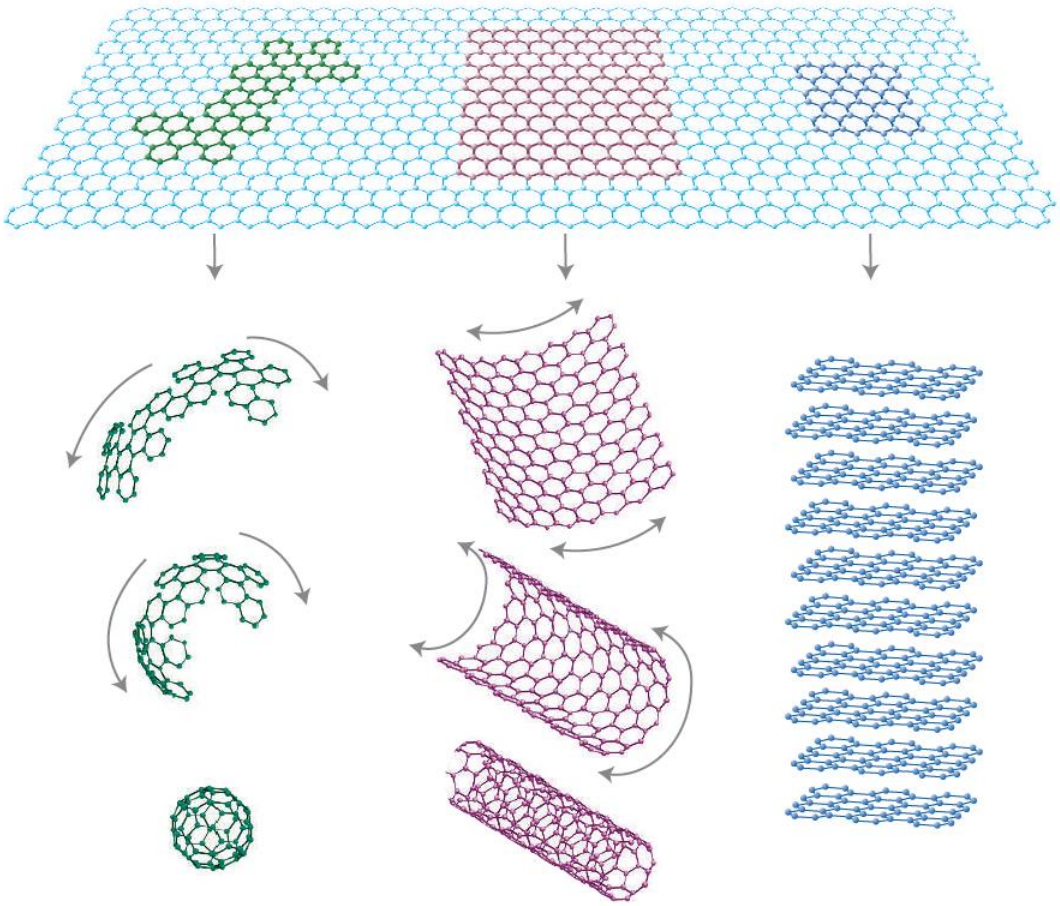

Figure 1.6 Mother of all graphitic forms. Graphene is a 2D building material for carbon materials of all other dimensionalities. It can be wrapped up into 0D buckyballs, rolled into 1D nanotube or stacked into 3D graphite (*28*).

The covalent bonds between nearest-neighbor carbon atoms in graphene are formed by sp^2-hybridised orbitals. These strong bonds give graphene its extraordinary mechanical strength, making it possible to have stable free-standing graphene sheets, being only one atomic layer thick (*35*). The remaining p-electron per atom is delocalized over the whole graphene lattice, and is responsible for the electric conductivity. Figure 1.7a represents the lattice structure of graphene. The graphene lattice consists of two interpenetrating sublattices, denoted A and B depicted in blue (dark gray) and red (light gray). The unit cell, indicated in gray, therefore comprises two atoms, one of each sublattice. The nearest neighbor distance is a_0 = 1.42 A. In reciprocal space, the first Brillouin zone also has a hexagonal shape (Figure 1.7b). A tight-binding approach (*36*) leads to the band structure shown in Figure 1.7b. Valence and conduction bands touch at the K and K' points at the corners of the first Brillouin zone, with a linear dispersion for small enough energies (Figure 1.7c). Around the K and K' points the dispersion relation of graphene can be described by the expression $E_{\pm}(q) \approx \pm \hbar v_F |q|$, with $v_F \approx 1 \times 10^6$ m s^{-1}. In undoped graphene, the Fermi energy lies exactly at the Dirac point: the π-band is completely filled, while the π^*-band is empty (*37*).

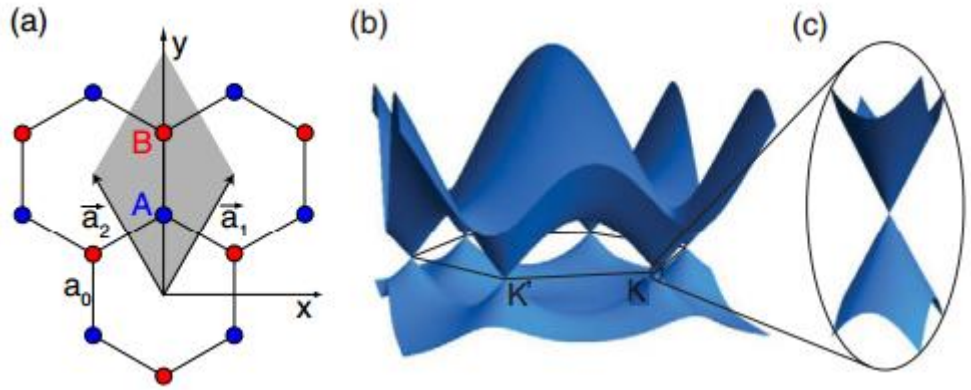

Figure 1.7 (a) Lattice structure of graphene. The atoms belonging to the two sublattices A and B are represented by circles; the lines between the circles indicate the chemical bonds. a_0 is the nearest-neighbor distance. The unit cell is depicted in gray, together with the primitive lattice vectors $a_{1,2}$. (b) Band structure of graphene. (c) Zoom of the dispersion relation close to the K-point for small energies (*37*).

So far, the most popular approaches to graphene preparation are mechanical exfoliation (*28*), growth on metals and subsequent graphene transfer to insulating substrates (*38, 39*), and thermal decomposition of SiC to produce so-called epitaxial graphene on top of SiC wafers (*40, 41*). Exfoliation is still popular for laboratory use but it is not suited to the electronics industry, whereas the other two options both have the potential for producing wafer-scale graphene. After the graphene has been prepared, common semiconductor processing techniques (such as lithography, metallization and etching) can be applied to fabricate graphene transistors. The most frequently stated advantage of graphene is its high carrier mobility at room temperature. Mobilities of 10,000–15,000 $cm^2 \cdot V^{-1} \cdot s^{-1}$ are routinely measured for exfoliated graphene on SiO_2-covered silicon wafers (*42*), and upper limits of between 40,000 and 70,000 $cm^2 \cdot V^{-1} \cdot s^{-1}$ have been suggested (*43*). Moreover, in the absence of charged impurities and ripples, mobilities of 200,000 $cm^2 \cdot V^{-1} \cdot s^{-1}$ have been predicted (*44*), and a mobility of 10^6 $cm^2 \cdot V^{-1} \cdot s^{-1}$ was recently reported for suspended graphene (*45*). For large-area graphene grown on nickel and transferred to a substrate, mobilities greater than 3,700 $cm^2 \cdot V^{-1} \cdot s^{-1}$ have been measured (*38*). Finally, for epitaxial graphene on silicon carbide, the mobility depends on whether the graphene is grown on the silicon face or the carbon face of SiC. Although graphene grown on the carbon face has higher mobility (values of ~5,000 $cm^2 \cdot V^{-1} \cdot s^{-1}$ have been reported (*41*), compared with ~1,000 $cm^2 \cdot V^{-1} \cdot s^{-1}$ for graphene grown on the silicon face (*46*), it is easier to grow single-layer and bilayer graphene on the silicon face, which

makes the silicon face of SiC more suited for graphene MOS device was among the breakthrough results reported by the Manchester group in 2004 (ref. 1).

A 300-nm SiO_2 layer underneath the graphene served as a back-gate dielectric and a doped silicon substrate acted as the back-gate (Figure 1.8a). Such back gate devices have been very useful for proof-of-concept purposes, but they suffer from unacceptably large parasitic capacitances and cannot be integrated with other components. Therefore, practical graphene transistors need a top-gate. The first graphene field-effect transistor (FET) with a top-gate was reported in 2007(*47*), representing an important milestone, and progress has been very rapid since then (Figure 1.8b) (*47*).

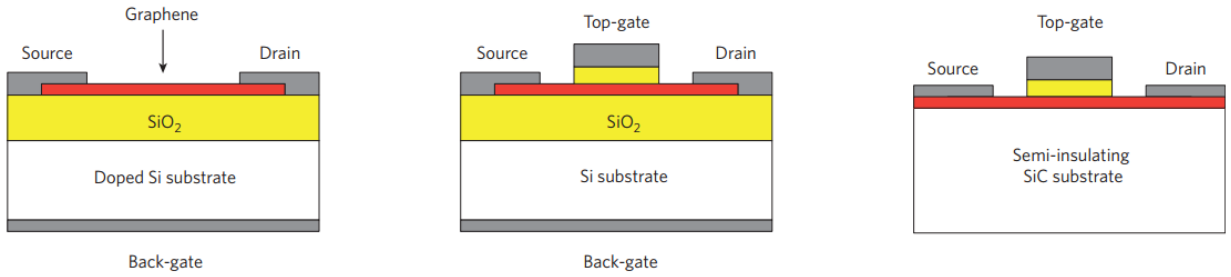

Figure 1.8 Schematics of different graphene FET types: back-gated FET (left); top-gated FET with a channel of exfoliated graphene or of graphene grown on metal and transferred to a SiO_2-covered Si wafer (middle); top-gated FET with an epitaxial-graphene channel (right) (*45*).

Although the low on–off ratios demonstrated so far make use in logic devices unrealistic, transistors with large-area graphene channels are promising candidates for radiofrequency applications because radiofrequency FETs are not required to switch off and can benefit from the high mobilities offered by large-area graphene. However, the absence of drain-current saturation will limit the radiofrequency performance of graphene transistors. One method of introducing a bandgap into graphene for logic applications is to create graphene nanoribbons. Nanoribbon FETs with back-gate control and widths down to less than 5 nm have been operated as p-channel devices and had on–off

ratios of up to 106 (*48*). This, and other evidence of a sizeable bandgap opening in narrow nanoribbons, provides proof of the suitability of nanoribbon FETs for logic applications.

1.4 Nanopatterned Graphene

Nanopatterned graphene means using a specific method to remove the unwanted regions of a full graphene sheet. The most common method is using a reactive ion species to make disordered and random nanostructure on graphene plane. The bluntness of this reactive etching process also creates rough graphene edges in the patterned regions which can severely degrade the electrical and mechanical properties of graphene (*49, 50*).

Thus fabrication of high performance nanostructured graphene demands efficient nanopatterning technologies able to produce nanoscale periodic or quasiperiodic modulations over large areas. It has been shown that quantum confinement effects can be used to open up a band gap in graphene. For example, it has been demonstrated that the band gap of graphene nanoribbons, Eg, patterned using electron-beam lithography, roughly varies inversely with the width of the nanoribbons, ω, according to Eg ~ 0.2-1.5 eV·nm/ω (*36, 51, 52*). Other forms of nanostructured graphene showing semiconducting behavior have also been fabricated using electron-beam lithography, including graphene quantum dots (*53*) and inverse dot lattices (*54, 55*). The successes of electron-beam lithography in fabricating graphene nanostructures that exhibit semiconducting behavior motivates future studies of nanostructured graphene based materials and devices. However two challenges have become apparent from these preliminary studies. First, in order to open a band gap>>kT in nanostructured graphene, it must be nanopatterned to critical dimensions <20 nm. However, 20 nm is on the threshold of achieving good pattern using conventional electon beam lithography due to known electron scattering effects in common electron beam resists. The second challenge is that electron-beam lithography is a serial technique, which limits its throughput and applicability to the large-area patterning of graphene. Thus, in order to practically realize nanostructured graphene-

based materials, new patterning techniques that can be extended to large areas with sub-20- nm resolution are needed.

Sinitskii and Tour (*56*) used nanosphere lithography to prepare a porous metal film, which was then employed as an etch mask for fabrication of graphene nanomesh (GNM), however it had unsatisfactory geometrical dimensions. As an alternative, self-assembly nanoarrays have been extensively investigated, such as a block co-polymer (BCP) and anodized aluminum oxide. One of the most fascinating properties of self-ordered nanoarrays lies in the readiness of its fabrication on length scales that are difficult to obtain by standard semiconductor lithography technique (*57*). Block copolymer (BCP) self-assembly has been extensively studied as a promising lithographic technique for patterning sub-10 nm scale features densely aligned over large areas (*59, 60*). Several BCP related methods have been developed to pattern graphene sheets into hexagonally packed graphene nanomeshes (GNMs) with sub-10 nm interhole spacing (*58, 61, 62*). The advantages of BCP self-assembly include structure formation at the sub- 10-nm scale, scalable parallel processing, and ultrafine pattern precision. Furthermore, BCP self-assembly can be used to create laterally ordered, device-oriented nanopatterns by directed self-assembly (DSA) (*63*). For example, Liang et al. combined the self-assembly of BCPs and nano-imprint lithography to prepare GNM with neck width (w) down to less than 10 nm (Figure 1,10).

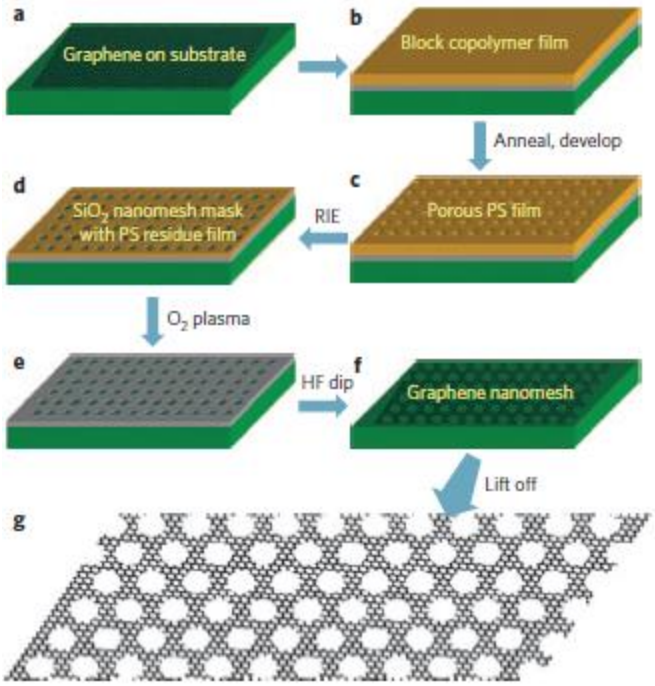

Figure 1.9 Schematic of fabrication of a graphene nanomesh by poly (styreneblock-methyl methacrylate) (P(S-b-MMA)) block copolymer (*61*).

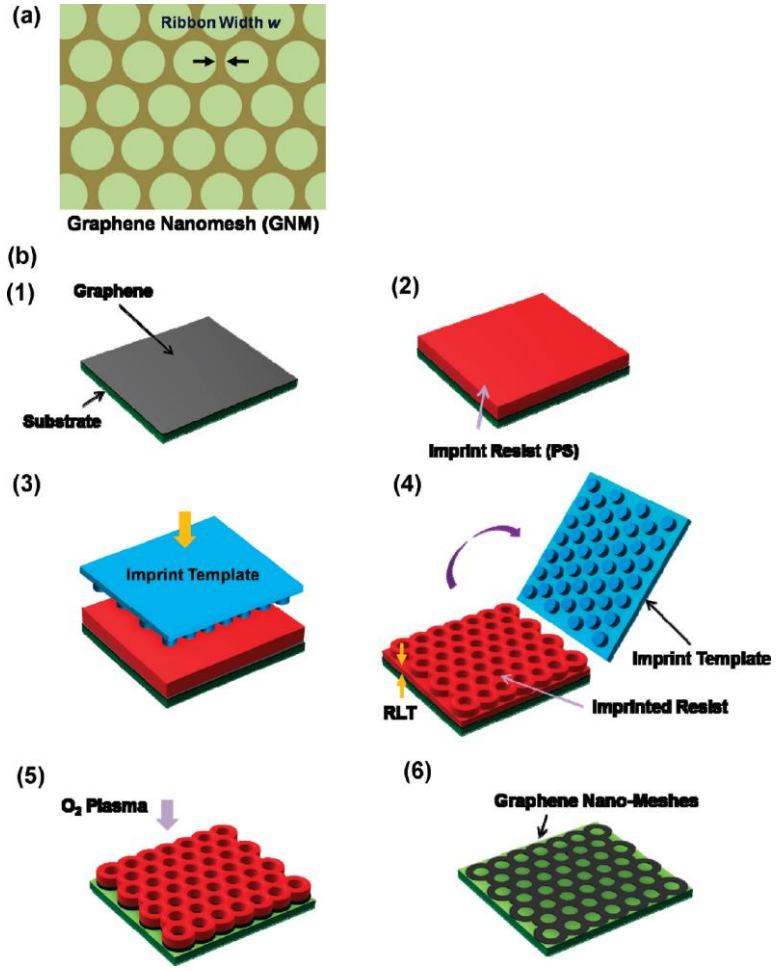

Figure 1.10 (a) Schematic illustration of graphene nanomesh (GNM) with ribbon width w. (b) Schematic fabrication process of graphene nanomeshes (GNMs) (*58*).

1.5 References

1. F. S. Bates, G. H. Fredrickson, Block copolymers—designer soft materials. *Physics today* 52, 32 (1999).
2. I. Hamley, Ordering in thin films of block copolymers: Fundamentals to potential applications. *Progress in Polymer Science* 34, 1161 (2009).
3. P. Alexandridis, B. Lindman, *Amphiphilic block copolymers: self-assembly and applications*. (Elsevier, 2000).
4. S. Förster, T. Plantenberg, From Self‐Organizing Polymers to Nanohybrid and Biomaterials. *Angewandte Chemie International Edition* 41, 688 (2002).
5. J. K. Kim, S. Y. Yang, Y. Lee, Y. Kim, Functional nanomaterials based on block copolymer self-assembly. *Progress in Polymer Science* 35, 1325 (2010).
6. M. C. Orilall, U. Wiesner, Block copolymer based composition and morphology control in nanostructured hybrid materials for energy conversion and storage: solar cells, batteries, and fuel cells. *Chemical Society Reviews* 40, 520 (2011).

7. E. Helfand, Z. Wasserman, Block copolymer theory. 4. Narrow interphase approximation. *Macromolecules* 9, 879 (1976).
8. E. Helfand, Z. Wasserman, Block copolymer theory. 5. Spherical domains. *Macromolecules* 11, 960 (1978).
9. E. Helfand, Z. Wasserman, Block copolymer theory. 6. Cylindrical domains. *Macromolecules* 13, 994 (1980).
10. L. Leibler, Theory of microphase separation in block copolymers. *Macromolecules* 13, 1602 (1980).
11. M. W. Matsen, M. Schick, Stable and unstable phases of a diblock copolymer melt. *Physical review letters* 72, 2660 (1994).
12. M. Matsen, F. S. Bates, Unifying weak-and strong-segregation block copolymer theories. *Macromolecules* 29, 1091 (1996).
13. Li, W.; Liu, M.; Qiu, F.; Shi, An-C. Phase Diagram of Diblock Copolymers Confined in Thin Films. J. Phys. Chem. B, 2013, 117 (17), 5280-5288.
14. E. Han *et al.*, Perpendicular orientation of domains in cylinder-forming block copolymer thick films by controlled interfacial interactions. *Macromolecules* 42, 4896 (2009).
15. R. J. Albalak, M. S. Capel, E. L. Thomas, Solvent swelling of roll-cast triblock copolymer films. *Polymer* 39, 1647 (1998).
16. K. Fukunaga, H. Elbs, R. Magerle, G. Krausch, Large-scale alignment of ABC block copolymer microdomains via solvent vapor treatment. *Macromolecules* 33, 947 (2000).
17. A. Knoll *et al.*, Phase behavior in thin films of cylinder-forming block copolymers. *Physical review letters* 89, 035501 (2002).
18. S. H. Kim, M. J. Misner, T. Xu, M. Kimura, T. P. Russell, Highly oriented and ordered arrays from block copolymers via solvent evaporation. *Advanced Materials* 16, 226 (2004).
19. C. Sinturel, M. Vayer, M. Morris, M. A. Hillmyer, Solvent vapor annealing of block polymer thin films. *Macromolecules* 46, 5399 (2013).
20. Y. S. Jung, C. A. Ross, Orientation-controlled self-assembled nanolithography using a polystyrene− polydimethylsiloxane block copolymer. *Nano Lett* 7, 2046 (2007).
21. R. G. Lammertink *et al.*, Nanostructured Thin Films of Organic－Organometallic Block Copolymers: One‐Step Lithography with Poly (ferrocenylsilanes) by Reactive Ion Etching. *Advanced Materials* 12, 98 (2000).
22. J. Y. Cheng *et al.*, Formation of a cobalt magnetic dot array via block copolymer lithography. *Advanced Materials* 13, 1174 (2001).
23. R. Ruiz *et al.*, Density multiplication and improved lithography by directed block copolymer assembly. *Science* 321, 936 (2008).
24. T. Thurn-Albrecht *et al.*, Nanoscopic templates from oriented block copolymer films. *Advanced Materials* 12, 787 (2000).
25. A. S. Zalusky, R. Olayo-Valles, J. H. Wolf, M. A. Hillmyer, Ordered nanoporous polymers from polystyrene− polylactide block copolymers. *Journal of the American Chemical Society* 124, 12761 (2002).
26. S. Park, J.-Y. Wang, B. Kim, J. Xu, T. P. Russell, A simple route to highly oriented and ordered nanoporous block copolymer templates. *ACS nano* 2, 766 (2008).
27. S. Park *et al.*, Lateral ordering of cylindrical microdomains under solvent vapor. *Macromolecules* 42, 1278 (2009).
28. K. S. Novoselov *et al.*, Electric field effect in atomically thin carbon films. *Science* 306, 666 (2004).
29. A. K. Geim, K. S. Novoselov, The rise of graphene. *Nature materials* 6, 183 (2007).

30. K. Novoselov *et al.*, Nature 438 197 Zhang Y, Tan YW, Stormer HL and Kim P 2005. *Nature* 438, 201 (2005).
31. I. Meric *et al.*, Current saturation in zero-bandgap, top-gated graphene field-effect transistors. *Nature nanotechnology* 3, 654 (2008).
32. C. Lee, X. Wei, J. W. Kysar, J. Hone, Measurement of the elastic properties and intrinsic strength of monolayer graphene. *Science* 321, 385 (2008).
33. A. A. Balandin *et al.*, Superior thermal conductivity of single-layer graphene. *Nano Lett* 8, 902 (2008).
34. G. Tsoukleri *et al.*, Subjecting a graphene monolayer to tension and compression. *Small* 5, 2397 (2009).
35. J. C. Meyer *et al.*, The structure of suspended graphene sheets. *Nature* 446, 60 (2007).
36. A. C. Neto, F. Guinea, N. M. Peres, K. S. Novoselov, A. K. Geim, The electronic properties of graphene. *Reviews of modern physics* 81, 109 (2009).
37. F. Molitor *et al.*, Electronic properties of graphene nanostructures. *Journal of Physics: Condensed Matter* 23, 243201 (2011).
38. K. S. Kim *et al.*, Large-scale pattern growth of graphene films for stretchable transparent electrodes. *Nature* 457, 706 (2009).
39. A. Reina *et al.*, Large area, few-layer graphene films on arbitrary substrates by chemical vapor deposition. *Nano Lett* 9, 30 (2008).
40. C. Berger *et al.*, Electronic confinement and coherence in patterned epitaxial graphene. *Science* 312, 1191 (2006).
41. J. Kedzierski *et al.*, Epitaxial graphene transistors on SiC substrates. *IEEE Transactions on Electron Devices* 55, 2078 (2008).
42. J.-H. Chen, C. Jang, S. Xiao, M. Ishigami, M. S. Fuhrer, Intrinsic and extrinsic performance limits of graphene devices on SiO2. *Nature nanotechnology* 3, 206 (2008).
43. F. Chen, J. Xia, D. K. Ferry, N. Tao, Dielectric screening enhanced performance in graphene FET. *Nano Lett* 9, 2571 (2009).
44. S. Morozov *et al.*, Giant intrinsic carrier mobilities in graphene and its bilayer. *Physical review letters* 100, 016602 (2008).
45. F. Schwierz, Graphene transistors. *Nature nanotechnology* 5, 487 (2010).
46. K. V. Emtsev *et al.*, Towards wafer-size graphene layers by atmospheric pressure graphitization of silicon carbide. *Nature materials* 8, 203 (2009).
47. M. C. Lemme, T. J. Echtermeyer, M. Baus, H. Kurz, A graphene field-effect device. *IEEE Electron Device Letters* 28, 282 (2007).
48. X. Wang *et al.*, Room-temperature all-semiconducting sub-10-nm graphene nanoribbon field-effect transistors. *Physical review letters* 100, 206803 (2008).
49. M. Y. Han, B. Özyilmaz, Y. Zhang, P. Kim, Energy band-gap engineering of graphene nanoribbons. *Physical review letters* 98, 206805 (2007).
50. M. Kim, N. S. Safron, E. Han, M. S. Arnold, P. Gopalan, Electronic transport and Raman scattering in size-controlled nanoperforated graphene. *ACS nano* 6, 9846 (2012).
51. C. Stampfer *et al.*, Energy gaps in etched graphene nanoribbons. *Physical review letters* 102, 056403 (2009).
52. L. Yang, C.-H. Park, Y.-W. Son, M. L. Cohen, S. G. Louie, Quasiparticle energies and band gaps in graphene nanoribbons. *Physical review letters* 99, 186801 (2007).
53. L. Ponomarenko *et al.*, Chaotic Dirac billiard in graphene quantum dots. *Science* 320, 356 (2008).
54. J. Eroms, D. Weiss, Weak localization and transport gap in graphene antidot lattices. *New Journal of Physics* 11, 095021 (2009).

55. T. Shen *et al.*, Magnetoconductance oscillations in graphene antidot arrays. *Applied Physics Letters* 93, 122102 (2008).
56. A. Sinitskii, J. M. Tour, Patterning graphene through the self-assembled templates: toward periodic two-dimensional graphene nanostructures with semiconductor properties. *Journal of the American Chemical Society* 132, 14730 (2010).
57. M. Park, C. Harrison, P. M. Chaikin, R. A. Register, D. H. Adamson, Block copolymer lithography: periodic arrays of~ 1011 holes in 1 square centimeter. *Science* 276, 1401 (1997).
58. X. Liang *et al.*, Formation of bandgap and subbands in graphene nanomeshes with sub-10 nm ribbon width fabricated via nanoimprint lithography. *Nano Lett* 10, 2454 (2010).
59. S. Park *et al.*, Macroscopic 10-terabit–per–square-inch arrays from block copolymers with lateral order. *Science* 323, 1030 (2009).
60. S.-M. Park *et al.*, Sub-10 nm nanofabrication via nanoimprint directed self-assembly of block copolymers. *ACS nano* 5, 8523 (2011).
61. J. Bai, X. Zhong, S. Jiang, Y. Huang, X. Duan, Graphene nanomesh. *Nature nanotechnology* 5, 190 (2010).
62. M. Kim, N. S. Safron, E. Han, M. S. Arnold, P. Gopalan, Fabrication and characterization of large-area, semiconducting nanoperforated graphene materials. *Nano Lett* 10, 1125 (2010).
63. M. P. Stoykovich, P. F. Nealey, Block copolymers and conventional lithography. *Materials Today* 9, 20 (2006).

2. Direct Block copolymer self-assembly on silicon

This chapter was adapted from "Substrate tolerant direct block copolymer nanolithography," Tao Li, Zhongli Wang, Lars Schulte and Sokol Ndoni. Nanoscale, 2016, 8, 136–140, "Fast & scalable pattern transfer via block copolymer nanolithography," Tao Li, Zhongli Wang, Lars Schulte, Ole Hansen and Sokol Ndoni. RSC Adv., 2015, 5, 102619–10262 and "Synthesis and Characterization of Ferrocene Containing Block Copolymers. Journal of Polymer Science Part A: Polymer Chemistry." Sergey Chernyy, Zhongli Wang, Jacob Judas Kain Kirkensgaard, Anders Bakke, Kell Mortensen, Sokol Ndoni, Kristoffer Almdal. 2017, 55, 495–503.

2.1 Introduction

Direct self-assembly of block copolymers has received a great deal of research attentions as a promising nanolithography to complement the intrinsic limitations of conventional photolithography. In this chapter, we explored fully scalable and efficient block copolymers (BCPs) self-assembly directly on silicon substrate. Various advanced directed self-assembly approaches are examined. We presented our recent progress in the directed self-assembly of BCPs with a focus on guiding the assemblies of small features over large areas.

Block copolymer (BCP) self-assembly produces periodic microdomain features with dimensions of a few nanometers and above, making it a candidate for next generation lithography technique (*1-4*). Directed self-assembly (DSA) of block copolymers (BCPs) generates laterally ordered, periodic arrays of self-assembled spheres, cylinders, or lamellae with a typical feature size in the 3~50 nm region (*5-9*). The highly ordered self-assembled nanopatterns can be exploited for lithographic masks for parallel line arrays or hexagonal/-square dot arrays (*10-12*). As a result of prolonged research effort over the last three decades, DSA is attracting tremendous attention as a complementary technology for conventional photolithography with a variety of potential benefits,

such as molecular scale pattern precision, ultrafine line edge roughness (LER), and low-cost processing (*1, 13-18*).

The period of the microdomains in the BCP is given by $L_0 = aN^{2/3}\chi^{1/6}$ in the strong segregation limit, where "a" is the Kuhn monomer length, N is the degree of polymerization, and χ the Flory−Huggins interaction parameter (*5, 19*). The driving force for microphase separation increases with χN so to obtain microphase separation for small period BCPs, a high χ is required. Commonly studied polystyrene-block-polymethylmethacrylate (PS-PMMA) has $\chi \sim 0.06$ at room temperature limiting achievable periodicities to >∼24 nm (*20*). but high-χ BCPs, such as polystyrene-blockpolydimethylsiloxane (PS-PDMS, $\chi \sim 0.26$ at 300 K), can exhibit periodicities ∼10 nm or lower making them candidates for reaching the very small feature sizes required for next generation lithography (*21*).

Here we demonstrated an efficient BCP self-assembly procedure by using three PDMS-rich poly (styrene-b-dimethylsiloxane) (PS-b-PDMS) copolymers, two PS-rich poly (styrene-b-dimethylsiloxane) (PS-b-PDMS) copolymers, two organic polymers (poly (styrene-b-2-vinyl pyridine) and poly (styrene-b-2-vinyl pyridine)) copolymers and one ferrocene containing copolymer PF9MA-PFMMA ($PF9_{35k}F_{25}$). Due to the large inter-block segregation and high etching contrast; PS-b-PDMS is strong candidate for sub-10 nm lithography. The masks are directly applied on substrates which have broad different surface energy, such as polymers, silicon and graphene. For PDMS-rich PS-b-PDMS copolymers, the perpendicular PS cylinder in the sub-20 nm thin film is kinetically captured by annealing in vapors of selective solvents (selective PDMS block). An oxygen plasma treatment enables formation of the oxidized PDMS hard mask, PS block removal and polymers or graphene substrate patterning after few seconds fluorine plasma treatment. PS-rich PS-b-PDMS copolymers have the same procedure. However selectively removal block A from diblock copolymer A-b-B template is not a simple task. Most BCPs are made of organic materials,

where they lack etching contrast between different blocks. Simple oxygen RIE removes both organic polymer blocks at the similar rate, leaving a flat film that unsuitable for further pattern transfer. Thus, we also discussed the organic BCP systems PS-b-P2VP and PS-b-P4VP BCPs, a reconstruction process to enhance the etch contrast between two organic blocks in this chapter. In addition, we discussed a new block copolymer PF9MA-PFMMA ($PF9_{35k}F_{25}$) hexagonally packed cylinder morphology by using this efficacy annealing method. Our procedure improves and simplifies the traditional BCP by combining kinetic control, sub-lattice thickness confinement and selective solvent annealing as the key elements.

2.2 Experimental

Materials and sample preparation

In this study, all the solvents are purchased from Sigma Aldrich without further purification. SD67 (21-b-46 kg mol^{-1}), S2VP44.5 (32.5-b-12 kg mol^{-1}) and S4VP24 (19-b-5 kg mol^{-1}) are purchased from Polymer Source Inc. and used without further purification. SD42 (13-b-29 kg mol^{-1}), SD39 (27-b-12 kg mol^{-1}), SD165 (144.5-b-20.5 kg mol^{-1} and SD23 (7-b-16 kg mol^{-1}) are synthesized by living anionic polymerization following already reported procedure (*22*). After precipitation in methanol and vacuum drying, SD23, SD42 and SD67 are all dissolved in heptane (2-5wt %). Transparent solutions are obtained in heptane, despite of it is a nonsolvent for PS; These BCPs form micelles in such conditions. However, the solutions turn turbid after a residence time of 10-20 hours, and the undissolved solids are removed by centrifugation. This step is essential for a reliable following self-assembly process, since we find that even a small amount of unreacted PS impurity makes the whole process less robust. SD39 was dissolved in cyclohexane at a concentration of 0.25 wt. % and was spin-cast directly onto the substrate at 2000 rpm for 30 seconds to give a 15 nm thin film. Monolayer cylinder morphology formed after appropriate solvent annealing of the SD39 film (solvent vapor of 1, 4-dioxane), following the procedure reported in our lab (*23*). SD165 was

dissolved in cyclohexane at a concentration of 0.2 wt. % and was spin-cast directly onto the substrate at 2000 rpm for 30 seconds to give a 13 nm thin film. Monolayer sphere morphology formed after appropriate solvent annealing of the SD165 film (mix solvents vapor of cyclohexene/xylene, 5/1). SVPs were dissolved in a mixture of toluene and THF to form a uniform solution. $PF9_{35k}F_{25}$ (PF9MA-b-PFMMA) is synthesized by anionic polymerization and was directly applied on silicon substrate without any pretreatment by spin-coating from 0.1 wt. % toluene solution at 2000 rpm for 30 s to give a 12 nm thin film.

Table 2.1 List of BCPs with different molecular weights used in this chapter

Sample ID	*Molecular weight**	PDI
SD23	7- *b* -16	1.02
SD42	13- *b* -29	1.02
SD67	21- *b* -46	1.45
SD39	27- *b* -12	1.03
SD165	144.5- *b* -20.5	1.05
S2VP44.5	32.5- *b* -12	1.05
S4VP24	19- *b* -5	1.10
$PF9_{35k}F_{25}$	26- *b* -9	1.03

Characterization

In our lab, we always use the standard characterized methods to study our samples. For example, we use VASE Ellipsometer (J.A. Woollam) at three different incidence angles (55^o, 60^o and 65^o) to measure film thickness. We use Field Emission Zeiss Ultra Plus scanning electron microscope with a Gemini column operating at an accelerating voltage of 2kV to take scanning electron microscopy (SEM) images. All the samples are scanned directly without coating or staining. Atomic Force Microscopy (AFM) images are taken by an AFM Dimension Icon-PT from Bruker AXS. The annealing process is followed in situ by a quartz crystal microbalance QCM 200 digital controller connected to a QCM 25 crystal oscillating at 5 MHz from Stanford Research Systems.

2.3 Results and discussion

Self-assembly of PDMS-rich PS-b-PDMS

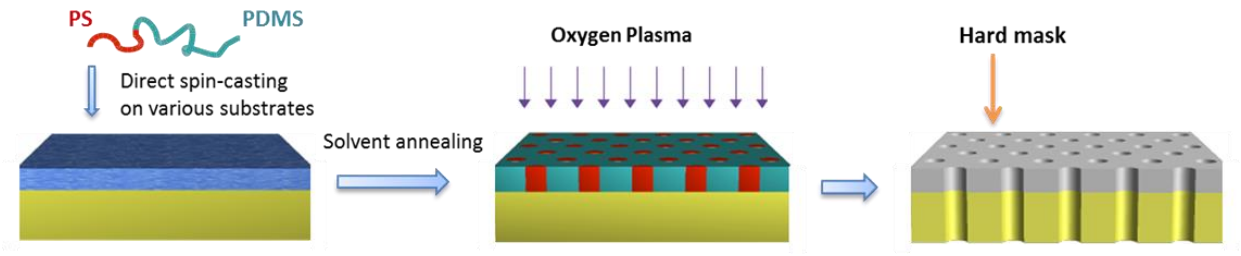

Figure 2.1 Schematic of direct BCPs nanolithography. SDs are directly cast on various substrates.

First three SDs with different M_n from 23.4 to 67.0 kg/mol are investigated, SD solutions in heptane are spin-cast into sub-20 nm thin films on silicon. Figure 2.2 a, b show the top view scanning electron microscopy (SEM) images of SD23 and SD42 after annealing. A well-ordered hexagonally packed cylinder morphology with narrow PS-cylinder size distribution is clearly seen, which can be visualized directly in SEM. A SEM image of SD67 after annealing is shown in Figure 2.2c, with the same morphology but lacking in lateral order, which might be due to its large PDI.

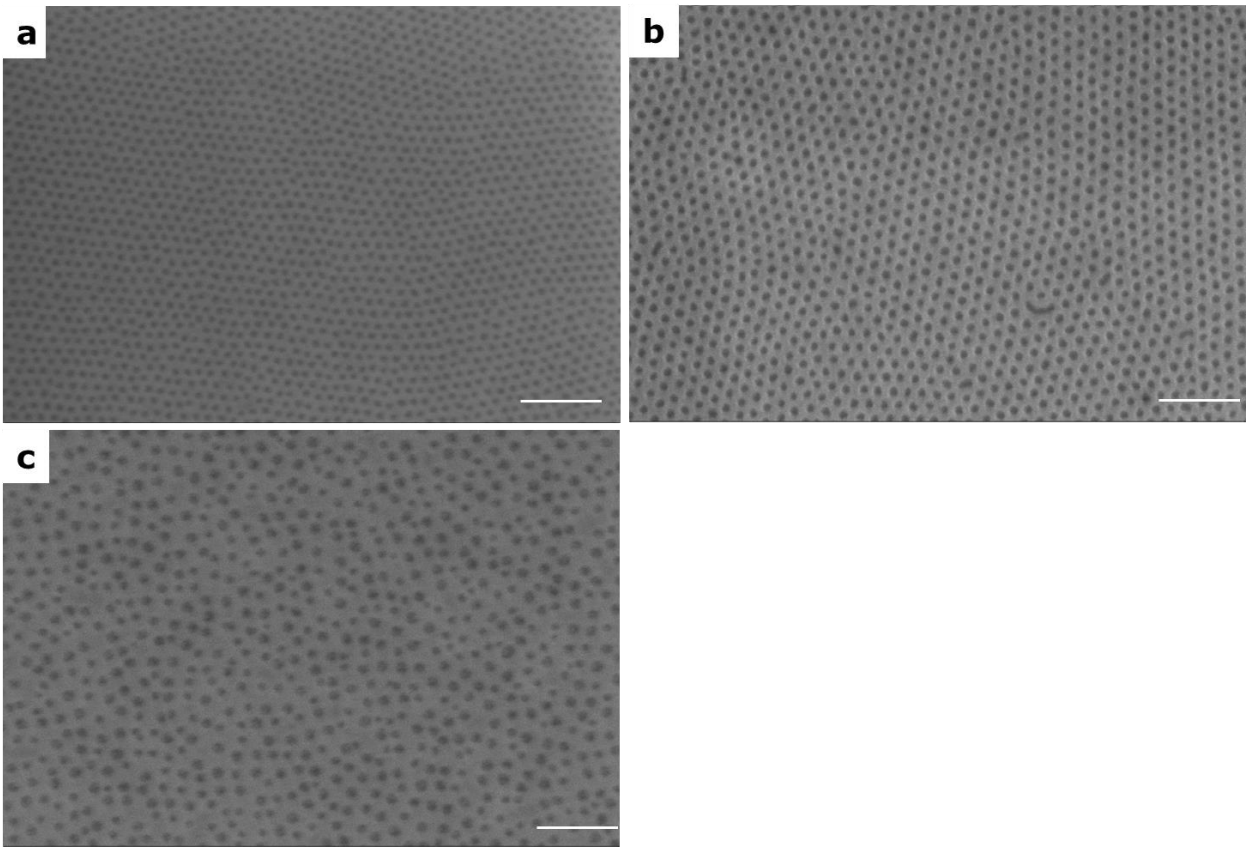

Figure 2.2 Top view SEM images of the masks after annealing: (a) SD23 annealed in TMPA for 40 minutes with a thickness of 13.5 nm, (b) SD42 annealed in hexane for 40 minutes with a thickness of 15.8 nm, (c) SD67 annealed in 1-octene for 90 minutes with a thickness of 19.1 nm, Scale bars: 200 nm.

Compared with the morphologies of as cast films or of films after thermal annealing (Figure 2.3a, b), it clearly shows that the solvent annealing is effective on directing the SD self-assembly over wafer-scale with micrometer grain size (Figure 2.3c). The corresponding period scales with the 0.6^{th} power of BC molecular weights. A wide range of the pore size from 13 nm (SD23) to 30 nm (SD67) is obtained. Common shortcomings of solvent vapor annealing, such as dewetting and deformation of the structures, (*24*) are not observed in this study due to the limited PS chain mobility in the presence of a nonsolvent.

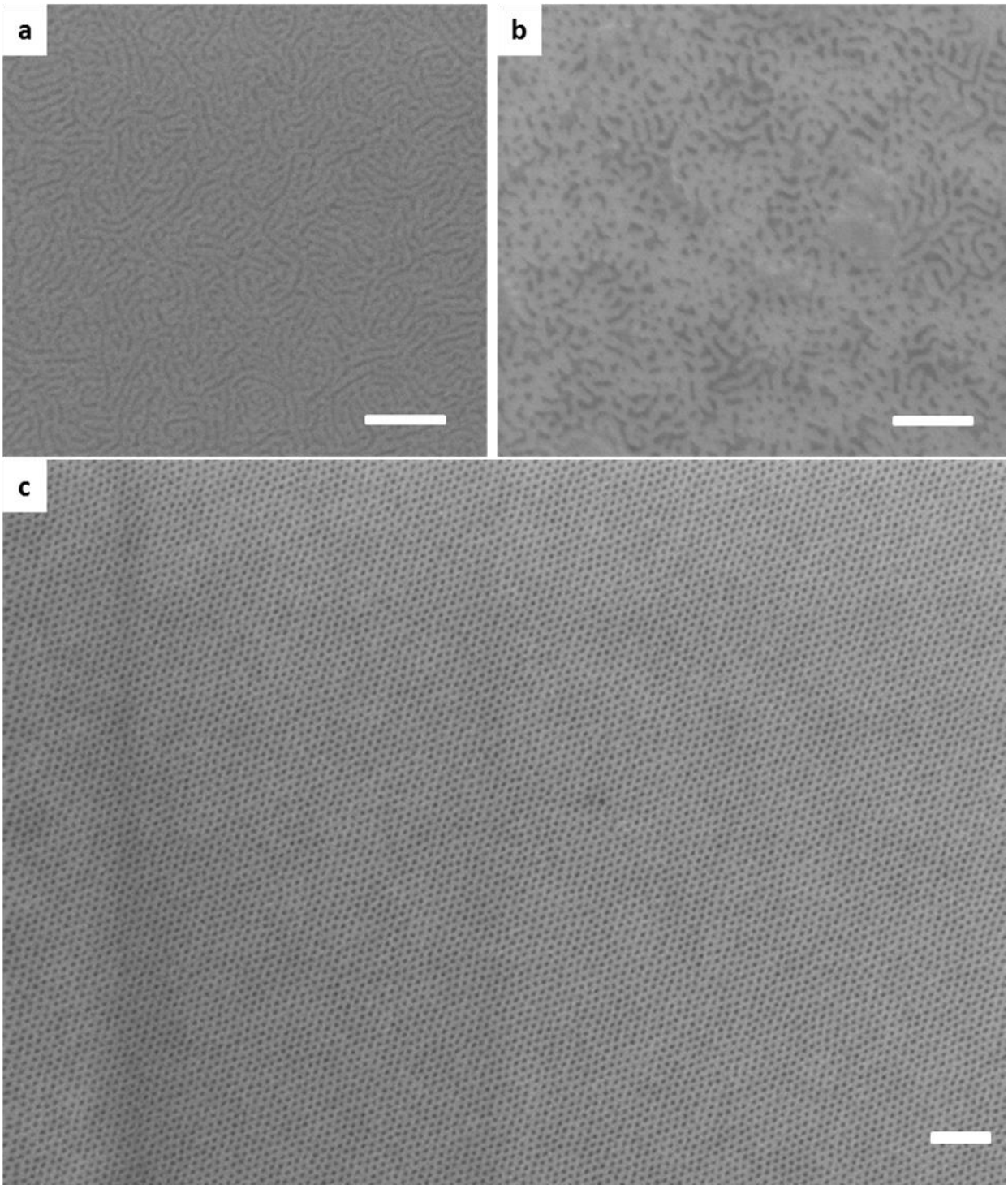

Figure 2.3 SEM image of the (a) SD42 as cast on silicon substrate; the shown morphology is similar for all the SDs after spin-casting, (b) SD42 thermal annealed at 160^{o}C for 15 hours and (c) SD42 annealed in hexane for 40 minutes with the grain size exceeding 4 um. Scale bar: 200 nm.

From Figure 2.4 we find that the film morphology is strongly dependent on the film thickness and the annealing solvent. For an example (Figure 2.4a), when the film thickness is beyond the ideal range (14.5-16.5 nm), defects easily present. Similar results are also observed when the annealing solvent is changed, as shown in Figure 2.5; the transition of the horizontal cylinder to perpendicular cylinder is captured. By annealing under vapors of the slightly more selective solvent to PS block, 1-octene ($\Delta\delta_{PS\text{-}1\text{-}octene} = 3.0$), instead of hexane ($\Delta\delta_{PS\text{-}hexane} = 3.6$), the perpendicular cylinder phase seems to be the equilibrium state. The film is homogeneous and no sphere phase is observed for 4 hours (longer annealing time not tested).

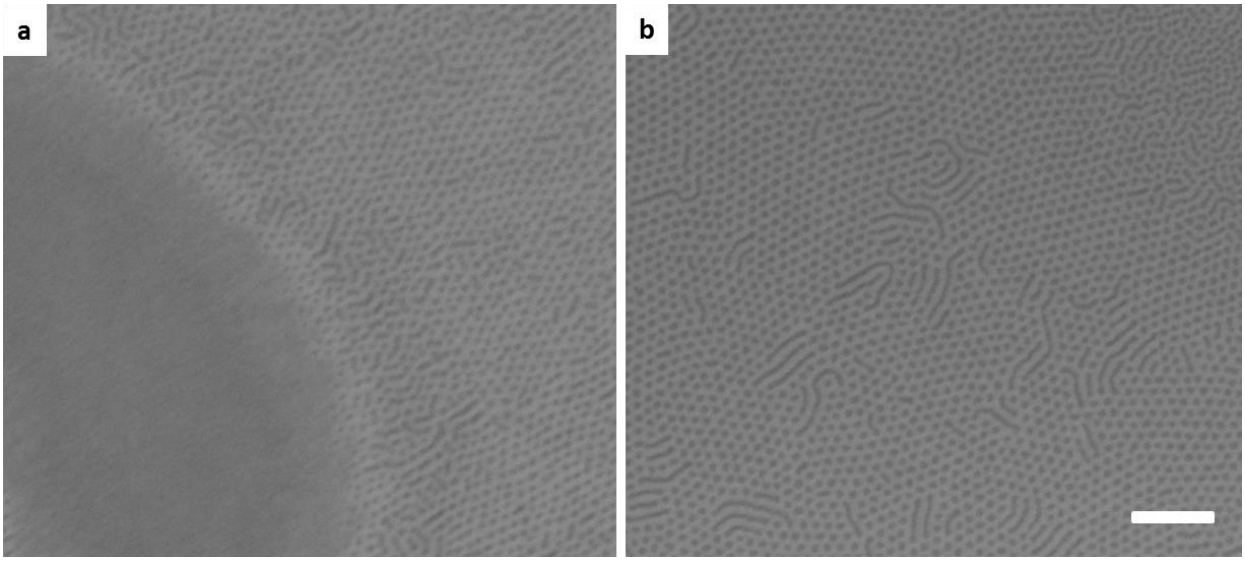

Figure 2.4 SEM images of the SD42 annealed in hexane for 30 minutes with a thickness of (a) 13.2 nm and (b) 16.9 nm, Scale bar: 200 nm.

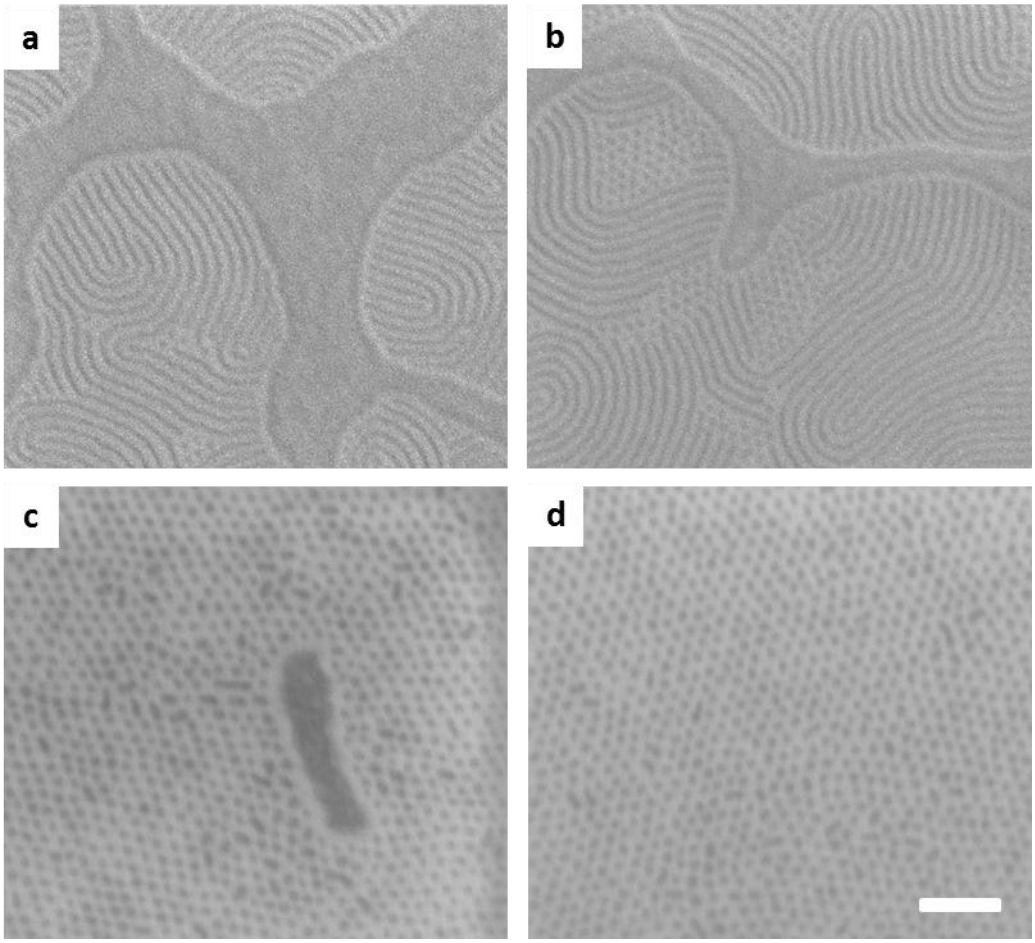

Figure 2.5 SEM images of the SD42 annealed in 1-octene for (a) 15 minutes, (b) 30 minutes, (c) 1 hour and (d) 4 hours, Scale bar: 200 nm.

Self-assembly of PS-rich PS-b-PDMS

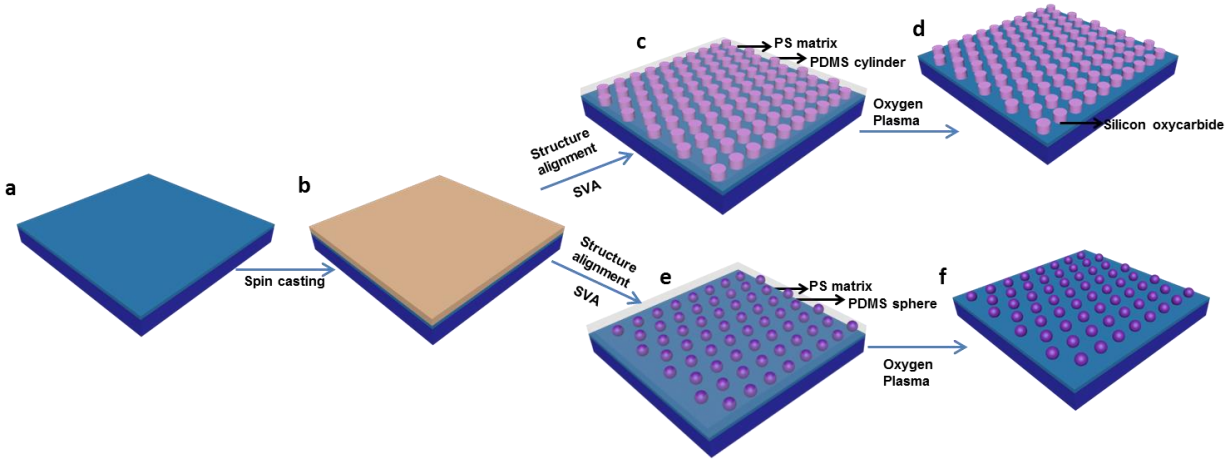

Figure 2.6 Schematic workflow of direct PS-rich SDs nanolithography. (a) SiO_2/Si substrate. (b) Spin coating of block copolymer thin film directly on SiO_2/Si substrate. (c, e) Structure alignment of block copolymer via solvent vapor annealing. (d, f) Fabrication of hard silicon oxycarbide nanocylinder/nanosphere array through oxidation of PDMS, simultaneous removal of PS and etching of graphene under oxygen plasma.

Figure 2.6 shows the overall nanodisk arrays fabrication process. First the polystyrene-*b*-polydimethylsiloxanes (PS-PDMS) were directly spin-cast on a SiO_2/Si substrate without any preliminary surface modification (like e.g. the ubiquitous surface grafting of a brush layer (*25*). The morphologies formed at different conditions of solvent vapor annealing were investigated by SEM and AFM. Figure 2.7 shows top view SEM images of SD39 after two different conditions of annealing. The ordering behavior exhibits strong solvent dependence and the difference in the solubility of the PS and PDMS blocks gives a possibility to further manipulate the domain size and separation distances in thin films. Selective (to the PS domain) solvent vapor (1, 4-dixoane) annealing (SVA) was then applied to generate well-ordered vertical hexagonal cylinder morphology over a large area. The following O_2 dry etching enables simultaneous formation of the hard silicon oxycarbide nanocylinder by oxidation of the PDMS block, removal of the PS block. Morphology of well-ordered horizontal cylinders is clearly seen upon annealing in saturated solvent vapor of toluene for 30 min (Figure 2.7 c, d). The reason for the change in the orientation of morphologies in different annealing solvent vapors can be explained in terms of the difference in solvent selectivity and solvent saturated vapor pressure. Since 1, 4-dixoane only swells but does not dissolve the PDMS block it could be considered a more selective solvent for the PS block. Therefore, in the presence of a selective solvent (1, 4-dixoane) the surface interactions are screened to a larger extent for PS block but not for PDMS block and, thus, specific adsorption of the PDMS onto the substrate induces perpendicular cylinder orientation. On the contrary, when nonspecific solvent is present

(toluene) both blocks are well solvated, their mutual segment-segment interactions become screened to a certain extent while their surface interactions appear to be totally balanced ("neutral surface") resulting in the parallel with respect to the substrate orientation of the cylinders.

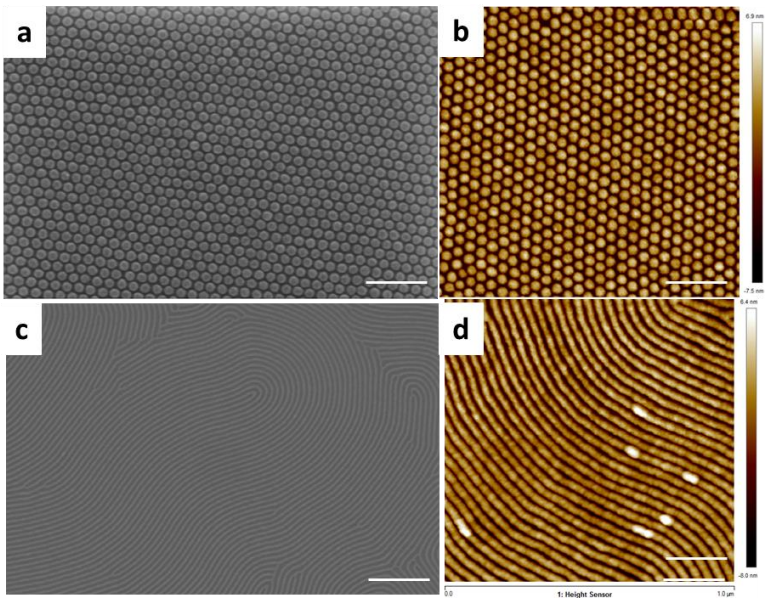

Figure 2.7 (a-b) SEM and AFM images of silicon oxycarbide nanocylinders mask on SiO_2/Si substrate, (c-d) SEM and AFM images of silicon oxycarbide nanoribbons mask on SiO_2/Si substrate. Scale bars: 200 nm.

SD165 was dissolved in cyclohexane at a concentration of 0.2 wt. % and was spin-cast directly onto the substrate at 2000 rpm for 30 seconds to give a 13 nm thin film. Monolayer sphere morphology formed after appropriate solvent annealing of the SD165 film (mix solvents vapor of cyclohexene/xylene, 5/1). The self-assembled BCPs are transformed into hard lithography masks by oxidation of PDMS under oxygen plasma (Figure 2.8 a, b).

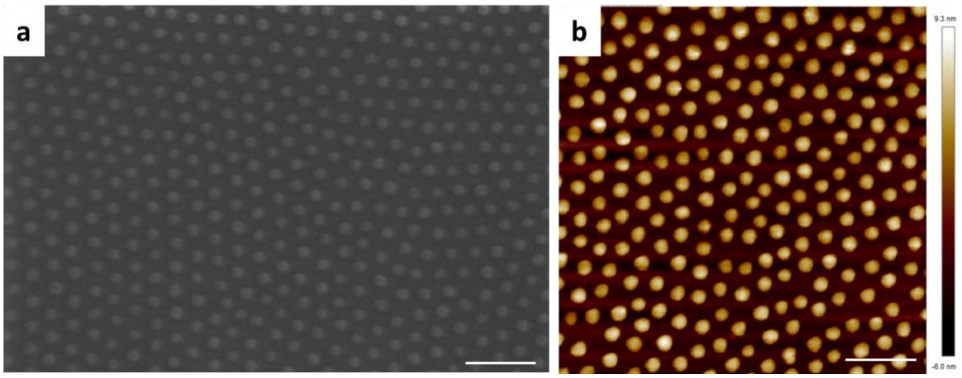

Figure 2.8 (a-b) SEM and AFM images of silicon oxycarbide nanospheres mask on SiO_2/Si substrate. Scale bars: 200 nm.

Self-assembly of PS-b-PVP

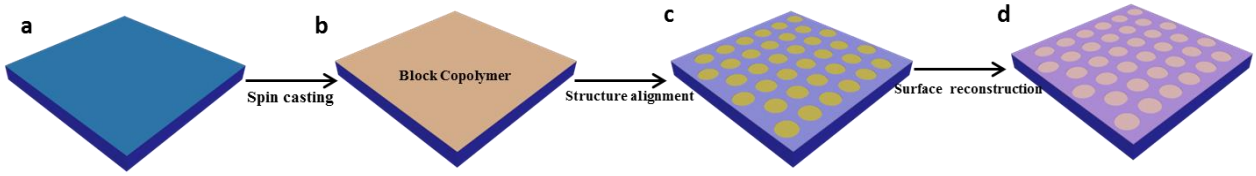

Figure 2.9 Schematic procedure of direct BCPs nanolithography. SVPs are directly cast on various substrates.

Figure 2.9 shows the schematic process of fabricating porous BCP templates. S2VP44.5 and S4VP24 are spin-coated onto silicon wafers and solvent annealed in different solvent, to self-assemble the BCP into hexagonally packed PVP cylindrical domains normal to substrate surrounded by a PS matrix (Figure 2.9c). The film is treated with ethanol, which selectively swell the PVP domains to reconstruct the film. As the solvent dries, the PVP domains collapse onto the sidewalls and top surface of the PS matrix, creating pores in the film (Figure 2.9d).

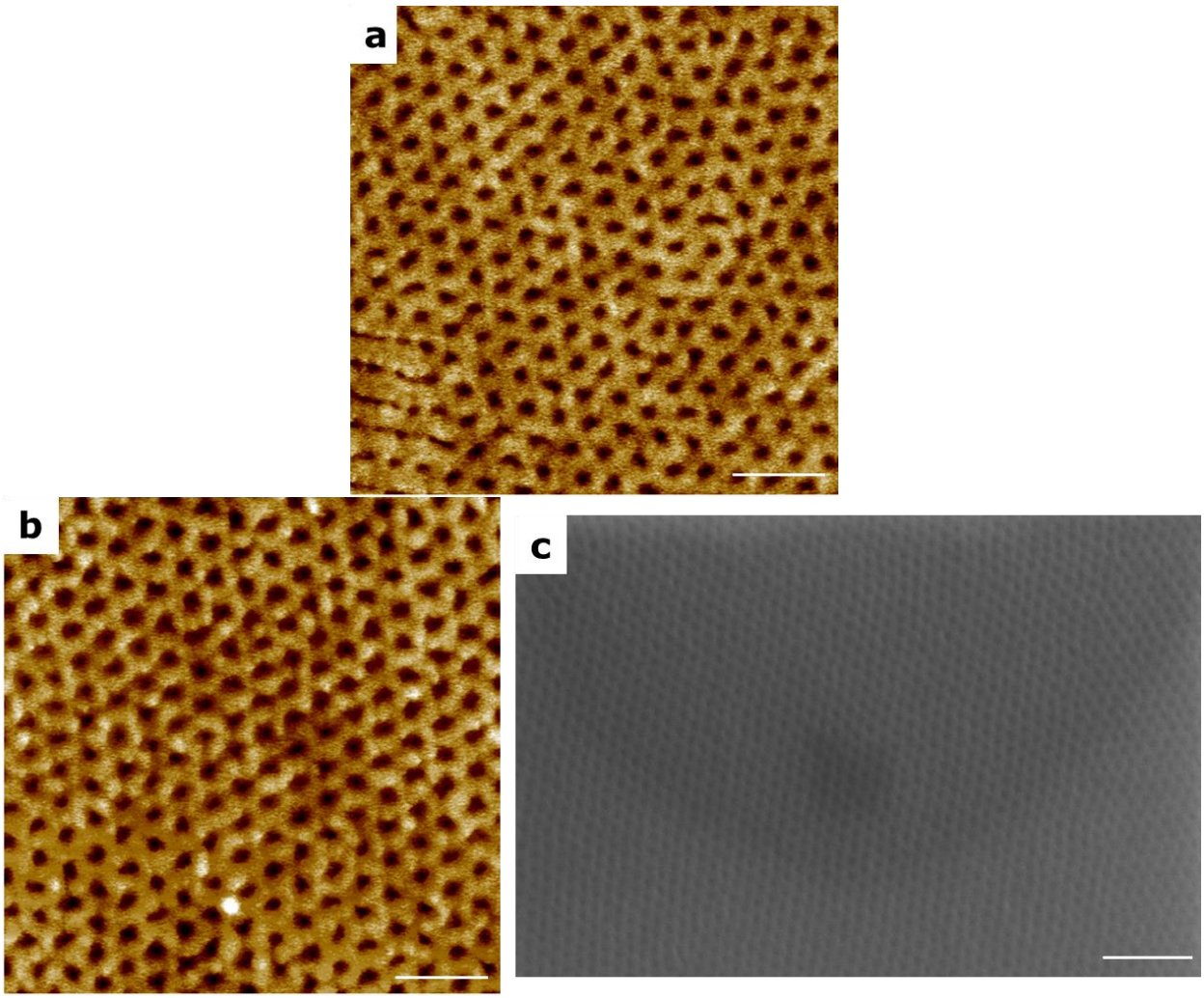

Figure 2.10 a) AFM image of the S2VP44.5 pattern after solvent annealing. b) And c) AFM and SEM image of the S2VP44.5 pattern after reconstruction in ethanol. Scale bar: 200 nm.

Figure 2.10 shows AFM height images and SEM images of the surface topography of S2VP44.5 films annealed in ethyl benzoate for 90 minutes and then, subsequently reconstructed in ethanol. The solubility parameter for ethyl benzoate is 16.8 $(MPa)^{1/2}$, for PS it is 18.5$(MPa)^{1/2}$ and for P2VP it is 20.4$(MPa)^{1/2}$(*26*). Ethyl benzoate is a nonsolvent for the PS block and P2VP block. In the ethyl benzoate-annealed films, the P2VP microdomains are oriented parallel to the surface and embedded in a PS matrix. There is only a ~1 nm height difference that indicates the location of the P2VP microdomains. So it is hardly to observe the morphology under SEM. We used AFM to investigate the surface morphology of S2VP44.5 (Figure 2.10a) and found it highly ordered. After

reconstruction, the swelling of the P2VP microdomains by ethanol amplifies this height difference. (Figure 2.10b, c).

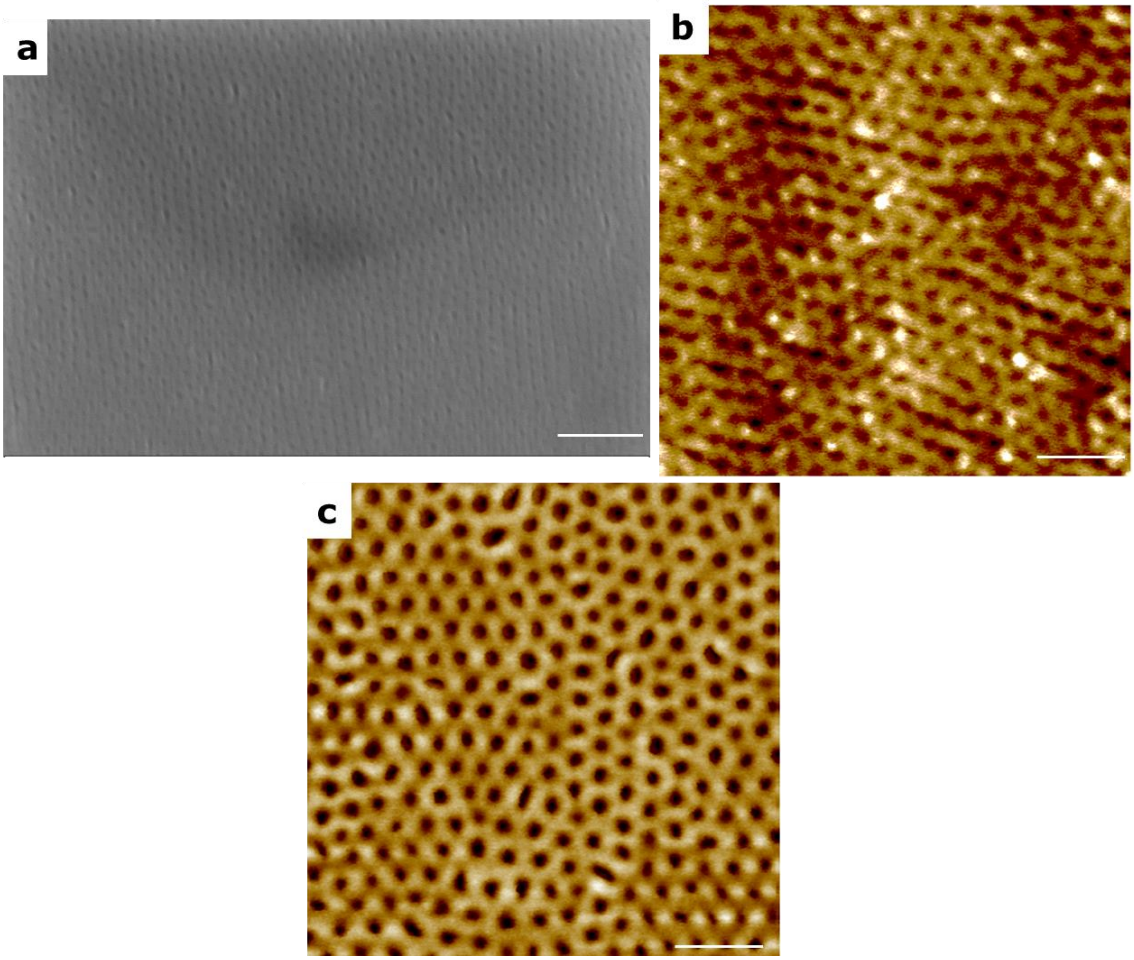

Figure 2.11 a) And b) SEM and AFM image of the S4VP24 pattern after solvent annealing, c) AFM image of the S4VP24 pattern after reconstruction in ethanol. Scale bar: 200 nm.

In addition, we demonstrate the generality of this reconstruction and etching methodology, using a S4VP24 BCP to form nanoholes. By using THF, the S4VP24 was solvent annealed to form cylindrical microdomains oriented normal to the surface of the film (Figure 2.11a, b). After the film was reconstructed in ethanol, porous films were formed on the silicon (Figure 2.11c). Most of the PVP was displaced to the surface, while a small fraction, due to the bonding to the PS block, remained in the nanohole. In order to open the nanoholes completely, we used 3 seconds oxygen

plasma to directly etch the reconstructed S4VP24 thin film, we found that the contrast is clear and the deep of the nanoholes changed from 6.4 nm to 7.8 nm (Figure 2.12).

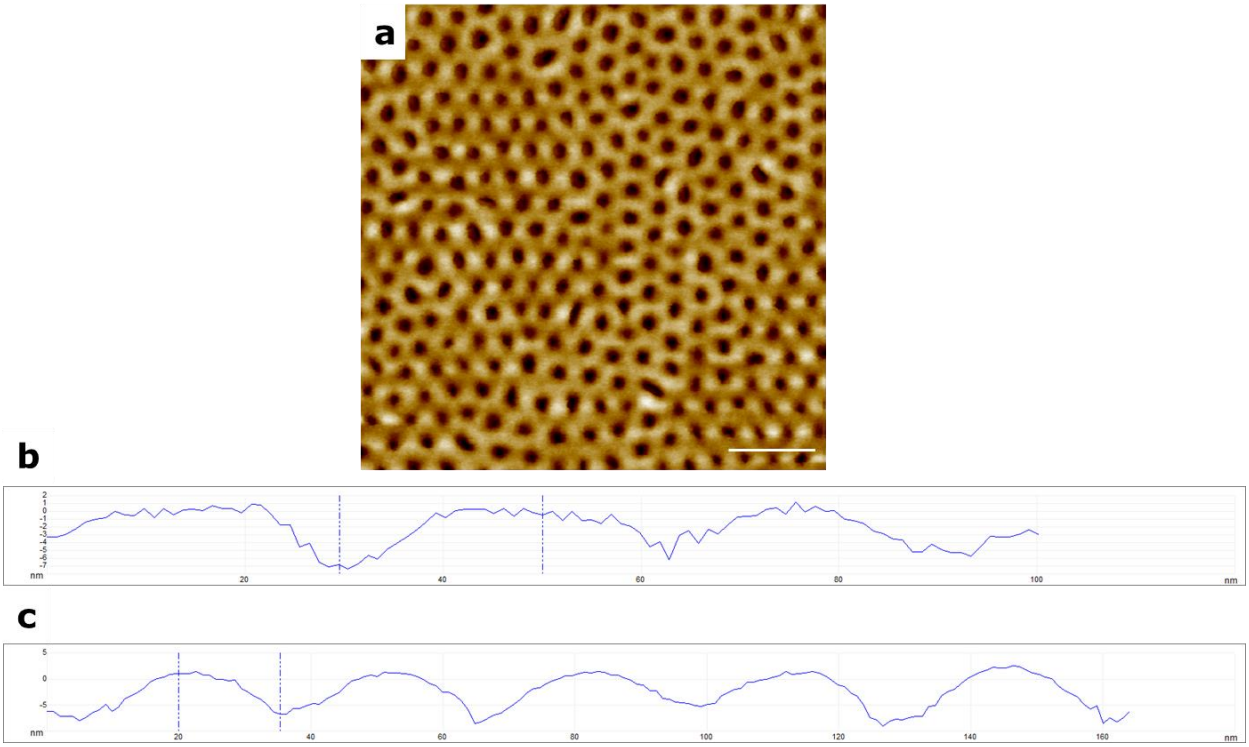

Figure 2.12 a) AFM image of the S4VP24 pattern after 3 s oxygen plasma, b) Height profile of the S4VP24 pattern after reconstruction in ethanol, c) Height profile of the S4VP24 pattern after 3s oxygen plasma treatment. Scale bar: 200 nm.

Self-assembly of $PF9_{35k}F_{25}$ copolymer

In order to explore the widespread of procedure which we developed above, we selected anionic polymerization for the synthesis of diblock copolymers of ferrocenylmethyl methacrylate (FMMA) and 1H, 1H, 2H, 2H-nonafluorohexyl methacrylate (F9MA), with the aim to further investigate the bulk and surface morphologies of the resulting novel block copolymers by means of TEM, SEM, SAXS, Rheology, and AFM. Here we only talk about $PF9_{35K}F_{25}$ block copolymer thin film morphology using SEM and AFM. The other part discussion was studied by my colleague.

$PF9_{35k}F_{25}$ copolymer was directly applied on silicon substrate without any pretreatment by spin-coating from 0.1 wt. % toluene solution at 2000 rpm for 30 s to give a 12 nm thin film. The

morphologies formed at different conditions of solvent vapor annealing were investigated by SEM and AFM. Figure 2.13 shows top view SEM images of $PF9_{35k}F_{25}$ after three different conditions of annealing. The ordering behavior exhibits strong solvent dependence and the difference in the solubility of the PFMMA and PF9MA blocks gives a possibility to further manipulate the domain size and separation distances in thin films.

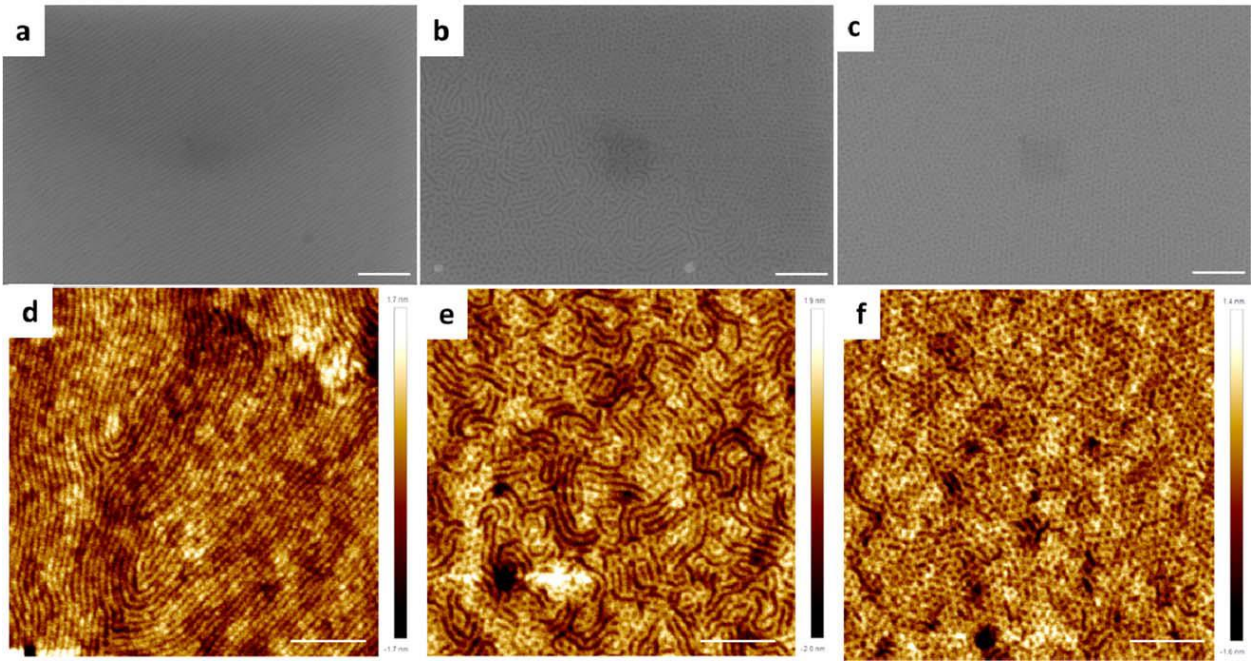

Figure 2.13 SEM (top-row) and AFM (bottom-row) images of $PF9_{35K}F_{25}$ on SiO2/Si substrate after annealing for 20 min in (a, d) ethyl acetate atmosphere, (b, e) EA/THF atmosphere, and (c, f) THF atmosphere. Scale bars correspond to 100 nm.

Morphology of well-ordered lateral cylinders with 19 nm period is clearly seen upon annealing in saturated solvent vapor of ethyl acetate for 20 min (Figure 2.13). The 19 nm period is in a good agreement with an equilibrium domain spacing (d) which was estimated by SAXS to be equal to 19.3 nm. When ethyl acetate/THF (v/v55/1) mixture was used for the solvent annealing for 20 min, a mixed morphology containing cylinders of both parallel and perpendicular orientations was observed (Figure 2.13b,e). Furthermore, well-ordered hexagonally packed cylinders perpendicular to the substrate surface were observed when the film was annealed in pure THF vapor for 20 min

(Figure 2.13c, f). The reason for the change in the orientation of morphologies in different annealing solvent vapors can be explained in terms of the difference in solvent selectivity and solvent saturated vapor pressure. The perpendicular orientation of HEX morphology requires the underlying surface to be neutral. Since ethyl acetate only swells but does not dissolve the PFMMA block it could be considered a more selective solvent for the PF9MA block. Therefore, in the presence of a selective solvent (ethyl acetate) the surface interactions are screened to a larger extent for PF9MA block but not for PFMMA block and, thus, specific adsorption of the PFMMA onto the substrate induces parallel cylinder orientation. On the contrary, when nonspecific solvent is present (THF) both blocks are well solvated, their mutual segment-segment interactions become screened to a certain extent while their surface interactions appear to be totally balanced ("neutral surface") resulting in the perpendicular with respect to the substrate orientation of the cylinders.

2.4 Conclusions

In summary, we have demonstrated a novel BCP nanolithography process using several BCPs with perpendicular orientation by selective solvent vapor annealing. The highly ordered morphology is captured via kinetic control of BCP assembly and efficacy solvent evaporation. The BCP mask can be directly applied on silicon substrate without brush layer or top coats, which greatly simplifies the lithography process. The choice of the annealing solvents, film thickness and annealing time play a important role in determining the final structure. For PS-b-PDMS BCPs, Removal of PS domain, hardening of PDMS domain and pattern transfer can be achieved at the same time by using a simple dry etch process. This BCPs self-assembly nanolithography provides many potential application such as thin film patterning, membrane separation, nanostructured materials, sensors (27-*29*), and so on. We have also shown that a simple reconstruction of the organic BCPs can provide etching contrast and allows the patterning of BCP mask for subsequent pattern transfer into the underlying substrate. Finally we discuss a new block copolymer PF9MA-PFMMA ($PF9_{35k}F_{25}$) hexagonally

packed cylinder morphology by using this efficacy annealing method. Some of those BCPs self-assembly and lithography will be used in the following chapters.

2.5 References

1. R. Ruiz *et al.*, Density multiplication and improved lithography by directed block copolymer assembly. *Science* **321**, 936 (2008).
2. M. P. Stoykovich *et al.*, Directed assembly of block copolymer blends into nonregular device-oriented structures. *Science* **308**, 1442 (2005).
3. S.-M. Park *et al.*, Sub-10 nm nanofabrication via nanoimprint directed self-assembly of block copolymers. *ACS nano* **5**, 8523 (2011).
4. S. Darling, Directing the self-assembly of block copolymers. *Progress in Polymer Science* **32**, 1152 (2007).
5. F. S. Bates, G. H. Fredrickson, Block copolymer thermodynamics: theory and experiment. *Annual review of physical chemistry* **41**, 525 (1990).
6. G. H. Fredrickson, F. S. Bates, Dynamics of block copolymers: theory and experiment. *Annual Review of Materials Science* **26**, 501 (1996).
7. F. S. Bates, G. H. Fredrickson, Block copolymers—designer soft materials. *Physics today* **52**, 32 (1999).
8. M. Malkoch *et al.*, Structurally diverse dendritic libraries: a highly efficient functionalization approach using click chemistry. *Macromolecules* **38**, 3663 (2005).
9. J. K. Kim, S. Y. Yang, Y. Lee, Y. Kim, Functional nanomaterials based on block copolymer self-assembly. *Progress in Polymer Science* **35**, 1325 (2010).
10. G. Xia *et al.*, Spin coating nanopatterned multielemental materials via self-assembled nanotemplates. *Nanotechnology* **20**, 225301 (2009).
11. B. H. Kim *et al.*, Mussel‐Inspired Block Copolymer Lithography for Low Surface Energy Materials of Teflon, Graphene, and Gold. *Advanced Materials* **23**, 5618 (2011).
12. B. H. Kim, J. Y. Kim, S. O. Kim, Directed self-assembly of block copolymers for universal nanopatterning. *Soft Matter* **9**, 2780 (2013).
13. C. Tang, E. M. Lennon, G. H. Fredrickson, E. J. Kramer, C. J. Hawker, Evolution of block copolymer lithography to highly ordered square arrays. *Science* **322**, 429 (2008).
14. S. O. Kim *et al.*, Novel complex nanostructure from directed assembly of block copolymers on incommensurate surface patterns. *Advanced Materials* **19**, 3271 (2007).
15. I. Bita *et al.*, Graphoepitaxy of self-assembled block copolymers on two-dimensional periodic patterned templates. *Science* **321**, 939 (2008).
16. J. K. Yang *et al.*, Complex self-assembled patterns using sparse commensurate templates with locally varying motifs. *Nature nanotechnology* **5**, 256 (2010).
17. B. H. Kim *et al.*, Spontaneous Lamellar Alignment in Thickness‐Modulated Block Copolymer Films. *Advanced Functional Materials* **19**, 2584 (2009).
18. D. O. Shin *et al.*, One-dimensional nanoassembly of block copolymers tailored by chemically patterned surfaces. *Macromolecules* **42**, 1189 (2009).
19. L. Leibler, Theory of microphase separation in block copolymers. *Macromolecules* **13**, 1602 (1980).
20. T. L. Bucholz, Y.-L. Loo, Phase behavior of near-monodisperse semifluorinated diblock copolymers by atom transfer radical polymerization. *Macromolecules* **39**, 6075 (2006).

21. S. Park *et al.*, Macroscopic 10-terabit–per–square-inch arrays from block copolymers with lateral order. *Science* **323**, 1030 (2009).
22. S. Ndoni, P. Jannasch, N. B. Larsen, K. Almdal, Lubricating effect of thin films of styrene-dimethylsiloxane block copolymers. *Langmuir* **15**, 3859 (May 25, 1999).
23. T. Li, Z. Wang, L. Schulte, O. Hansen, S. Ndoni, Fast & scalable pattern transfer via block copolymer nanolithography. *RSC Advances* **5**, 102619 (2015).
24. M. Y. Paik *et al.*, Reversible Morphology Control in Block Copolymer Films via Solvent Vapor Processing: An in Situ GISAXS Study. *Macromolecules* **43**, 4253 (May 11, 2010).
25. R. A. Farrell *et al.*, Large-scale parallel arrays of silicon nanowires via block copolymer directed self-assembly. *Nanoscale* **4**, 3228 (2012).
26. C. M. Hansen, *Hansen solubility parameters: a user's handbook*. (CRC press, 2007).
27. M. E. Warkiani *et al.*, Isoporous micro/nanoengineered membranes. *Acs Nano* **7**, 1882 (Mar 26, 2013).
28. B. N. Miles *et al.*, Single molecule sensing with solid-state nanopores: novel materials, methods, and applications. *Chem Soc Rev* **42**, 15 (Jan 7, 2013).
29. A. de la Escosura-Muniz, A. Merkoci, Nanochannels preparation and application in biosensing. *Acs Nano* **6**, 7556 (Sep 25, 2012).

3. Graphene nanopatterning with sub-10 nm resolution via selective-area photocatalysis

This chapter was adapted from "Photocatalytic Nanostructuring of Graphene Guided by Block Copolymer Self-Assembly," Zhongli Wang,†,‡ Tao Li,,† Lars Schulte,†,‡ Kristoffer Almdal,†,‡ and Sokol Ndoni*,†,‡ ACS Appl. Mater. Interfaces 2016, 8, 8329−8334.*

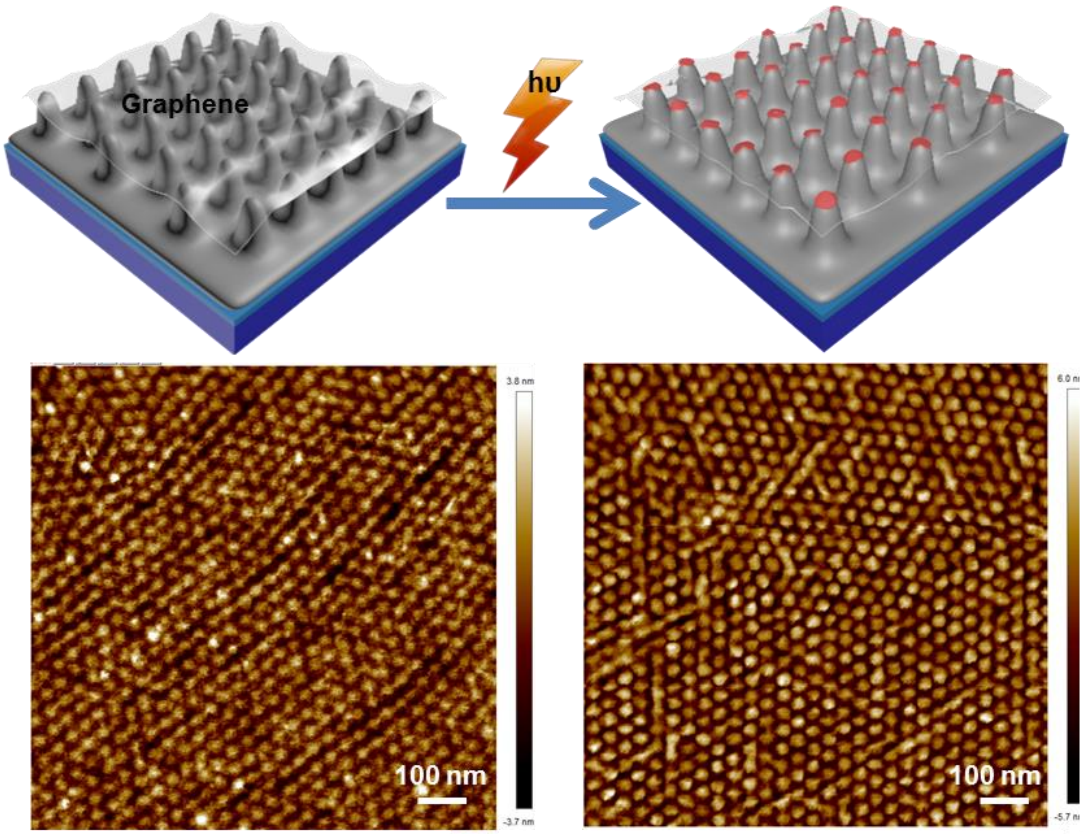

3.1 Introduction

Since 2004 graphene has attracted a wide range of interests due to its fascinating electronic, optical, mechanical, and thermal properties (*1*). Graphene provides a great opportunity especially for the development of high-performance electronic devices because of its extremely high carrier mobility, flexibility, transparency and chemical stability (*2*). However, it is a semimetal with intrinsic zero bandgap which prohibits to achieve high on/off current ratios required for field-effect transistors (*3-5*). Many efforts so far have focused on the creation of an energy bandgap by cutting graphene into

nanomesh (*6*) and nanoribbons (*7*). Nanopatterned graphene shows also a high potential as sensor for enhanced gas sensitivity (*8*) and as atomic-layer separation membranes (*9*). Moreover, nanopatterned graphene can be used to control the absorption of infrared light (*10*), as well as substrate for plasmonics (*11*). To date, several approaches have been reported for fabricating graphene superlattices (*6, 12*). Most of these methods are based on the use of lithography masks in complicated and time-consuming procedures. The limited controllability and/or lack of scalability as well as the complicated and time-consuming procedures of these approaches call for more effective and breakthrough on graphene engineering for graphene electronics.

It was recently shown that carbon bonds of graphene can be cut by oxidation (*13*). Oxidation and decomposition of carbonaceous materials, using metal oxide semiconductor photocatalysts, such as TiO_2 and ZnO, are well-known (*14-17*). Patterned photodegradation of graphene by nanostructured photocatalysts is an emerging procedure to produce graphene nonomesh. TiO_2 has been considered as one of the most promising photocatalytic materials for solar energy conversion and environmental purification (*18, 19*) due to its low cost, high stability, and long life-time of photogenerated carrier. The bonds of Ti-O become weaken and oxygen vacancies generate because the large bandgap (3.0 eV for rutile and 3.2 eV for anatase) of TiO_2 are matched with photogenerated electrons and holes. Then photoexcited high energy electrons and holes further react with the surrounding water moisture and oxygen molecules, creating reactive intermediate species •OH (*20*). These reactive intermediate species then can react with the vicinity organics and finally degrade them (*21*). Photocatalytic tailoring is a solution- and chemical- free process because it does not introduce any photoresist or other chemical reagents. So it becomes a high promising technique for graphene electronics because any chemical contamination would degrade the device performance. TiO_2-based photocatalytic, which likes chemical scissors, can be employed to cut the stable sp^2 carbon network of graphene (*17*). This method is a clean and dry photocatalytic process

enabling a versatile tailoring of graphene. Therefore it is significant to develop a simple method of creating permanently nanopatterned graphene based on such an improved technique.

Here we report a simple approach to pattern graphene suspended on top of nanopillar arrays via selective-area photocatalysis without using any plasma or chemical agents. In our approach we use a fully scalable block copolymer lithography process for the preparation of the nanopillar array (*22, 23*), which allows for the fabrication of graphene nanomesh with significantly smaller pitch than state-of-the-art (*17*). Graphene patterning can be controlled with great accuracy by using uniform and periodic nano-templates fabricated by block copolymer lithography. In addition, the photocatalytic process can be easily adapted to large scale production, which is a very appealing feature of the proposed method. A schematic of the fabrication process of graphene nanomesh based on patterned graphene photocatalysis is illustrated in Figure 3.1. First the periodically patterned substrate (silicon oxycarbide nanopillars) was fabricated employing a recently developed block copolymer nanolithography process (*22, 23*): polystyrene-*b*-polydimethylsiloxanes (SD) was directly spin-cast on SiO_2/Si substrate without any brush layer. Similar to our previous reports, selective solvent vapor annealing (SVA) was conducted to generate well-ordered hexagonal cylinder with perpendicular orientation without film defects over large area. The following O_2 dry etching enables simultaneous formation of the silicon oxycarbide nanopillars and removal of the PS block. A thin layer of TiO_2 (~4 nm) was conformably deposited onto these silicon oxycarbide nanopillars by ALD. The obtained samples were then thermally annealed in air at 500℃ for 2 hours in order to induce crystallization of TiO_2 in the photocatalytically active anatase phase (*24*). The CVD graphene was transferred onto such a patterned substrate. Then, the graphene sample was irradiated with ultraviolet light of wavelength 315-400 nm and power density of 5 mW/cm^2 in the presence of oxygen at room temperature. Poly (methyl methacrylate) (PMMA) thin film was used as the transfer medium, and subsequently removed by acetone. The photocatalytic mechanism can

be found elsewhere (*14, 19, 21*). Briefly, electron-hole pairs are created by the UV photons on TiO_2, which then generate highly reactive •OH free radicals in reaction with the air oxygen and water molecules. The •OH free radicals oxidize and ultimately break the graphene skeleton covalent bonds. Finally, the graphene superlattice was transferred onto a flat target substrate after dissolving the TiO_2-covered nanopillars in HF solution.

In this way, graphene nanopatterning is defined by the prepatterned substrates. We have successfully fabricated graphene nanomesh and graphene nanoribbons with different periodicities by varying the morphology and length scale of the photocatalytic substrate.

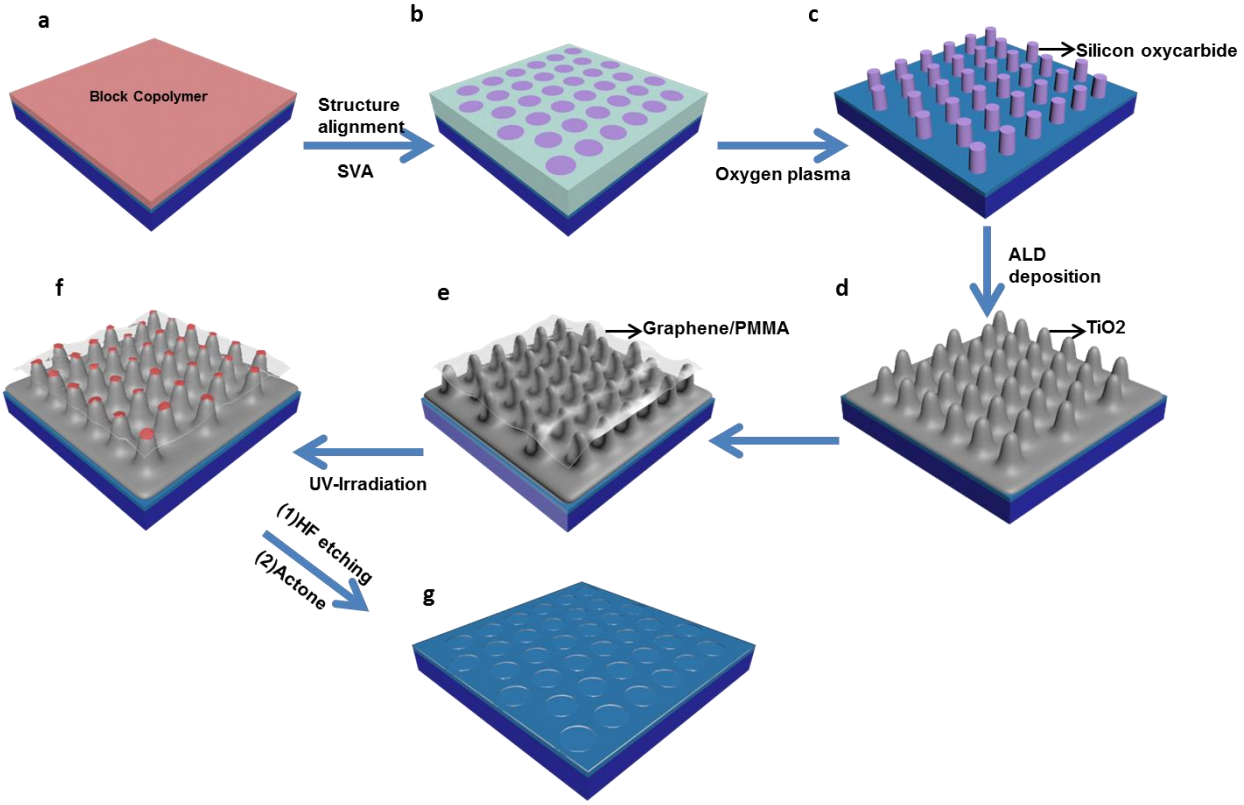

Figure 3.1 Schematic illustration of the process for selective-area photocatalytic graphene patterning. (a) Spin coating of block copolymer thin film directly on SiO_2/Si substrate. (b) Structure alignment via solvent vapor annealing (SVA) of block copolymer. (c) Fabrication of hard silicon oxycarbide nanopillars through oxidation of PDMS and simultaneous removal of PS under oxygen plasma. (d) Atomic layer deposition of TiO_2 thin film on top of the silicon oxycarbide nanopillars.

(e) Transferring PMMA-supported single-layer graphene onto the TiO_2-covered nanopillars. (f) Photocatalytic creation of graphene nanomesh via UV irradiation at ambient conditions. (g) Graphene nanomesh transferred on SiO_2/Si substrate after HF wet etching of the nanopillars and, removal of PMMA by acetone.

3.2 Methods to nanopatterned graphene

Sample Preparation

Silicon substrates were received within clean room environment and 90 nm SiO_2 were grown by using "Boron Drive-in + Pre-dep Furnace" after standard RCA cleaning. Polystyrene-b-polydimethylsiloxanes (SD39) (27K-b-12K) was synthesized by living anionic polymerization following already reported procedure (*25*). It was dissolved in cyclohexane at a concentration of 0.25 wt. % and was spin-cast directly onto the substrate at 2000 rpm for 30 seconds to give a 15 nm thin film. Monolayer cylinder morphology formed after appropriate solvent annealing of the SD39 film following the procedure reported in our lab (*22*). The pattern is directly formed on the substrate during solvent annealing at room temperature without any preliminary surface treatment of the substrate. The self-assembled BCPs are transformed into hard lithography masks by oxidation of PDMS under oxygen plasma. The dry etch process was performed in an Advanced Silicon Etcher (ASE, STS MESC Multiplex ICP serial no. 30343). The etch rate of the PS was estimated to be 3 nm/s as measured by ellipsometry.

Preparation of TiO_2-covered Nanopillars

A TiO_2 layer of 4 nm was deposited onto silicon oxycarbide nanopillars using atomic layer deposition (ALD) with 120 cycles at 200℃, which was followed by thermal annealing in air at 500℃ at 500℃ for 2 hours in order to induce crystallization of TiO_2 in the photocatalytically active anatase phase (*24*). The ALD was conducted in Picosun ALD model R200, using alternating exposures to titanium tetrachloride (97%, Aldrich) and deionized water at 200℃ for 100 cycles with

a N_2 gas purge step in between. The exposure and purge times for both precursors used in this study were 1 and 20 seconds, respectively.

Producing Graphene Nanomesh by TiO_2 Nanopillars Photocatalysts

CVD-graphene/PMMA was purchased from ACS Material, with graphene already transferred on polymer substrate. It is predominantly single-layer graphene and the sheet resistance is <600Ω/sq. We transferred CVD-graphene/PMMA onto TiO_2-covered nanopillars and then the structure was illuminated at controlled times by a Ultra-Violet Lamp with 5 mW/cm^2 intensity and a band in the range from 350-400 nm. The photocatalytic reaction of graphene was performed in air at room temperature. After site-selective photocatalytic modification, the samples were immersed in a 40% HF aqueous solution at room temperature using PMMA film as the transfer medium. After detaching the graphene from TiO_2-covered nanopillars, we left the PMMA-supported graphene floating in HF solution for 20 min before transferring it to flat SiO_2/Si substrates in order to allow for complete removal of possible residual TiO_2. The PMMA film was finally removed by acetone.

Material Characterization

Film thicknesses were determined using a VASE Ellipsometer (J. A. Woollam) at three different incidence angles (55^o, 60^o and 65^o). Scanning electron microscopy (SEM) images were taken using a Field Emission Zeiss Ultra Plus scanning electron microscope with a Gemini column operating at an accelerating voltage of 2 kV. All samples were imaged directly without coating or other treatment. Atomic Force Microscopy (AFM) images were taken by an AFM Dimension Icon-PT from Bruker AXS in Peak force QNM (adhesion, modulus, deformation and dissipation) mode. A Thermo DXR-Raman system with a laser wavelength of 455 nm was used for the characterization of graphene samples. The resolution is 5.9-8.5 cm^{-1}, the spot size is 0.5μm, collect exposure time is 10 s per scan, and 5 scans are accumulated to evaluate the tailoring results. The XPS measurements were performed in a XPS-ThermoScientific instrument using Al K-Alpha monochromated radiation

at 1486.7 eV at base pressure between $5*10^{-9}$ and $1*10^{-8}$ Torr. The survey spectra were recorded using 270 watts of X-ray power, 80 pass energy, 0.5 eV step size. The spectra are shown without energy-scale correction and the peak fits consist of Lorentzian and Gaussian distributions.

3.3 Result & discussion

The surface topography of the graphene sheet was characterized by AFM. Surface morphology of the vertically aligned TiO_2-covered nanopillars is presented in Figure 3.2b. It is seen that TiO_2 thin film was deposited uniformly on the silicon oxycarbide nanopillars. Compared to the silicon oxycarbide nanopillars array with a period of 34 nm and pillar diameter of 29 nm (Figure 3. 2a), the period of TiO_2-covered nanopillars remains unchanged and the diameter increases to about 32 nm (Figure 3.2b). Figure 3.2c shows the AFM image of the monolayer CVD graphene on the TiO_2-covered nanopillars. It is clear that the presence of graphene film blurs the AFM image of the pillar contours. Photocatalytic reaction was then simply performed on the graphene sheet under Xe-lamp irradiation. Due to the direct contact between nanopillars and graphene, active •OH species generated on TiO_2 locally react with carbon atoms in contact with TiO_2, breaking the sp^2 carbon bond network. Graphene cutting most likely begins from the center of each nanopillar and then extends to the edge as the irradiation time increases. Figure 3.2d shows the AFM image of the sample after 12 hours of UV-irradiation. We found that the AFM image becomes sharper compared to the image of Figure 3.2c; strongly indicating that photocatalytic reaction has been proceeding.

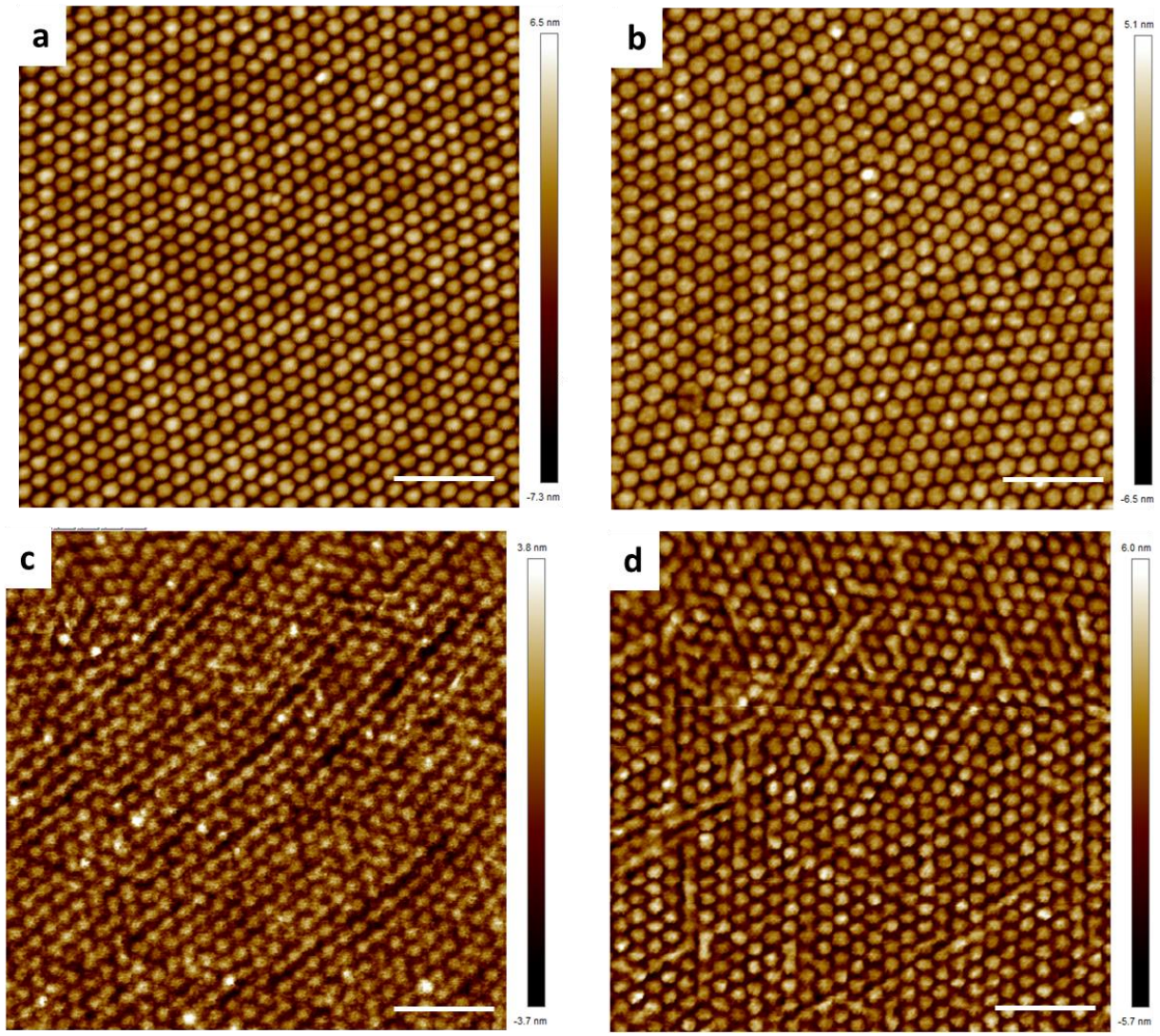

Figure 3.2 Graphene nanomesh formation on TiO_2-covered nanopillars (steps c to f in Figure 3.1). AFM images of (a) Silicon oxycarbide nanopillars. (b) TiO_2-covered nanopillars. (c) Graphene sheet transferred on TiO_2-covered nanopillars and (d) Graphene sheet after 12 h of UV-irradiation. Scale bars: 200 nm.

Scanning electron microscopy (SEM) images confirmed the periodic pattern structure of TiO_2-covered nanopillars and graphene sheet on the TiO_2-covered nanopillars (Figure 3.3). However, in this case, there is no clear distinction between the images of graphene before (Figure 3.3c) and after (Figure 3.3d) UV irradiation.

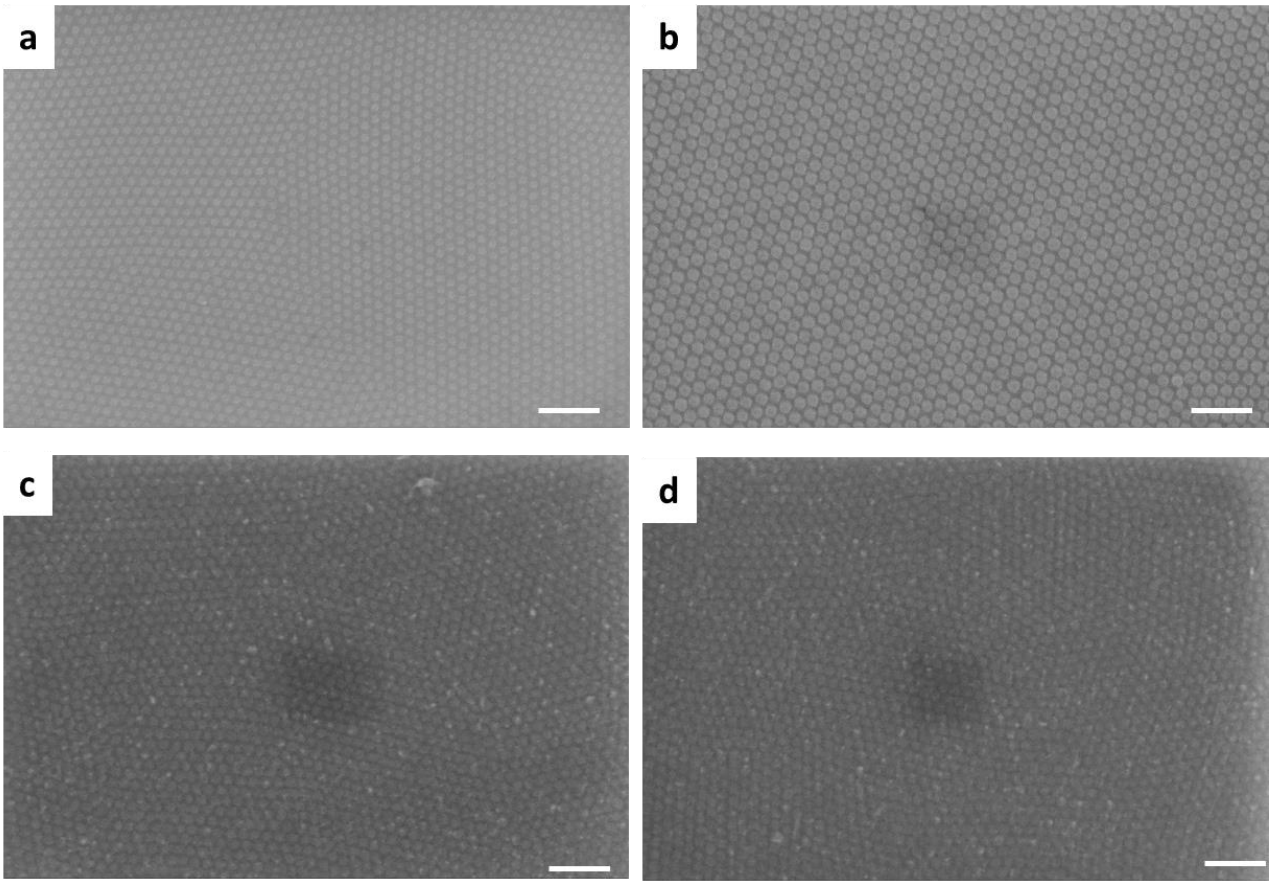

Figure 3.3 Graphene nanomesh formations on TiO_2-covered nanopillars assembly. SEM images of (a) Silicon oxycarbide nanopillars. (b) TiO_2-covered nanopillars. (c) Graphene sheet on TiO_2-covered nanopillars and (d) Graphene sheet on TiO_2-covered nanopillars after 12 h of UV-irradiation. Scale bars: 200 nm.

In addition, the necessary presence of TiO_2 for a successful nanopatterning of graphene has been proved by a control experiment in which CVD single-layer graphene was transferred directly on silicon oxycarbide nanopillars, without TiO_2 coverage, as shown in Figure 3.4a. After 12 h of irradiation by UV-light, we found that the Raman spectrum of graphene remained unchanged (Figure 3.4b); there was no defect (D) peak generated (see the discussion of Raman spectroscopy after Figure 3.5). This result confirms the crucial role of TiO_2 for the photoreaction.

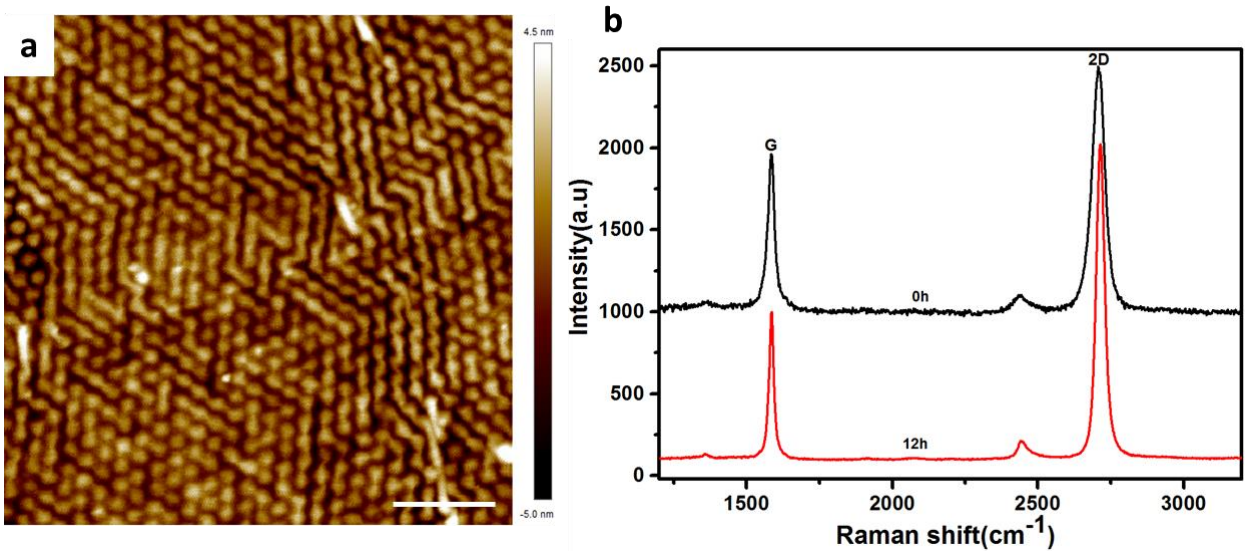

Figure 3.4 (a) AFM image of a graphene sheet on Silicon oxycarbide nanopillars. (b) Raman spectra of pristine graphene and graphene sheet on Silicon oxycarbide nanopillars after 12 h of UV-irradiation. Scale bar: 200 nm.

Figure 3.5 exhibits the typical SEM and AFM image of the patterned graphene after transfer onto a flat SiO_2/Si substrate. As is clearly seen, graphene nanomesh is successfully fabricated after UV-irradiation, indicating formation porous sheets after the photocatalytic process. The period of nanomesh graphene was 34 nm, which is the same as the period of the nanotemplate (Figure 3. 2). This is strong evidence that the selective-area graphene nanopatterning is defined by the underlying nano-template. Graphene superlattice with the 14 nm neck width (Figure 3.5a, b) was formed after 12 h reaction.

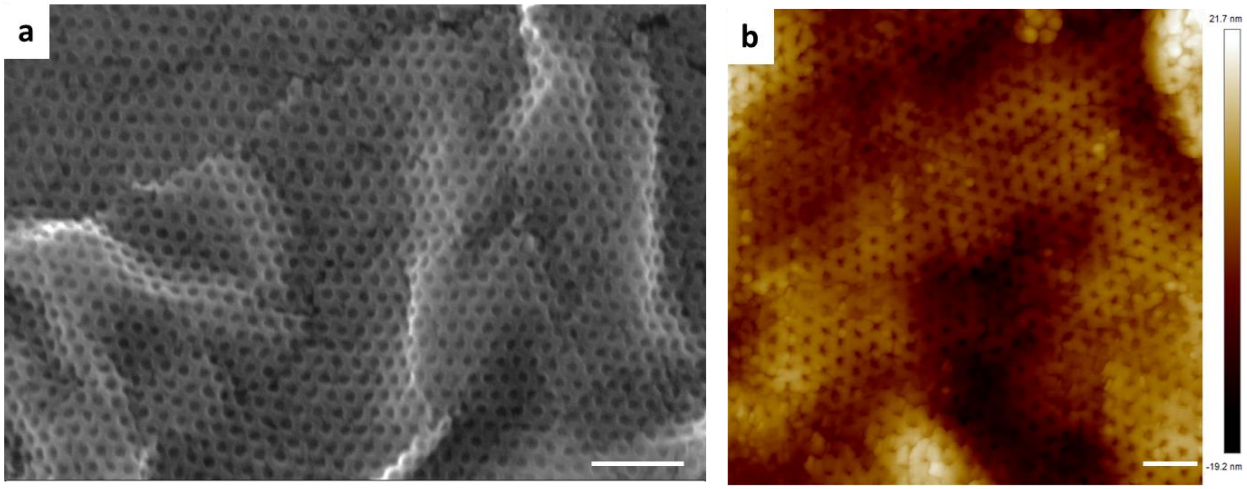

Figure 3.5 Graphene nanomesh transferred onto SiO_2/Si substrate after 12 h of UV-irradiation (step g in Figure 3.1). Scale bars: 200 nm (a), 100 nm (b).

However because of the delicate nature of the monolayer patterned graphene nanomesh, it is difficult and challenging to transfer defect-free graphene nanomesh film to other substrate. As a result, breakage and rupture in the film were introduced during the transfer process. Figure 3.6 shows the large-scale nanomesh graphene transferred onto a silicon substrate. The many folds evident from the image are due to the transfer process. Moreover XPS data show that there is no titanium element left after transferring graphene onto SiO_2/Si substrate (Figure 3.7).

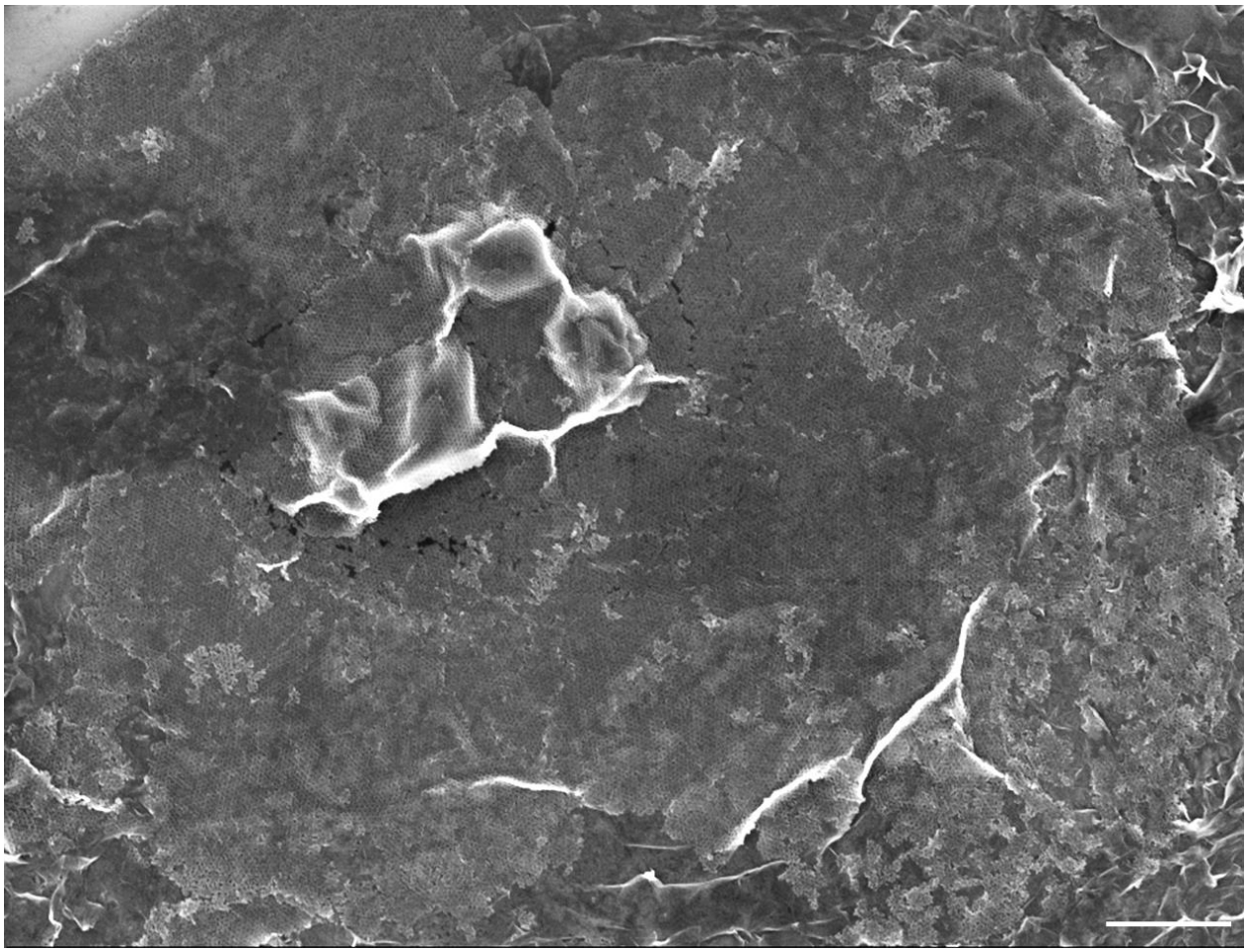

Figure 3.6 SEM image of nanomesh graphene on SiO_2/Si. Scale bar: 1 µm. The entire graphene sheet was transformed into a nanomesh.

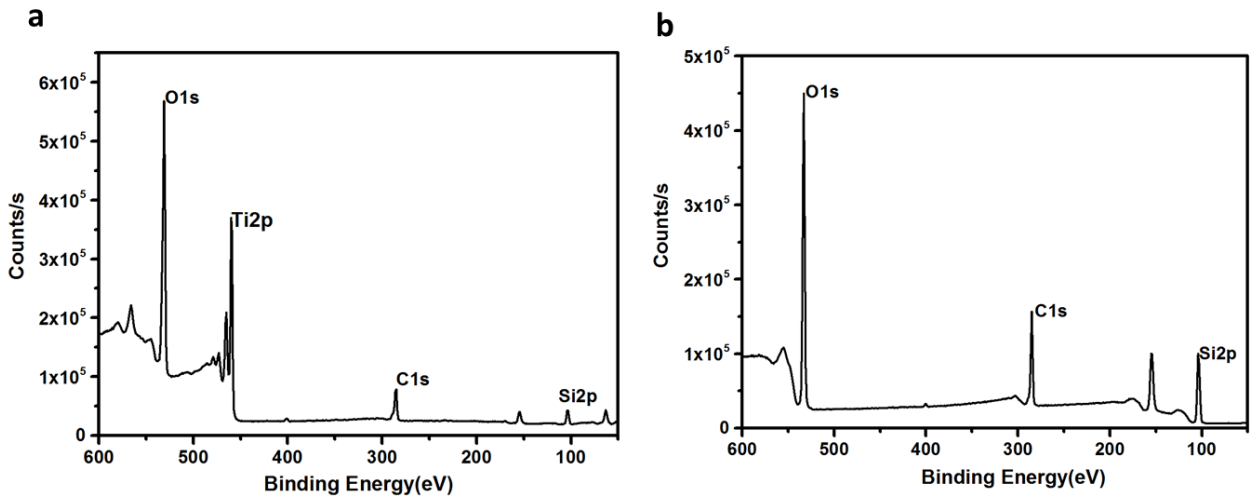

Figure 3.7 XPS spectra of nanomesh graphene (a) on the TiO_2-covered nanopillars, (b) on SiO_2/Si substrate.

As a powerful tool for characterizing ordered/disordered crystal structures of carbonaceous materials, Raman spectroscopy was utilized to examine the defects generated during photocatalysis. Figure 3.8a shows the Raman spectra of graphene transferred from TiO_2-covered nanopillars without UV-irradiation (black curve), 12 h (red) and 14 h of UV-irradiation (blue), revealing the evolution of defect formation. For the pristine CVD graphene used in this study, only a very small Raman D peak is observed, indicative of its high quality. After the photoreaction in the presence of TiO_2, a prominent disorder-induced D peak appears at 1358 cm^{-1}. In addition, the double-resonance 2D peak is weakened. These observations suggest the presence of a larger number of defects, which originate from active species •OH oxidizing the carbon atoms under UV illumination (*19, 21*). It is argued that highly reactive •OH radicals work as photoscissors for the graphenic carbon network (*17, 26*). Also, the intensity ratio between Raman D and G peaks I(D)/I(G) (commonly used to characterize disorder in graphene), is observed to increase with the time of UV-irradiation. As the irradiation time increases, we observed a significant increase of I(D)/I(G) ratio from 0.03 for 0 h to 0.73 for 12 h, and 0.94 for 14 h as shown in Figure 3.8b. Moreover, disorder should lead to a

decrease of the I(2D)/I(G) as shown in Figure 3.8b (*27*). In general, full width half maximum of the 2D peak (FWHM (2D)) remains constant for changes in doping level and increase only with disorder (*27*). Here we can see FWHM (2D) changing slightly and then noticeably increase after 12 h of UV-irradiation, revealing high defect density at 14 h irradiation (Figure 3.8c) (*28*).

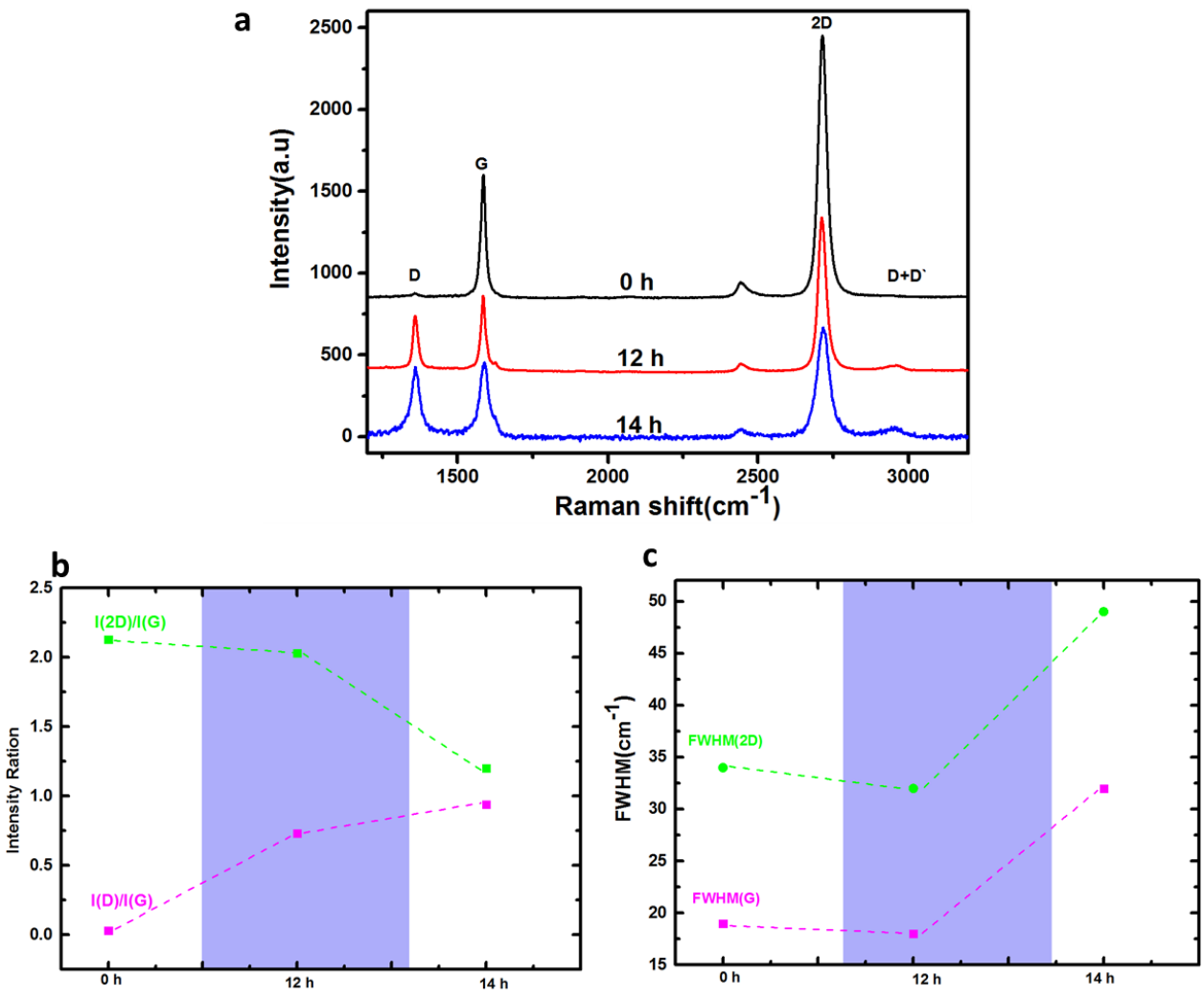

Figure 3.8 Characterization by Raman spectroscopy of pristine graphene and graphene nanomesh formed after 12 h and 14 h of UV-irradiation transferred onto SiO_2/Si substrate. (a) Raman spectra. (b) Evolution of the peak intensity ratios I(D)/I(G) (magenta) and I(2D)/I(G) (green) during the fabrication of nanomesh graphene. (c) Evolution of FWHM (G) (magenta) signal together with FWHM (2D) (green) during the fabrication of nanomesh graphene.

In order to quantify the amount of defects introduced in the photocatalytic process, we analyze the obtained Raman spectra accounting for the defect that may be present in the system. The patterning itself could introduce a characteristic crystallite length scale related to the boundaries of the GNM and this is a measure of the average inverse nano-crystallite size 1/La (*29*).For our analysis, we use the Tuinstra–Koenig relation to obtain La.

$$L_a\ (nm) = (2.4 \times 10^{-10})\ \lambda_{laser}^{4} (I_D/I_G)^{-1}. \qquad (3.1)$$

Here La is the average separation between defects, λ is the Raman excitation wavelength (455 nm in our case) and I_D/I_G is the peak intensity ratio. Supposing that the disorder originates from graphene boundaries, Equation (3.1) estimates a nanomesh neck width of 14.1 nm for 12 h UV-irradiation and 10.9 nm for 14 h UV-irradiation. A 14.1 nm neck width almost coincides with that measured from the SEM and AFM images in Figure 3.5a, b. The entire activation of the D band measured in graphene nanomesh would be, thus, fully accounted for by the nanomesh edges. This fact indicates that the main defects in the graphene nanomesh are close to the nanomesh edges. It should be careful that the control of irradiation time is critical to the formation of nanomesh. When the irradiation time is longer than 12 hours, graphene mostly seems damage and cannot be transferred from the TiO_2-covered nanopillars, probably due to uncontrolled diffusion of reactive species (*22, 23, 30*). Graphene nanoribbons with a periodicity of 36 nm (Figure 3.9) have been fabricated in such a way.

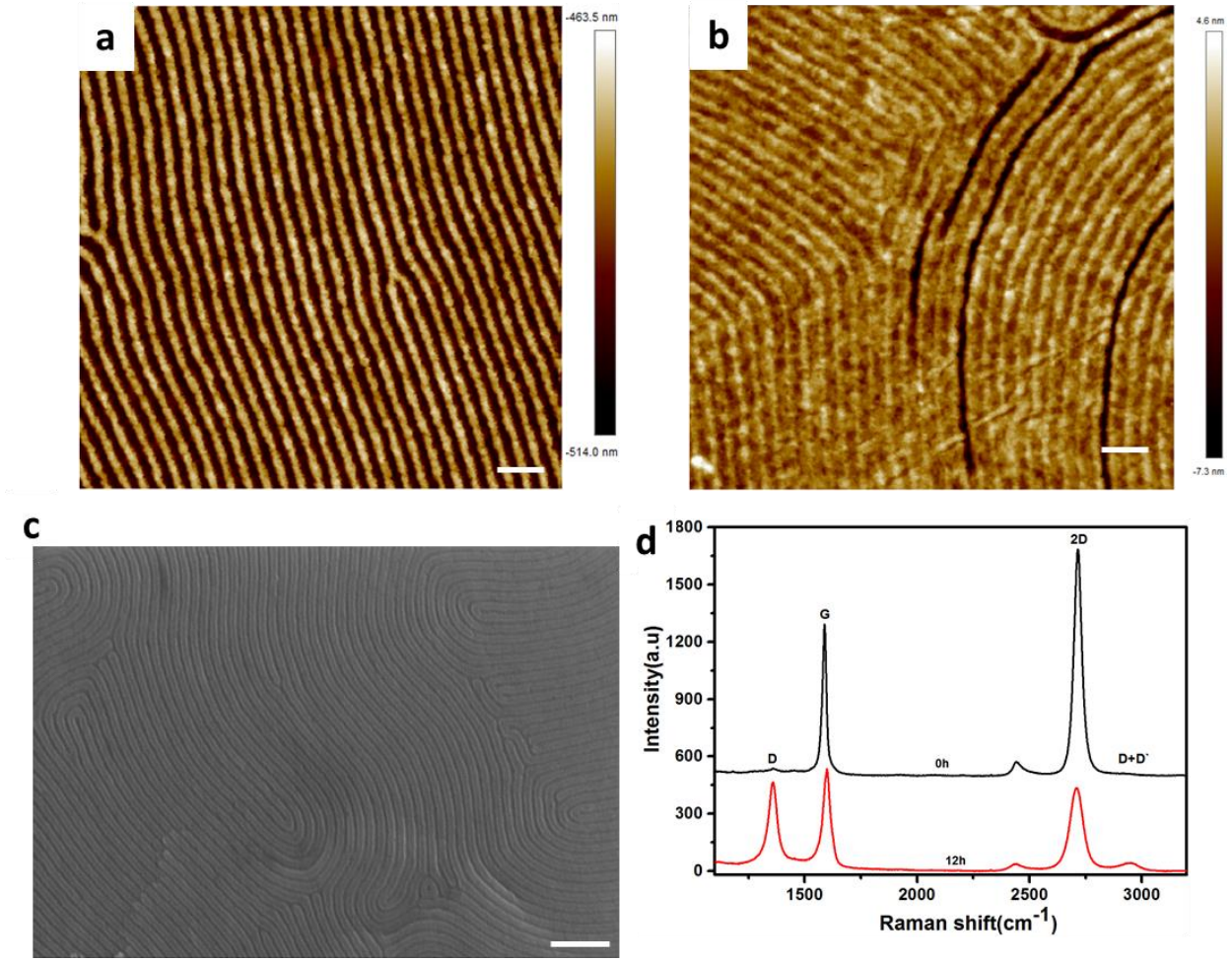

Figure 3.9 AFM images of (a) TiO_2-covered nanoribbons. (b) Graphene sheet on TiO_2-covered nanoribbons after 12 h of UV-irradiation. (c) SEM image of graphene nanoribbons transferred onto SiO_2/Si substrate after 12 h of UV-irradiation and (d) Raman spectroscopy characterization of graphene sheet on TiO_2-covered nanoribbons after 12 h of photo-irradiation. Scale bars: 100 nm (a) and (b), 200 nm (c).

We use the equation (3.1) to estimate the ribbon defect generation. Supposing that the disorder originates from graphene boundaries, Equation (3.1) estimates a ribbon channel (La) of 11.8 nm for 12 h of UV-irradiation, agreeing with the 13 nm width as shown in Figure 3.9c.

3.4 Summary

In summary, uniform graphene nanomeshs and nanoribbons were fabricated using local photocatalysis of graphene sheet by the contact of vertically aligned TiO_2-covered nanopillars and

nanowire arrays. AFM and SEM images illustrated the formation of the graphene nanomesh with the pore size of 24 nm and neck width of 14 nm, the graphene nanoribbions with the ribbon size of 24 nm and neck width of 12 nm. Disorder-quantification by Raman analyses confirmed the experiments results. The presented substrate engineering technique allows for a well-controlled periodic modification of graphene and other UV transparent thin films, enabling in perspective the construction of various graphene-based electronic and photonic devices, biosensors and extending the toolbox for studies of 2D materials superlattices.

3.5 References

1. K. Novoselov, A. Geim, The rise of graphene. *Nat. Mater* **6**, 183 (2007).
2. K. I. Bolotin *et al.*, Ultrahigh electron mobility in suspended graphene. *Solid state communications* **146**, 351 (2008).
3. K. Novoselov *et al.*, Two-dimensional gas of massless Dirac fermions in graphene. *nature* **438**, 197 (2005).
4. I. Meric *et al.*, Current saturation in zero-bandgap, top-gated graphene field-effect transistors. *Nature nanotechnology* **3**, 654 (2008).
5. F. Schwierz, Graphene transistors. *Nature nanotechnology* **5**, 487 (2010).
6. J. Bai, X. Zhong, S. Jiang, Y. Huang, X. Duan, Graphene nanomesh. *Nature nanotechnology* **5**, 190 (2010).
7. M. Y. Han, B. Özyilmaz, Y. Zhang, P. Kim, Energy band-gap engineering of graphene nanoribbons. *Physical review letters* **98**, 206805 (2007).
8. A. Cagliani *et al.*, Large-area nanopatterned graphene for ultrasensitive gas sensing. *Nano Research* **7**, 743 (2014).
9. K. Celebi *et al.*, Ultimate permeation across atomically thin porous graphene. *Science* **344**, 289 (2014).
10. Z. Fang *et al.*, Active tunable absorption enhancement with graphene nanodisk arrays. *Nano letters* **14**, 299 (2013).
11. F. J. Garcia de Abajo, Graphene plasmonics: challenges and opportunities. *Acs Photonics* **1**, 135 (2014).
12. Z. Sun *et al.*, Towards hybrid superlattices in graphene. *Nature communications* **2**, 559 (2011).
13. Z. Li, W. Zhang, Y. Luo, J. Yang, J. G. Hou, How graphene is cut upon oxidation? *Journal of the American Chemical Society* **131**, 6320 (2009).
14. O. Akhavan, Graphene nanomesh by ZnO nanorod photocatalysts. *ACS nano* **4**, 4174 (2010).
15. T.-J. Kuo, C.-N. Lin, C.-L. Kuo, M. H. Huang, Growth of ultralong ZnO nanowires on silicon substrates by vapor transport and their use as recyclable photocatalysts. *Chemistry of Materials* **19**, 5143 (2007).

16. U. I. Gaya, A. H. Abdullah, Heterogeneous photocatalytic degradation of organic contaminants over titanium dioxide: a review of fundamentals, progress and problems. *Journal of Photochemistry and Photobiology C: Photochemistry Reviews* **9**, 1 (2008).
17. L. Zhang *et al.*, Photocatalytic patterning and modification of graphene. *Journal of the American Chemical Society* **133**, 2706 (2011).
18. A. L. Linsebigler, G. Lu, J. T. Yates Jr, Photocatalysis on TiO2 surfaces: principles, mechanisms, and selected results. *Chemical reviews* **95**, 735 (1995).
19. X. Chen, S. S. Mao, Titanium dioxide nanomaterials: synthesis, properties, modifications, and applications. *Chemical reviews* **107**, 2891 (2007).
20. W. Kubo, T. Tatsuma, Detection of H2O2 released from TiO2 photocatalyst to air. *Analytical Sciences* **20**, 591 (2004).
21. A. Fujishima, X. Zhang, D. A. Tryk, TiO 2 photocatalysis and related surface phenomena. *Surface Science Reports* **63**, 515 (2008).
22. T. Li, Z. Wang, L. Schulte, O. Hansen, S. Ndoni, Fast & scalable pattern transfer via block copolymer nanolithography. *RSC Advances* **5**, 102619 (2015).
23. T. Li, Z. Wang, L. Schulte, S. Ndoni, Substrate tolerant direct block copolymer nanolithography. *Nanoscale* **8**, 136 (2016).
24. D.-J. Won, C.-H. Wang, H.-K. Jang, D.-J. Choi, Effects of thermally induced anatase-to-rutile phase transition in MOCVD-grown TiO2 films on structural and optical properties. *Applied Physics A* **73**, 595 (2001).
25. S. Ndoni, P. Jannasch, N. B. Larsen, K. Almdal, Lubricating effect of thin films of styrene-dimethylsiloxane block copolymers. *Langmuir* **15**, 3859 (1999).
26. W. Kubo, T. Tatsuma, Mechanisms of photocatalytic remote oxidation. *Journal of the American Chemical Society* **128**, 16034 (2006).
27. I. Childres, L. A. Jauregui, J. Tian, Y. P. Chen, Effect of oxygen plasma etching on graphene studied using Raman spectroscopy and electronic transport measurements. *New Journal of Physics* **13**, 025008 (2011).
28. L. Cancado *et al.*, General equation for the determination of the crystallite size La of nanographite by Raman spectroscopy. *Applied Physics Letters* **88**, 163106 (2006).
29. A. Jorio, C. A. Achete, E. H. M. Ferreira, L. G. Cançado, R. B. Capaz, *Measuring disorder in graphene with Raman spectroscopy*. (INTECH Open Access Publisher, 2011).
30. S. Rasappa *et al.*, High quality sub-10 nm graphene nanoribbons by on-chip PS-b-PDMS block copolymer lithography. *RSC Advances* **5**, 66711 (2015).

4. Pushing graphene plasmon polaritons to the near-infrared window by block copolymer nanolithography

This chapter was adapted from "Experimental demonstration of graphene plasmons working close to the near-infrared window," Zhongli Wang, Tao Li, Kristoffer Almdal, N. Asger Mortensen, Sanshui Xiao, Sokol Ndoni. Optics Letters. 2016, 41 (22), 5345–5348.

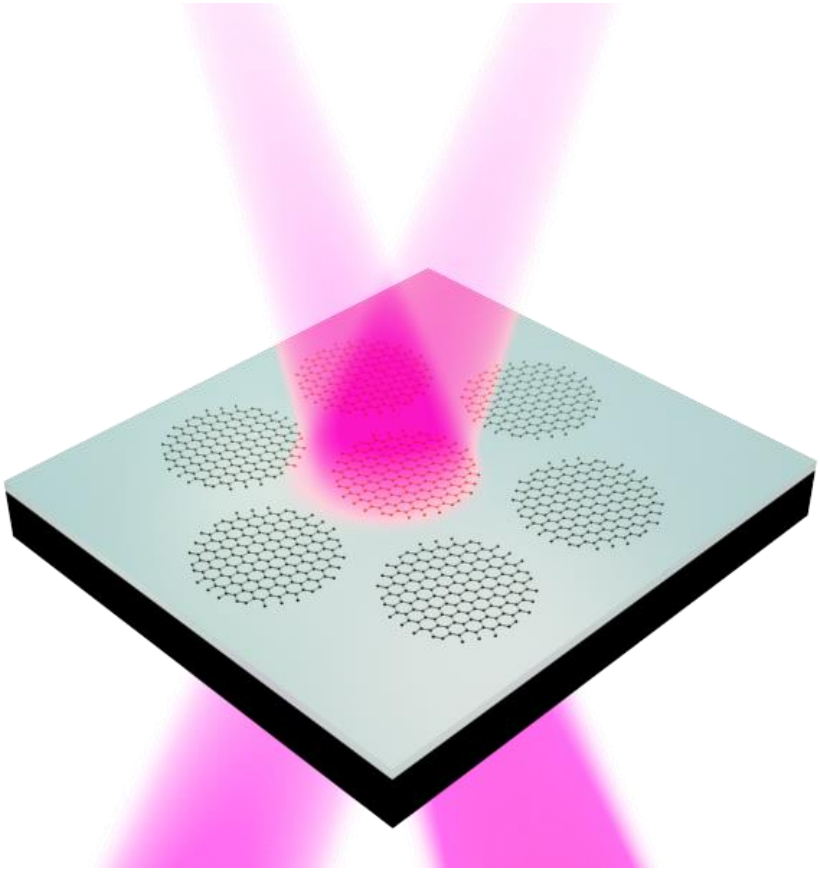

4.1 Introduction

Graphene is proved to be a promising material for optoelectronic devices because of its unique electric and photonic properties (*1*). Relying on its high carrier mobility and tunability, many fascinating graphene-based optoelectronic devices have been realized, including photodetectors (*2-5*), modulators (*6-11*), and ultrafast lasers (*12-14*). However, due to its single-atom-layer thickness, graphene interacts with light very inefficiently (only 2.3% absorption) (*15*), posing challenges and

restrictions for graphene-based optoelectronic devices. Many efforts so far have focused on enhancing light-graphene interactions by integrating graphene with dielectric cavity systems and plasmon resonators made from noble metals (*16-19*). An alternative approach for enhancing optical absorption in graphene is to excite graphene-plasmon polaritons (GPPs) supported by graphene sheets or graphene nanostructures (*20-23*). GPPs are confined to volumes much smaller than the diffraction limit, thus facilitating the optical absorption in the single-layer graphene. A highly doped graphene sheet does support propagation of GPP in the near-infrared window, while it is relatively difficult to excite the propagating GPP (*24-27*). Due to easy control and manipulation of localized plasmons supported by graphene nanostructures, localized GPPs have been widely explored in the mid-infrared and terahertz windows (*28-34*). In graphene nanostructures (with D being the characteristic dimension), the plasmon-resonance wavelength is associated with localized GPPs scales as $\sqrt{E_F/D}$, where E_F is the Fermi level of graphene (*35*). Thus, shorter wavelength can be achieved through both higher doping levels and/or reduced structure dimensions. Until now, the shortest wavelength of the localized GPP was observed around 3.7 μm in a 20 nm wide graphene nano-ring formed by using electron-beam lithography; this value is still quite far away from the wavelength window used in telecommunication (roughly 1.3~1.7 μm). It has been suggested to use bottom-up approaches to control graphene features even with atomic-scale resolution (*36, 37*). In this thesis, we demonstrate the first realization of graphene nanostructures supporting localized GPP below 2 μm by use of a block copolymer self-assembly method combined with oxygen reactive ion etching. We use a fully scalable block copolymer lithography process for preparation of highly uniform and periodic cylinder/sphere templates (*38*), which allow for a good control of size and uniformity of the produced graphene nanostructures

4.2 Graphene nanodisk plasmon observed close to the near-infrared window

Figure 4.1 shows the overall nanodisk arrays process. First the PS-majority BCPs PS-b-PDMS were directly spin-cast on a graphene/SiO_2/Si substrate without any preliminary surface modification (e.g. the ubiquitous surface grafting of a brush layer (*39*). Selective (to the PS domain) solvent vapor annealing (SVA) was then applied to generate well-ordered vertical hexagonal cylinder or monolayer packed sphere morphology over a large area. The following O_2 dry etching enables simultaneous formation of the hard silicon oxycarbide nanocylinder/nanosphere by oxidation of the PDMS block, removal of the PS block and patterning of the underlying graphene. The size of graphene nanodisks can be tuned by carefully adjusting the dry etching time.

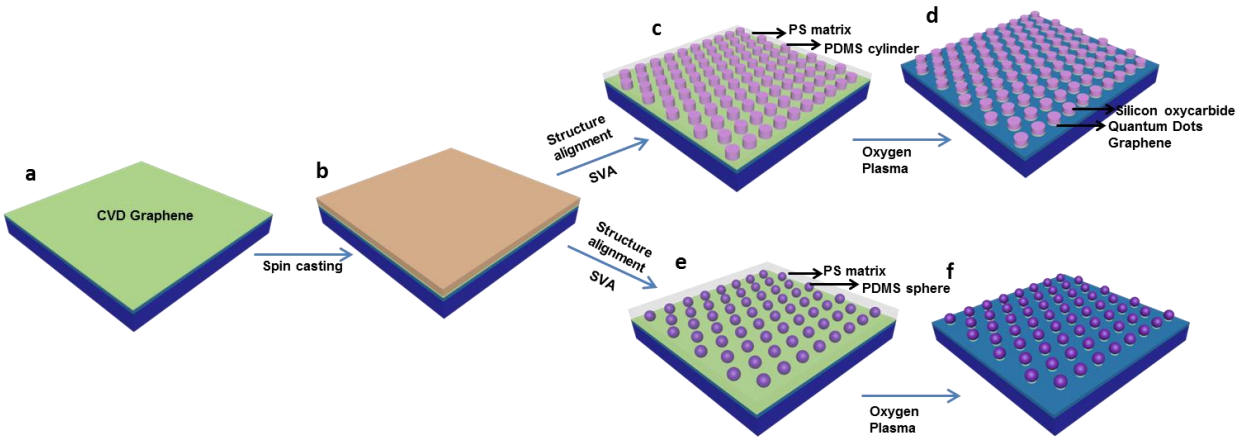

Figure 4.1 Fabrication of graphene-nanodisk arrays (GNDAs) by direct block copolymer nanolithography. (a) CVD graphene on SiO_2/Si substrate. (b) Spin coating of block copolymer thin film directly on CVD graphene. (c, e) Structure alignment of block copolymer via solvent vapor annealing. (d, f) Fabrication of hard silicon oxycarbide nanocylinder/nanosphere array through oxidation of PDMS, simultaneous removal of PS and etching of graphene under oxygen plasma.

Experimental section:

Synthesis: All the solvents are purchased from Sigma Aldrich without further purification (except for the BCP synthesis). Monolayer Graphene on SiO_2/Si (Graphenea) is used as received.

Polystyrene-b-polydimethylsiloxanes SD39 (27k-b-12k) and SD165 (144.5k-b-20.5k) were synthesized by living anionic polymerization following already reported procedure (*40*). SD39 was dissolved in cyclohexane at a concentration of 0.25 wt. % and was spin-cast directly onto the substrate at 2000 rpm for 30 seconds to give a 15 nm thin film. Monolayer cylinder morphology formed after appropriate solvent annealing of the SD39 film following the procedure reported in our lab (*38*). SD165 was dissolved in cyclohexane at a concentration of 0.2 wt. % and was spin-cast directly onto the substrate at 2000 rpm for 30 seconds to give a 13 nm thin film. Monolayer sphere morphology formed after appropriate solvent annealing of the SD165 film (mix solvents vapor of cyclohexene/xylene, 5/1). The patterns are directly formed on the substrate during solvent annealing at room temperature without any preliminary surface treatment of the substrate. The self-assembled BCPs are transformed into hard lithography masks by oxidation of PDMS under oxygen plasma.

Fabrication: Solvent vapor annealing is made at room temperature with the samples in a closed glass jar in the presence of selective annealing solvents. For SD39, the annealing time is 90 min in 1,4-dixoane. For SD165 the annealing condition is 1h in mix solvents vapor of cyclohexene/xylene (5/1). Using solvents that are strongly selective to PDMS effectively prevents dewetting since the mobility of the PS block is limited, resulting in a highly controlled and reproducible process. The dry etch process is performed on an Advanced Silicon Etcher (STS MESC Multiplex ICP serial no. 30343). SF_6 plasma condition for pretreatment: 30 sccm SF_6, 50 mTorr, coil power: 100w and platen power: 0w, 8 seconds. O_2 plasma condition for the pattern transfer: 10 sccm O_2, 10 mTorr, coil power: 100w and platen power: 20w. SF_6 plasma condition for mask removal: 50 sccm SF_6, 20 mTorr, coil power: 200w and platen power: 2w, 20 seconds. The etch rate of the PS was estimated to be 3.5 nm/s as measured by ellipsometry.

Characterization: Scanning electron microscopy (SEM) images are taken by a Field Emission Zeiss Ultra Plus scanning electron microscope with a Gemini column operating at an accelerating

voltage of 2 kV. All the samples are imaged directly without coating or other treatment. Atomic Force Microscopy (AFM) images are taken by an AFM Dimension Icon-PT from Bruker AXS. A Thermo DXR-Raman system with a laser wavelength of 455 nm is used for the characterization of graphene samples. The resolution is 5.9 – 8.5 cm^{-1}, spot size is 0.5 μm, collect exposure time is 10 s per scan, and 8 scans are accumulated for each sample.

Result & Discussion: The scanning-electron microscopy (SEM) and atomic-force microscopy (AFM) images of the nanocylinder array on different substrates are presented in Figure 4.2. Silicon oxycarbide nanocylinders were formed from Si-containing PS-*b*-PDMS block copolymers under oxygen plasma (*41*). A well-ordered hexagonally packed cylinder morphology is clearly observed in Figure 4.2a-b. Graphene sheets were patterned simultaneously during oxygen plasma etching on the Si/SiO_2 substrate. Compared to the silicon oxycarbide nanocylinders directly on Si/SiO_2 substrate, the order of nanocylinders on the graphene substrate is less well-defined (Figure 4.2c, d) due to the graphene grain boundary and folds, see Figure 4.3. The silicon oxycarbide mask can be removed by sonication in ethanol at room temperature, thus leaving a monolayer graphene nanodisk array on the substrates (Figure 4.2e, f). A large-area scanning electron microscopic of the GNDA is shown in Figure 4.4. Graphene nanodisks are occasionally removed under the ultrasonication process; however, the remaining population of nanodisks is more than sufficient for a direct size characterization. We notice that the characterization of the plasmonic properties of GNDAs was made prior to sonication.

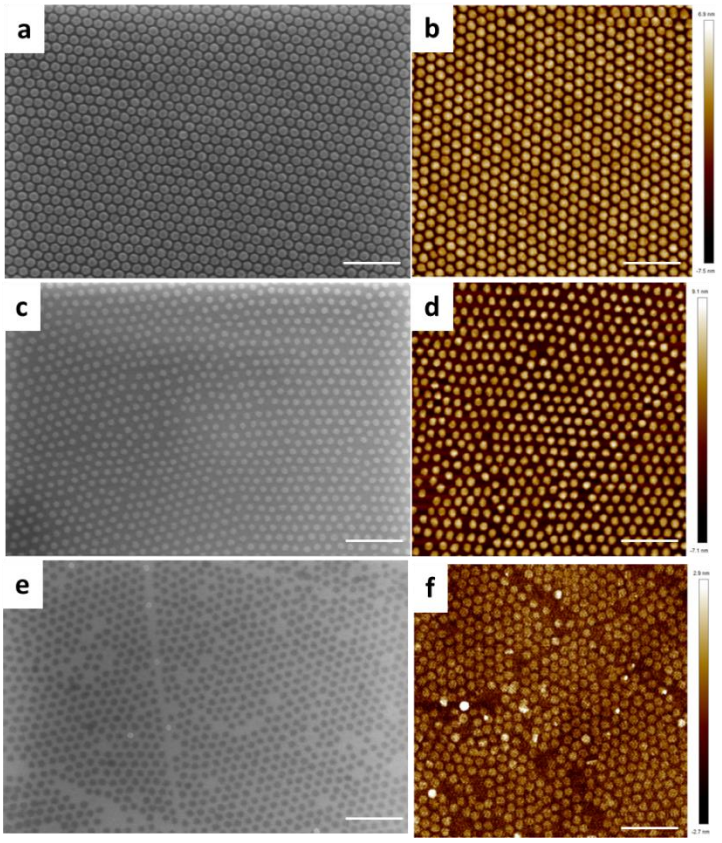

Figure 4.2 SEM (left-column panels) and AFM (right-column panels) images of silicon oxycarbide nanocylinders mask on (a-b) SiO_2/Si substrate, (c-d) on graphene, and (e-f) GNDAs after removal of the mask by sonication. Scale bars: 200 nm.

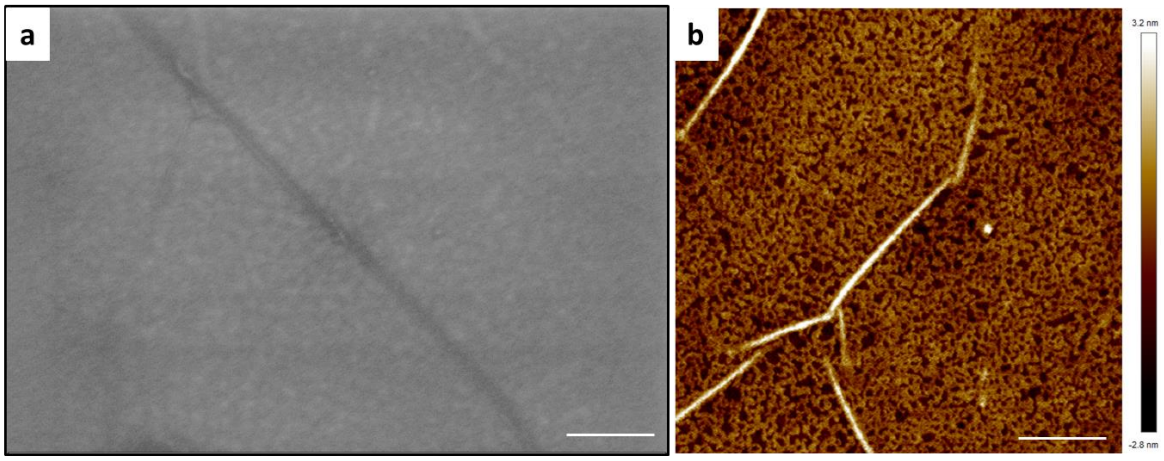

Figure 4.3 SEM and AFM images of pristine monolayer CVD graphene on SiO_2/Si substrate. Scale bar: 200 nm.

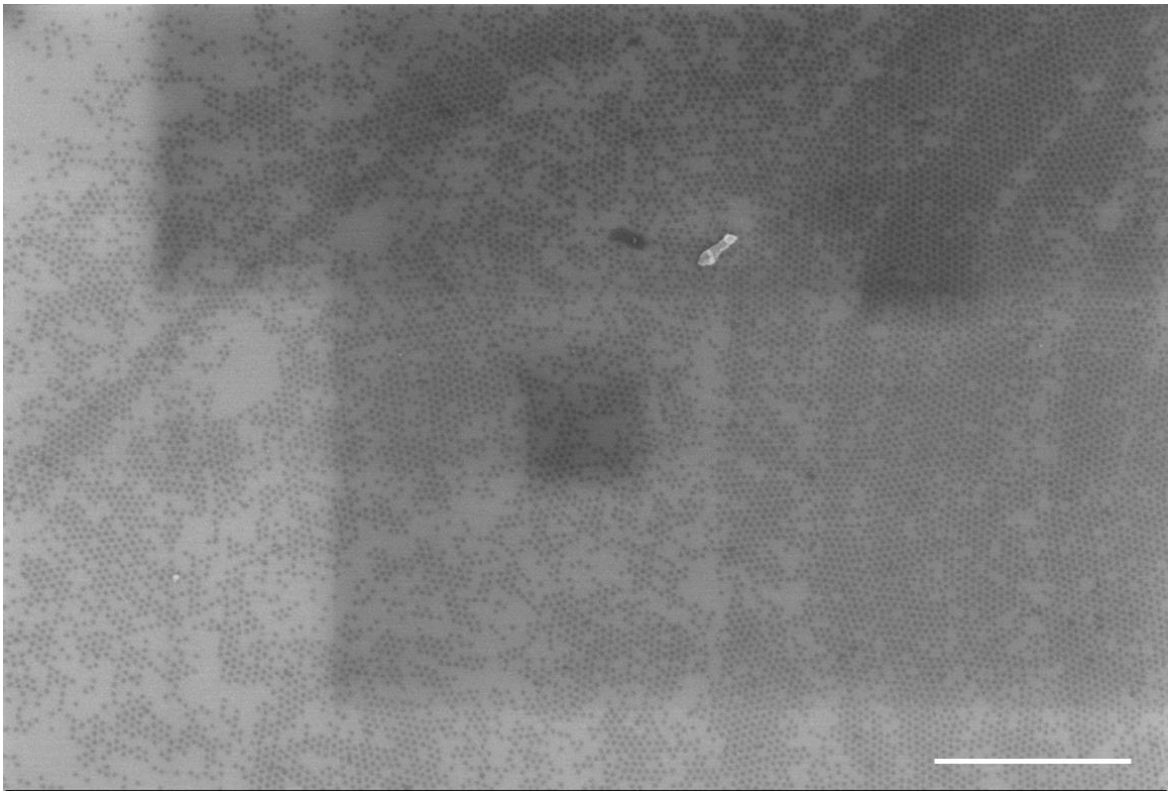

Figure 4.4 SEM image of GNDAs on SiO_2/Si substrate. Scale bar: 1µm.

The diameter of the graphene nanodisks can be controlled by varying the oxygen plasma etching time. For the silicon oxycarbide mask, the diameter remains around 24 nm regardless of the etching time of oxygen plasma (Figure 4.5). In contrast, the diameter of graphene nanodisks can be altered from 25 to 18 nm due to lateral etching when the time for the oxygen plasma changes from 8 s to 10 s, see Figure 4.6. Moreover, AFM images and profiles confirm that a GNDA monolayer is left on the substrate (Figure 4.7).

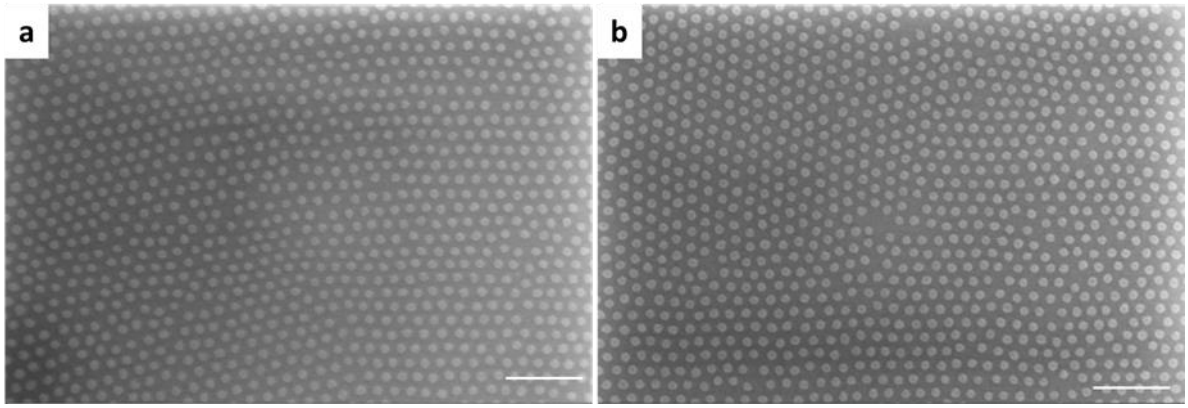

Figure 4.5 SEM images of GNDAs /Silicon oxycarbide nanodots on SiO2/Si substrate after a) 8 s oxygen plasma, and b) 10 s oxygen plasma. Scale bars: 200 nm.

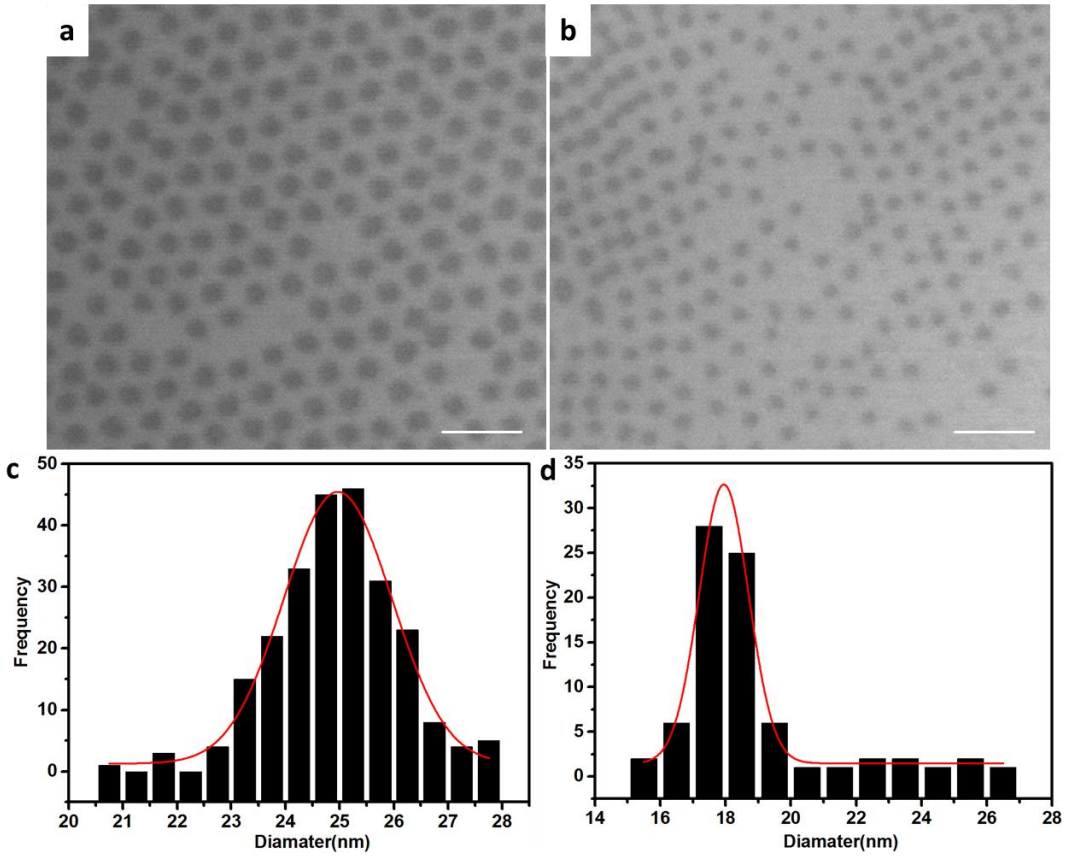

Figure 4.6 SEM images of GNDAs after (a) 8 s and (b) 10 s of oxygen plasma etching. Size distribution of GNDAs after (c) 8 s and (d) 10 s of oxygen plasma etching. Scale bars: 100 nm.

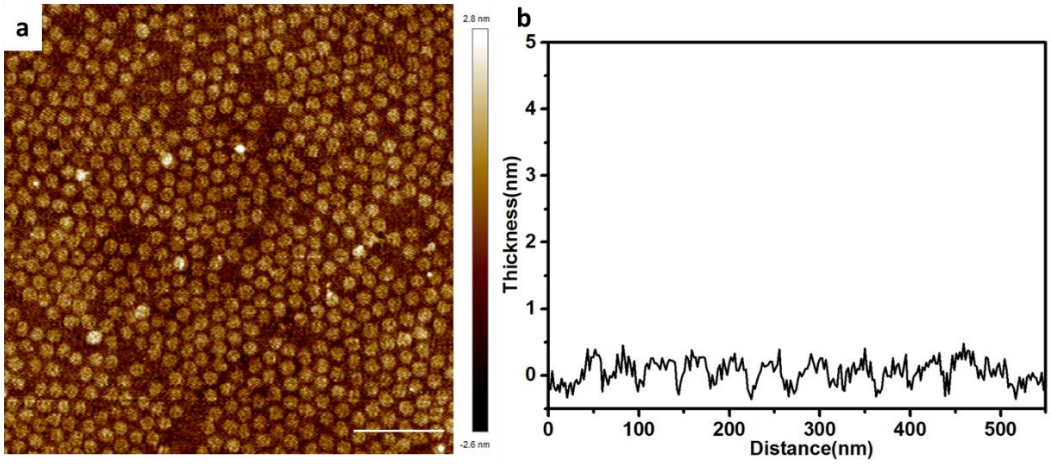

Figure 4.7 GNDAs on SiO_2/Si substrate after 8 s oxygen plasma of a) AFM image, and b) Corresponding line-scan profile. Scale bar: 200 nm.

Raman spectroscopy is a powerful nondestructive technique to explore the properties and structure of graphene samples (*42*). Here, we use Raman spectroscopy to examine the possible defects generated during the oxygen etching process. Figure 4.8a shows the Raman spectra of GNDAs /Silicon oxycarbide nanodots after 0 s (black curve), 8 s (red curve) and 10 s (blue curve) of oxygen plasma, revealing the evolution of defect formation. For the pristine CVD graphene used in this study, only a very small Raman D peak is observed, indicative of the good structural quality of graphene. After the etching in the presence of oxygen plasma, a prominent disorder-induced D peak appears at 1358 cm^{-1}. In addition, the double-resonance 2D peak becomes weaker. These observations suggest the presence of a larger number of defects related to the formation of nanodisk edges. Also, the intensity ratio *I(D)/I(G)* between Raman D and G peaks (commonly used to characterize disorder in graphene), is observed to increase with the time of oxygen plasma. As increasing etching time, we observe a significant increase of the *I(D)/I(G)* ratio, from the initial average of 0.03 for 0 s to 1.48 for 8 s, and 2.00 for 10 s as shown in Figure 4.8a. A higher defect density is also visible in the SEM image of the graphene etched for 10 s (Figure 4.6b) as compared to the sample etched for 8 s (Figure 4.6a). This increase is expected to correlate with the increased

ratio between edge length and disk area as the nanodisks become smaller. At short etching time (below 8 s), Raman spectra appear almost the same as for the pristine graphene, indicative of an unchanged quality. At extended irradiation times, all the Raman peaks characteristic of graphene diminish and broaden.

We examine reflection spectra for the GNDAs using Fourier transform infrared spectroscopy (FTIR, Bruker VERTEX 70) at room temperature with the reflection angle of 20°. To exclude the influence of water vapor surrounding the sample, the system was purged with nitrogen overnight prior to measurement. The centimeter-scale size of the fabricated GNDAs allows us to measure with a relatively large light spot, giving a strong optical response. The unpolarized reflection spectra for the fabricated GNDAs are shown in Figure 4.8b, where the unpolarized reflection for the bare graphene sheet on SiO_2/Si is taken as a reference. Prominent plasmonic resonances appear in the near-IR region for these graphene nanodisk arrays. The excitation of dipole resonances in the graphene nanodisk results in enhanced absorption, thus giving rise to significant dips in the reflection spectra. For nanodisk arrays on silicon substrates, the GPP resonance is observed around 4900 cm^{-1} after 8s treatment with oxygen plasma. As the oxygen plasma etching time increases, we observe a clear 50 nm blueshift from 2.05 μm for 8 s oxygen plasma to 2.00 μm for 10 s oxygen plasma, as shown in Figure 4.8b.

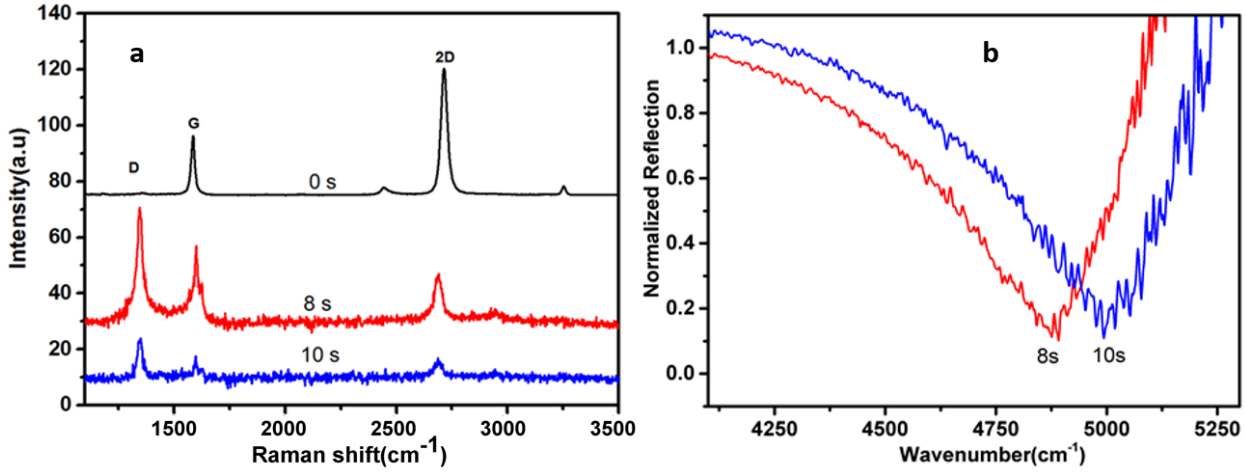

Figure 4.8 (a) Raman spectra and (b) normalized reflection spectra for the GNDAs/Silicon oxycarbide nanodisk formed after 8 s and 10 s of oxygen plasma. As a reference, Raman spectrum before oxygen etching (0 s), see the black line in (a), is shown. The dips in (b) are associated with the excitation of localized GPPs, leading to strong absorption.

Templates such as nanospheres with a lower density have also been fabricated by application of block copolymer lithography (Figure 4.9a, b). Figure 4.9c shows the Raman spectra of GNDAs /Silicon oxycarbide nanospheres after 0 s (black curve), 8 s (red curve) and 9 s (blue curve) of oxygen plasma, revealing the evolution of defect formation associated with the formation of nanodisks by oxygen plasma etching. Similarly, the presence of a larger number of defects is observed clearly as the etching time increases. At the same time, the intensity ratio *I(D)/I(G)* is observed to increase with the duration of oxygen plasma treatment. When increasing etching time, we observe a significant increase of the *I(D)/I(G)* ratio, from the initial average of 0.03 for 0 s to 0.72 for 8 s and 1.51 for 9 s as illustrated in Figure 4.9c. The graphene plasmonic resonance is observed around 5500 cm^{-1} for the case of etching time of 9 s. As the oxygen plasma time increases, we observe an obvious 80 nm blueshift from 1.88 μm for 8 s oxygen plasma to 1.80 μm for 9 s oxygen plasma as shown in Figure 4.9d. The large oscillation arises from the fact that the working wavelength is close to the detection limit of the FTIR instrument. From these nanosphere template experimental observations, we conclude that nanosphere templates are less appropriate masks for oxygen plasma etching to form a nanodisk array due to the isotropic etching, compared to the nanocylinder template. On the other hand, we can get a much smaller size of the graphene nanodisk, thus enabling us to push the plasmonic resonance to a shorter wavelength.

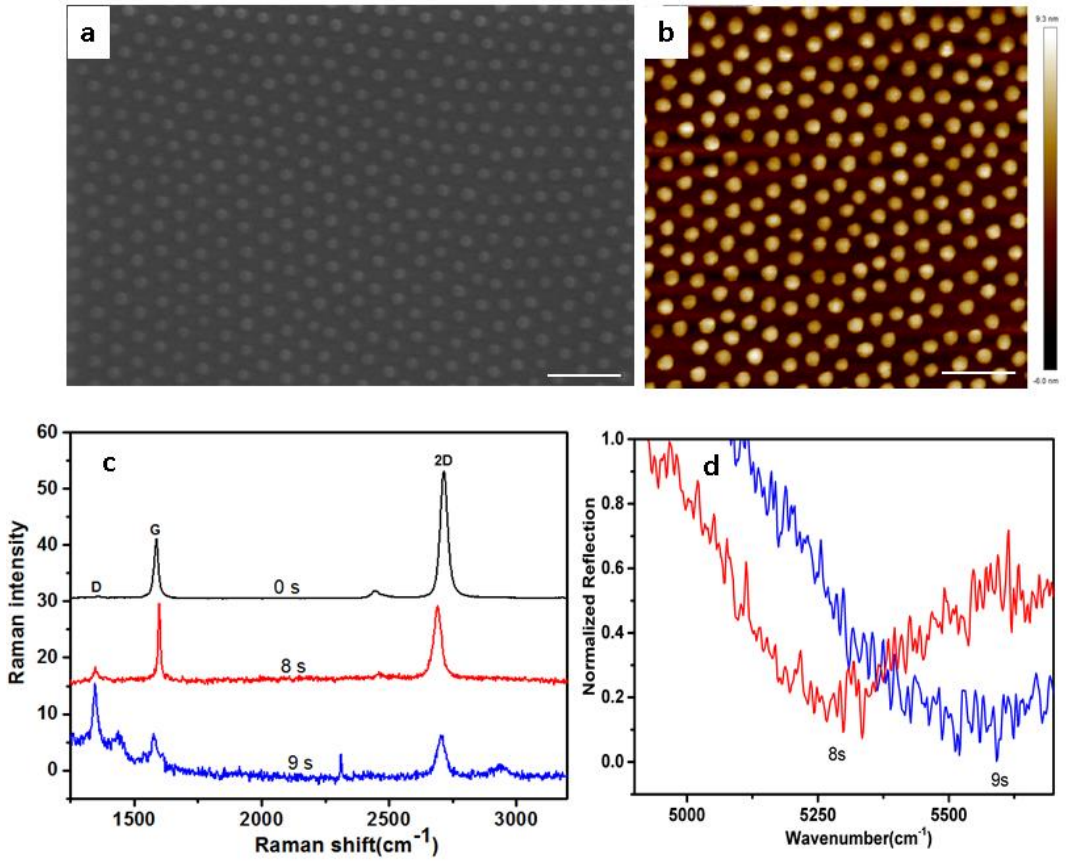

Figure 4.9 (a) SEM, (b) AFM images, (c) Raman spectra and (d) reflection spectra for the GNDAs/Silicon oxycarbide nanospheres after different oxygen plasma etching time on SiO_2/Si substrate. Scale bars: 200 nm.

When the size of graphene structures becomes smaller and smaller, we need to be concerned with atomic-scale details, such as quantum mechanical effects associated with electronic edge states (*43-46*). Ignoring for simplicity such size/quantum effects and coupling effects for the neighboring nanodisks, the GPP dipole-resonance supported by the graphene nanodisk can be classically evaluated as $\lambda = 2\pi c\sqrt{\frac{\pi\hbar^2\varepsilon_0(\varepsilon_1+\varepsilon_2)D}{2e^2E_F}}$, where c is the speed of light in vacuum, $\hbar$ is the reduced Planck constant, ε_1 and ε_2 are the permittivities of cladding and substrate, respectively. For our experiments, ε_1*=1* and ε_2*=2.1.* The CVD-grown graphene is normally hole-doped, and the G mode frequency ω_G in the Raman spectra can be used to estimate the Fermi level in the graphene[48,49] as

$|E_F| = \frac{\omega_G - 1580\ cm^{-1}}{42\ cm^{-1}/eV}$. As indicated in Figure 4.8a, the G mode frequency changes during the treatment by oxygen plasma, e.g. it shifts from 1583 cm^{-1} for the pristine graphene (0 s) to 1600 cm^{-1} after 10 s of plasma treatment, suggesting that the graphene is further hole-doped during the fabrication process. For the case of 10 s, E_F is around -0.48 eV, while we estimate an initial Fermi level of 0.07 eV for 0 s. Equipped with these values of λ and E_F, we obtain D of ~4.6 nm (for the case of 10 s) by use of the classical approach. Alternatively one can estimate effective size of the graphene crystallites by use of the Tuinstra–Koenig relation (*47*). With the value *I(D)/I(G)* of 2.00 for the 10 s case, one finds that the size of the graphene crystallite is about 4.7 nm, which is quite close to the value obtained from the classical theory. However, both estimated sizes are significantly smaller than the apparent physical dimensions (~18 nm) shown in Figure 4.6d. One can conclude that at the longer etching times there are many defects within the nanodisks that cannot be observed by SEM or AFM. In a previous transport experiment with graphene nanoribbon, it was assumed an electrical effective width smaller than the physical width (*48*). Recent work on graphene plasmons in graphene ribbons have made a significant modification of the ribbon width (with a subtraction of 28 nm to the physical value by E-beam) in order to match well with the experimental results (*29*). All these effects (including quantum effects and fabrication impurities) can potentially explain the difference in terms of the size of the graphene nanodisks.

4.3 Graphene nanomesh plasmon observed at the near-infrared window

Principally, increasing the etching time will lead to the reduction of the disk size, and then lead to reaching shorter wavelength. However, it becomes challenging to control the etching time since all graphene will be gone if we choose a relatively longer etching time. By this reason we are working on tuning graphene plasmon resonances at smaller scales in the future using electrical gating methods, where the local concentration of electrons and electric field profile can alter resonances

(*49*). Instead of graphene disks, graphene antidots (i.e. graphene sheets with regular holes) will be chosen because of its easy implementation of "back-gating technique".

Materials: Silicon substrates were received within clean room environment. All the solvents are purchased from Sigma Aldrich without further purification. Polystyrene-b-polydimethylsiloxanes SD81 (26K-b-55K) and SD42 (13K-b-29K) were synthesized by living anionic polymerization following already reported procedure (*40*). CVD graphene was bought from Graphenea.

Fabrication: The dry etch process is performed on an Advanced Silicon Etcher (STS MESC Multiplex ICP serial no. 30343). SF_6 plasma condition to remove PDMS top wetting layer: 40 sccm SF_6, 40 mTorr, coil power: 50w and platen power: 0w, 10 seconds. O_2 plasma condition to remove PS/graphene substrate and oxidize PDMS: 5 sccm O_2, 5 mTorr, coil power: 100w and platen power: 10w. SF_6 plasma condition for breakthrough of the PDMS-substrate wetting layer: 400 sccm SF_6, 10 mTorr, coil power: 200w and platen power: 10w, 5 seconds.

Characterization: Film thickness is determined by a VASE Ellipsometer (J.A. Woollam) at three different incidence angles (55^o, 60^o and 65^o). Scanning electron microscopy (SEM) images are taken by a Field Emission Zeiss Ultra Plus scanning electron microscope with a Gemini column operating at an accelerating voltage of 3 kV. A Thermo DXR-Raman system with a laser wavelength of 455 nm is used for the characterization of graphene samples. The resolution is 5.9 – 8.5 cm^{-1}, spot size is 0.5 μm, collect exposure time is 10 s per scan, and 8 scans are accumulated for each sample. Fourier transform infrared spectroscopy (FTIR, Bruker VERTEX 70) at room temperature with the reflection angle of 20^0.

Results and Discussion: The overall nano-patterning process on graphene substrate by SD42/SD81 is conducted by RIE, which is summarized in Figure 4.10.

First, the polystyrene-*b*-polydimethylsiloxanes (PS-b-PDMS) were directly spin-cast on a graphene/SiO_2/Si substrate without any preliminary surface modification. Selective (to the PDMS domain) solvent vapor annealing (SVA) was then applied to generate well-ordered vertical hexagonal cylinder morphology over a large area. The following O_2 dry etching enables simultaneous formation of the hard silicon oxycarbide nanomesh by oxidation of the PDMS block, removal of the PS block and patterning of the underlying graphene. The size of graphene nanomesh can be tuned by carefully adjusting the dry etching time.

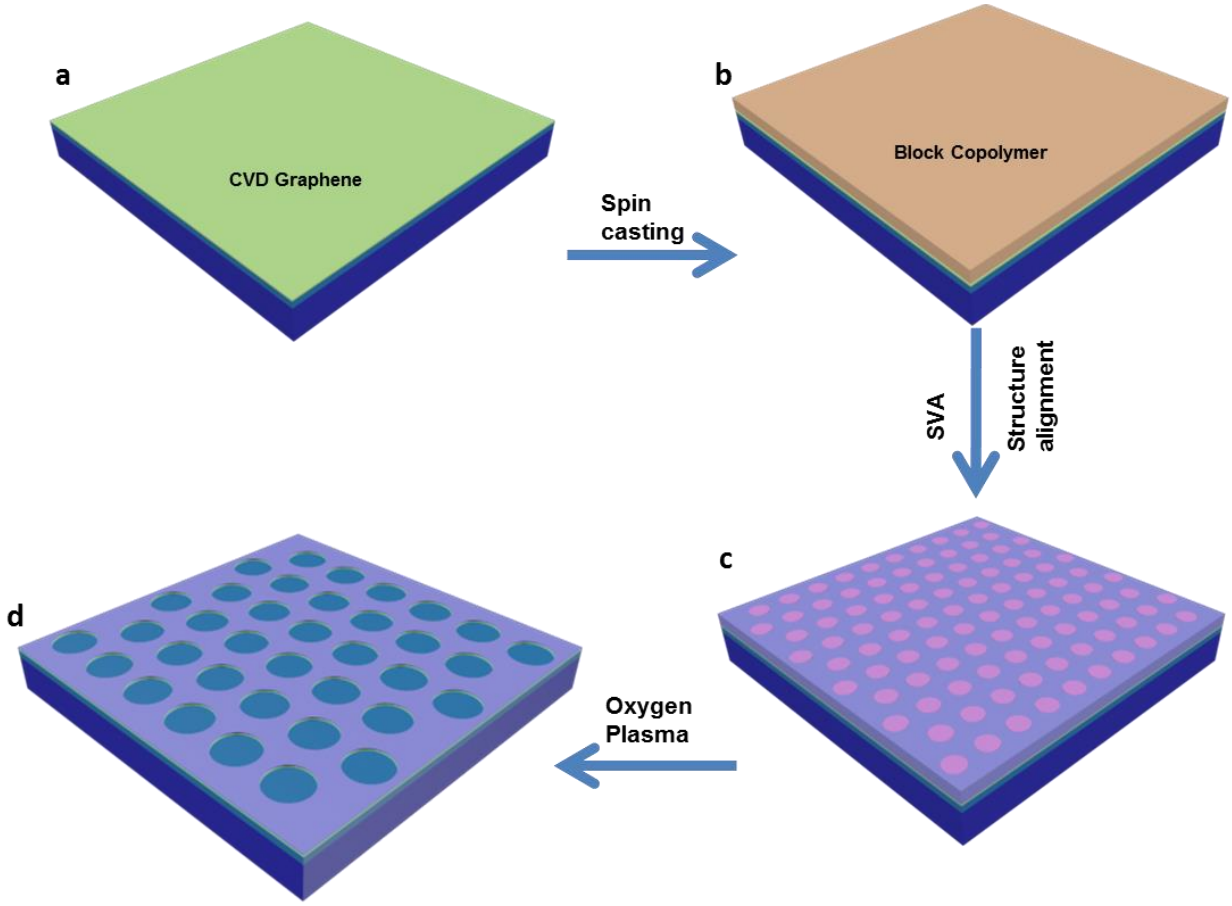

Figure 4.10 Fabrication of graphene-nanomesh (GNM) by direct block copolymer nanolithography. (a) CVD graphene on SiO_2/Si substrate. (b) Spin coating of block copolymer thin film directly on CVD graphene. (c) Structure alignment of block copolymer via solvent vapor annealing. (d)

Fabrication of hard silicon oxycarbide nanomesh through oxidation of PDMS, simultaneous removal of PS and etching of graphene under oxygen plasma.

Figure 4.11(a), (b) and (c) shows the SEM images of SD42 directly deposited on CVD-grown single layer graphene. A large area mask covers the graphene without defects after solvent annealing (Figure 4.11a). The pattern is well adjusted on graphene grain boundaries, multi-layer islands and other substrate defects. The contrast became clear after 8s oxygen plasma etching and the size of period didn't change (Figure 4.11b). However after 10s oxygen plasma etching, the mask was destroyed in certain degree (Figure 4.11c). As a powerful tool for characterizing ordered/disordered crystal structures of carbonaceous materials, Raman spectroscopy was utilized to examine the defect changes that occurred during plasma etching process. Figure 4.11(d) shows the Raman spectra of graphene under SD42 polymer without oxygen plasma treatment (black curve), 8s oxygen plasma treatment (red) and 10 s oxygen plasma treatment (blue), revealing the evolution of defects formation. For the pristine CVD graphene used in this study, only very small Raman D peak is observed, indicative of its high quality. After the oxygen plasma etching, a prominent disorder-induced D peak appears at 1358 cm^{-1}. In addition, the double-resonance 2D peak is weakened. These observations suggest the presence of a larger number of defects.

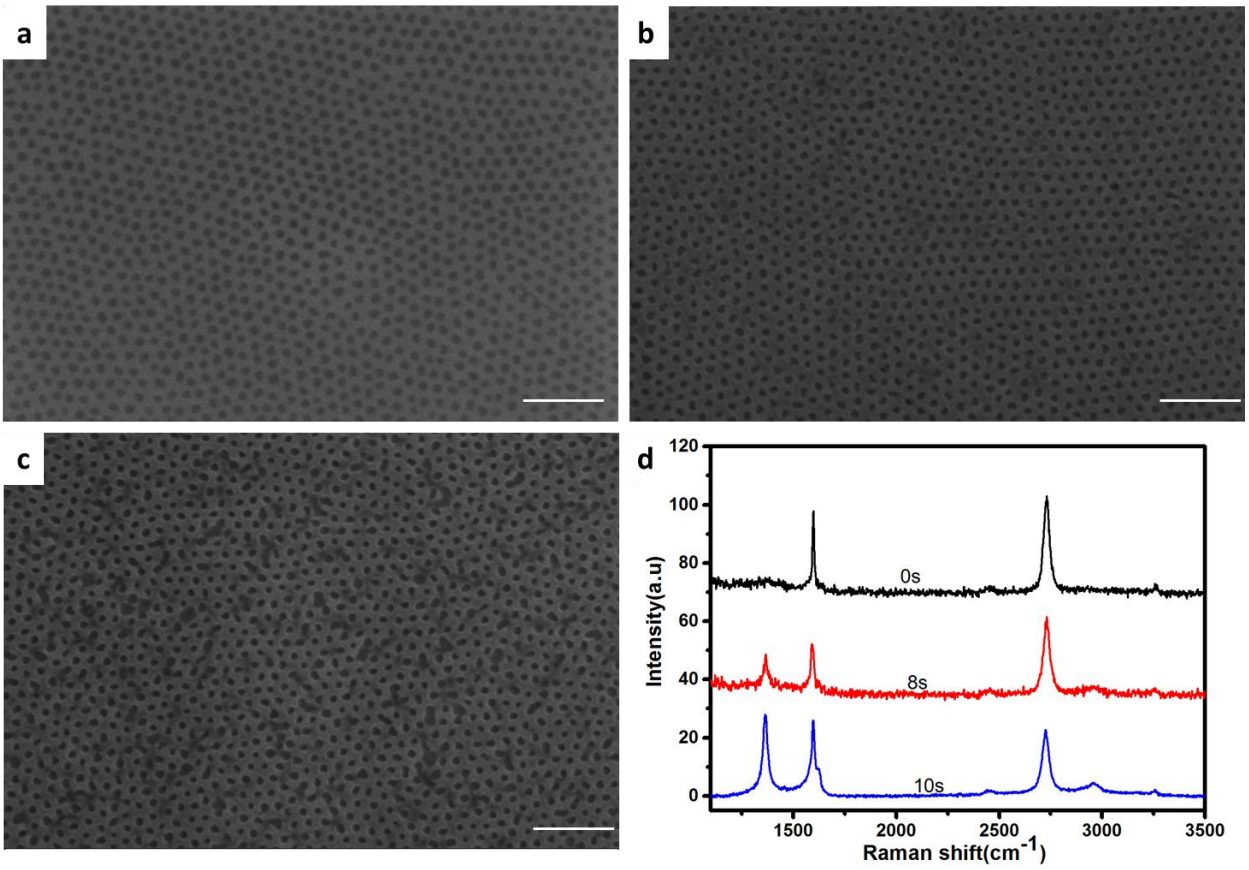

Figure 4.11 SEM images of GNM originated from SD42 after (a) 0 s, (b) 8 s and (c) 10 s of oxygen plasma etching. (d) Raman spectra for the GNM/Silicon oxycarbide nanomesh after different oxygen plasma etching time on SiO_2/Si substrate. Scale bars: 200 nm.

Here we examine reflection spectra for the GNM using Fourier transform infrared spectroscopy (FTIR, Bruker VERTEX 70) at room temperature with the reflection angle of 20°. The graphene plasmonic resonance is observed around 5250 cm^{-1} for the case an etching time of 8 s. As the oxygen plasma time increases, we observe an obvious blueshift from 1.87 μm for 8 s oxygen plasma (red line) to 1.72 μm for 10 s oxygen plasma (black line) as shown in Figure 4.12a. The plasmon modes in graphene nanostructures are strongly confined to the graphene plane due to the homogeneous graphene nanomesh, comparing graphene nanodisk arrays. We were also fabricated electrical devices based on the graphene nanomesh by depositing electrodes (Figure 4.12b). The study of graphene plasmonic by tuning voltage is ongoing.

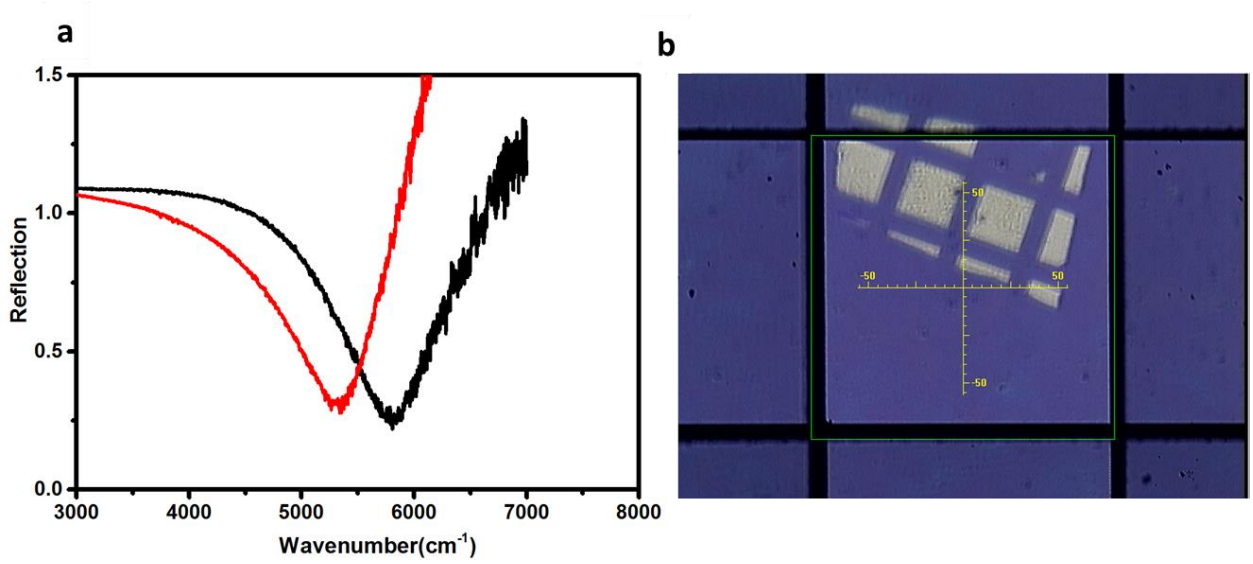

Figure 4.12 (a) Reflection spectra for the GNM/Silicon oxycarbide nanodisk formed after 8 s (red) and 10 s (black) of oxygen plasma. The dips are associated with the excitation of localized GPPs, leading to a strong absorption. (b) Optical image of a typical device for thr electrical gating methods tunable plasmons on nanomesh graphene.

Same method to fabricate big-sized graphene nanomesh has also been achieved in our lab. For SEM images of SD81 (Figure 4.13a, b, c), the contrast became clear after oxygen plasma etching and the size of period didn't change. Raman spectra (Figure 4.13d) show that after the oxygen plasma etching, a prominent disorder-induced D peak appears at 1358 cm^{-1}. In addition, the double-resonance 2D peak is weakened. These observations suggest the presence of a larger number of defects. The graphene plasmonic resonance is observed around 4230 cm^{-1} for the case of employing an etching time of 8 s. As the oxygen plasma time increases, we observe an obvious blueshift from 2.31 μm for 8 s oxygen plasma to 2.06 μm for 10 s oxygen plasma as shown in Figure 4.14.

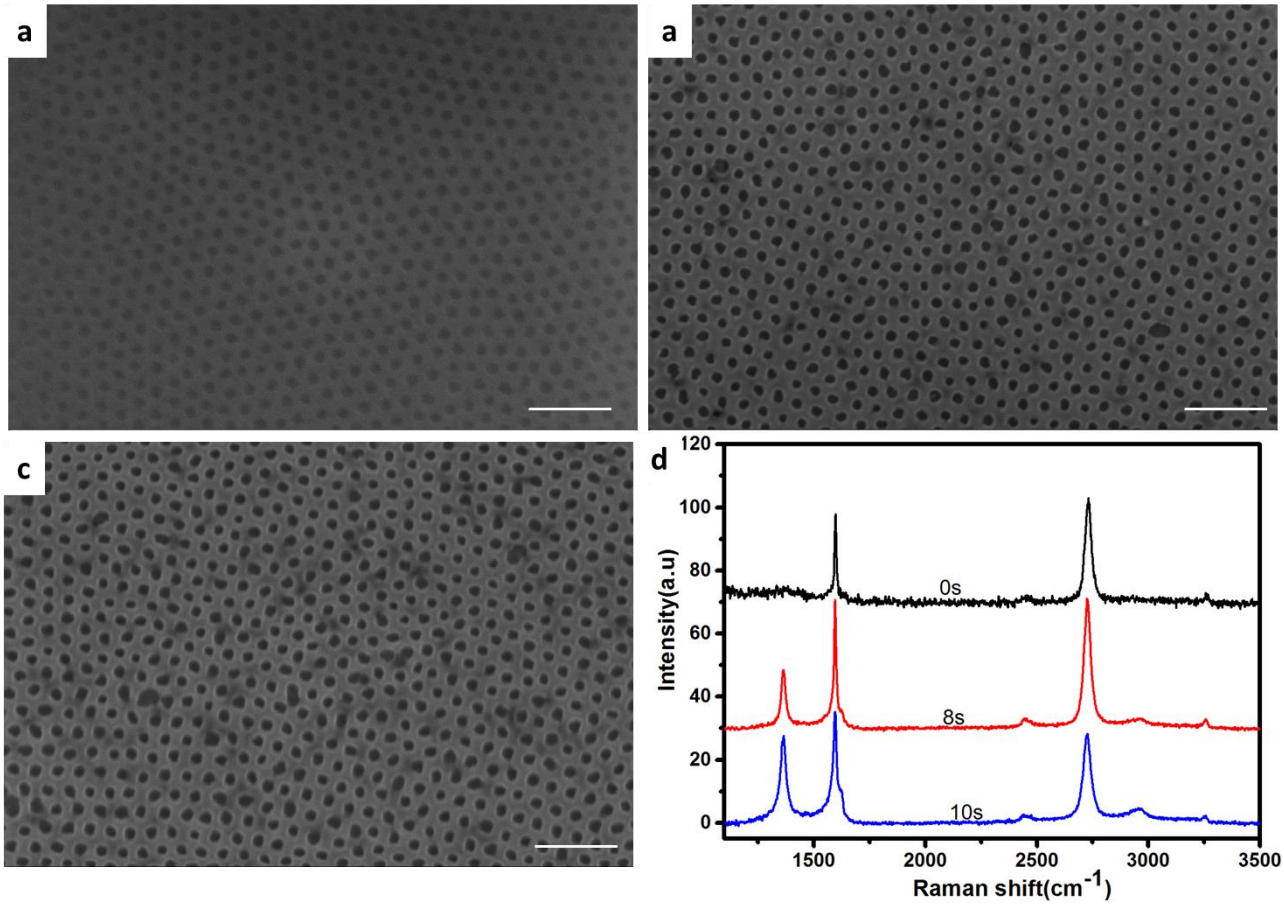

Figure 4.13 SEM images of GNM originated from SD81 after (a) 0 s, (b) 8 s and (c) 10 s of oxygen plasma etching. (d) Raman spectra for the GNM/Silicon oxycarbide nanomesh after different oxygen plasma etching time on SiO_2/Si substrate. Scale bars: 200 nm.

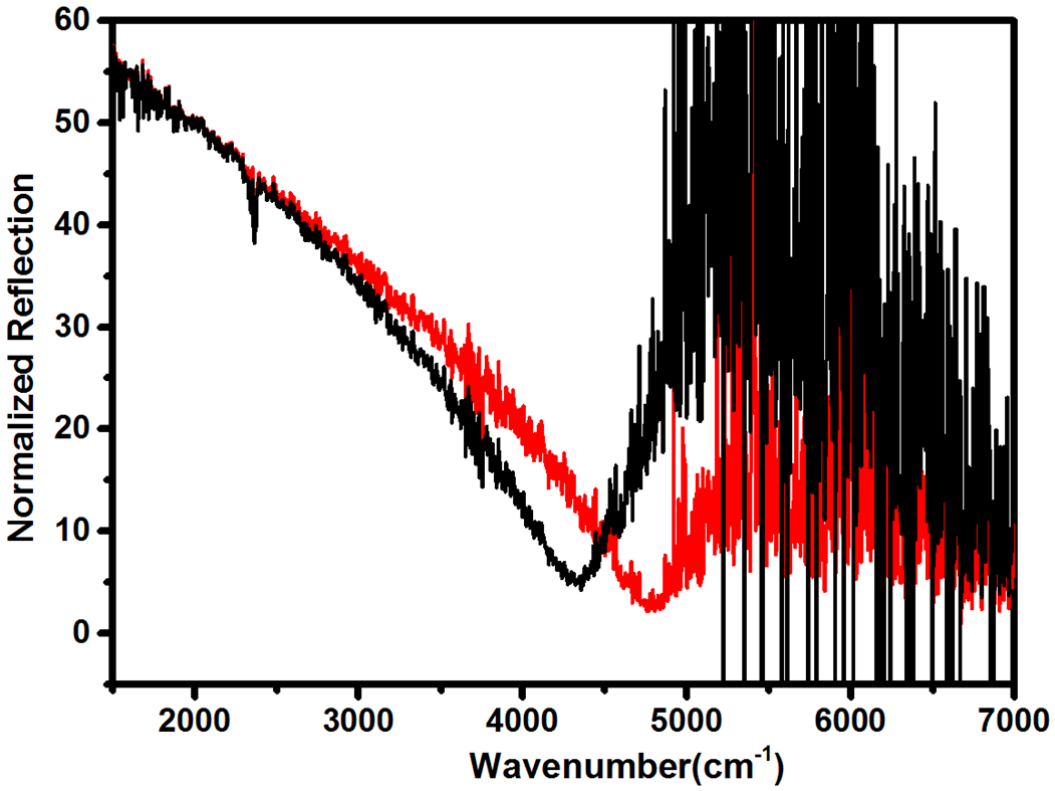

Figure 4.14 Reflection spectra for the GNM/Silicon oxycarbide nanomesh formed after 8 s (red) and 10 s (black) of oxygen plasma. The dips are associated with the excitation of localized GPPs, leading to a strong absorption.

4.4 Summary

In conclusion, we have achieved large-area fabrication of nanoscale graphene disk and nanomesh arrays, which support plasmon resonances in the near-infrared regime. We have used well-ordered vertically oriented cylinder and monolayer packed sphere morphologies to pattern graphene, and the dipole resonance of the GNDs plasmon polaritons has been pushed down to 2.0 μm and the GNMs plasmon polaritons has been pushed down to 1.7 μm, which is to the best of our knowledge the smallest value reported for the localized GPP resonance. With some further refinements, our results would facilitate graphene plasmons both for fundamental study and for potential applications in the telecommunication window. In fact, the technique that we are using can even produce smaller structures by appropriate choice of the block copolymer composition and molecular weight. The

same procedure can be applied to produce nanoscale structures in other 2D materials as a means to study their electronic or plasmonic properties.

4.5 References

1. F. Bonaccorso, Z. Sun, T. Hasan, A. Ferrari, Graphene photonics and optoelectronics. *Nature photonics* **4**, 611 (2010).
2. X. Gan *et al.*, Chip-integrated ultrafast graphene photodetector with high responsivity. *Nature photonics* **7**, 883 (2013).
3. T. Mueller, F. Xia, P. Avouris, Graphene photodetectors for high-speed optical communications. *Nature photonics* **4**, 297 (2010).
4. C.-H. Liu, Y.-C. Chang, T. B. Norris, Z. Zhong, Graphene photodetectors with ultra-broadband and high responsivity at room temperature. *Nature nanotechnology* **9**, 273 (2014).
5. I. Goykhman *et al.*, On-chip integrated, silicon–graphene plasmonic Schottky photodetector with high responsivity and avalanche photogain. *Nano Lett* **16**, 3005 (2016).
6. Y. Ding *et al.*, Effective electro-optical modulation with high extinction ratio by a graphene-silicon microring resonator. *arXiv preprint arXiv:1502.00480*, (2015).
7. C. T. Phare, Y.-H. D. Lee, J. Cardenas, M. Lipson, Graphene electro-optic modulator with 30 GHz bandwidth. *Nature photonics* **9**, 511 (2015).
8. M. Liu *et al.*, A graphene-based broadband optical modulator. *Nature* **474**, 64 (2011).
9. D. Ansell *et al.*, Hybrid graphene plasmonic waveguide modulators. *Nature communications* **6**, (2015).
10. Z. Sun, A. Martinez, F. Wang, Optical modulators with 2D layered materials. *Nature photonics* **10**, 227 (2016).
11. W. Li *et al.*, Ultrafast all-optical graphene modulator. *Nano Lett* **14**, 955 (2014).
12. Q. Bao *et al.*, Atomic‐layer graphene as a saturable absorber for ultrafast pulsed lasers. *Advanced Functional Materials* **19**, 3077 (2009).
13. F. Wang, A. Rozhin, V. Scardaci, Z. Sun, F. Hen nrich, IH White, WI Milne, and AC Ferrari. *Nature Nanotechnol* **3**, 738 (2008).
14. T. Hasan *et al.*, Nanotube–polymer composites for ultrafast photonics. *Advanced Materials* **21**, 3874 (2009).
15. R. R. Nair *et al.*, Fine structure constant defines visual transparency of graphene. *Science* **320**, 1308 (2008).
16. X. Zhu *et al.*, Enhanced light-matter interaction in graphene-covered gold nanovoid arrays. *arXiv preprint arXiv:1306.1555*, (2013).
17. M. Furchi *et al.*, Microcavity-integrated graphene photodetector. *Nano Lett* **12**, 2773 (2012).
18. X. Gan *et al.*, Strong enhancement of light–matter interaction in graphene coupled to a photonic crystal nanocavity. *Nano Lett* **12**, 5626 (2012).
19. T. Echtermeyer *et al.*, Strong plasmonic enhancement of photovoltage in graphene. *arXiv preprint arXiv:1107.4176*, (2011).
20. F. G. de Abajo, A. Photonics, 1, 135–152 (2014). *CrossRef, CAS, Web of Science® Times Cited* **79**.
21. A. Grigorenko, M. Polini, K. Novoselov, Graphene plasmonics. *Nature photonics* **6**, 749 (2012).
22. S. Xiao, X. Zhu, B.-H. Li, N. A. Mortensen, Graphene-plasmon polaritons: From fundamental properties to potential applications. *Frontiers of Physics* **11**, 1 (2016).

23. M. Jablan, H. Buljan, M. Soljačić, Plasmonics in graphene at infrared frequencies. *Physical Review B* **80**, 245435 (2009).
24. J. Chen *et al.*, Optical nano-imaging of gate-tunable graphene plasmons. *Nature* **487**, 77 (2012).
25. Z. Fei *et al.*, Gate-tuning of graphene plasmons revealed by infrared nano-imaging. *Nature* **487**, 82 (Jul 5, 2012).
26. X. Zhu *et al.*, Experimental observation of plasmons in a graphene monolayer resting on a two-dimensional subwavelength silicon grating. *Applied Physics Letters* **102**, 131101 (2013).
27. A. Woessner *et al.*, Highly confined low-loss plasmons in graphene–boron nitride heterostructures. *Nature materials* **14**, 421 (2015).
28. T. Low, P. Avouris. (PMID).
29. H. Yan *et al.*, Damping pathways of mid-infrared plasmons in graphene nanostructures. *Nature photonics* **7**, 394 (2013).
30. Z. Fang *et al.*, Gated tunability and hybridization of localized plasmons in nanostructured graphene. *ACS nano* **7**, 2388 (2013).
31. Z. Fang *et al.*, Active tunable absorption enhancement with graphene nanodisk arrays. *Nano Lett* **14**, 299 (2013).
32. W. Wang, B.-H. Li, E. Stassen, N. A. Mortensen, J. Christensen, Localized surface plasmons in vibrating graphene nanodisks. *Nanoscale* **8**, 3809 (2016).
33. F. Koppens, D. Chang, F. García de Abajo, Graphene plasmonics: a platform for strong light-matter interactions. *Nano Lett* **11**, 3370 (2011).
34. W. Wang, S. Xiao, N. A. Mortensen, Localized plasmons in bilayer graphene nanodisks. *Physical Review B* **93**, 165407 (2016).
35. P. A. D. Goncalves, N. M. Peres, *An Introduction to Graphene Plasmonics*. (World Scientific, 2016).
36. J. Cai *et al.*, Atomically precise bottom-up fabrication of graphene nanoribbons. *Nature* **466**, 470 (2010).
37. T. Li, Z. Wang, L. Schulte, S. Ndoni, Substrate tolerant direct block copolymer nanolithography. *Nanoscale* **8**, 136 (2016).
38. T. Li, Z. Wang, L. Schulte, O. Hansen, S. Ndoni, Fast & scalable pattern transfer via block copolymer nanolithography. *RSC Advances* **5**, 102619 (2015).
39. R. A. Farrell *et al.*, Large-scale parallel arrays of silicon nanowires via block copolymer directed self-assembly. *Nanoscale* **4**, 3228 (2012).
40. S. Ndoni, P. Jannasch, N. B. Larsen, K. Almdal, Lubricating effect of thin films of styrene-dimethylsiloxane block copolymers. *Langmuir* **15**, 3859 (1999).
41. Z. Wang, T. Li, L. Schulte, K. Almdal, S. Ndoni, Photocatalytic nanostructuring of graphene guided by block copolymer self-assembly. *ACS Applied Materials & Interfaces* **8**, 8329 (2016).
42. A. C. Ferrari, D. M. Basko, Raman spectroscopy as a versatile tool for studying the properties of graphene. *Nature nanotechnology* **8**, 235 (2013).
43. S. Thongrattanasiri, A. Manjavacas, F. J. García de Abajo, Quantum finite-size effects in graphene plasmons. *ACS nano* **6**, 1766 (2012).
44. T. Christensen, W. Wang, A.-P. Jauho, M. Wubs, N. A. Mortensen, Classical and quantum plasmonics in graphene nanodisks: Role of edge states. *Physical Review B* **90**, 241414 (2014).
45. W. Wang *et al.*, Plasmonic eigenmodes in individual and bow-tie graphene nanotriangles. *Scientific reports* **5**, 9535 (2015).

46. S. Raza, S. I. Bozhevolnyi, M. Wubs, N. A. Mortensen, Nonlocal optical response in metallic nanostructures. *Journal of Physics: Condensed Matter* **27**, 183204 (2015).
47. S. Rasappa *et al.*, High quality sub-10 nm graphene nanoribbons by on-chip PS-b-PDMS block copolymer lithography. *RSC Advances* **5**, 66711 (2015).
48. C. Berger *et al.*, Electronic confinement and coherence in patterned epitaxial graphene. *Science* **312**, 1191 (2006).
49. X. Yang *et al.*, Far‐Field Spectroscopy and Near‐Field Optical Imaging of Coupled Plasmon‐Phonon Polaritons in 2D van der Waals Heterostructures. *Advanced Materials* **28**, 2931 (2016).

5. Chemical Nanopatterning of Graphene assisted in-situ fabricated polymer mask

This chapter was adapted from "Selective photochemical functionalization of graphene with block copolymer" Safron, N. S.; Zhongli Wang, Kristoffer Almdal, Lars Schulte, Sokol Ndoni. Publication upcoming.

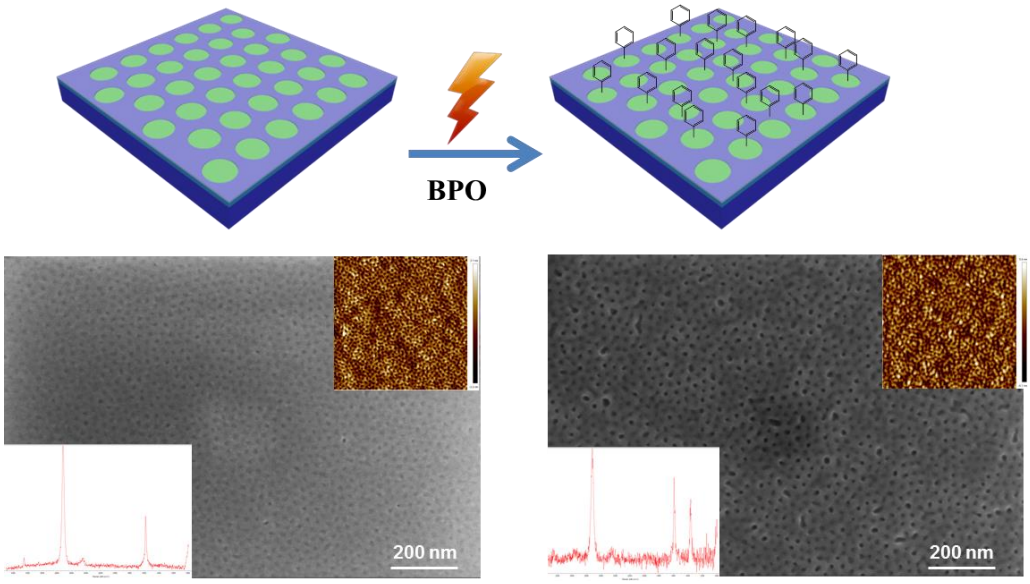

5.1 Introduction

Graphene is a rapidly rising star on the horizon of materials science and condensed-matter physics. The strictly two-dimensional material exhibits exceptionally crystal and electronic quality, has already revealed a cornucopia of new physics and potential applications. The unique and superior properties of graphene make it a broad range of applications including transistors, integrated circuits, displays, sensors, and nanocomposite materials (*1-5*). Despite its high potentials, major challenges still remain. These include intrinsic zero energy band gap, low reactivity and limited availability of well-defined pristine graphene, which have hampered the rapid development of graphene-based functional devices. Chemical functionalization of graphene is among several solutions to address the above challenges of graphene. Through synthetic chemistry methods, the preparation of p- and n-doped graphene has been achieved based on the section of electron donating- or withdrawing-complexes covalently bonded to the graphene plane. Except for this

tunable conductivity, some other properties of graphene, such as solubility and stability, can also be enhanced by chemical functionalization.

In recent years, graphene chemistry has been overviewed to emphasize the importance of chemical functionalization of graphene. In principle, covalent functionalization of pristine graphene requires reactive species that can form covalent adducts with the sp^2 carbon structures in graphene, therefore graphene is normally functionalized by using reactive intermediates, such as radicals, nitrenes, carbenes, and arynes (Figure 5.1) and based on covalent reactions include free radical addition, CH insertion, and cycloaddition reactions as below.

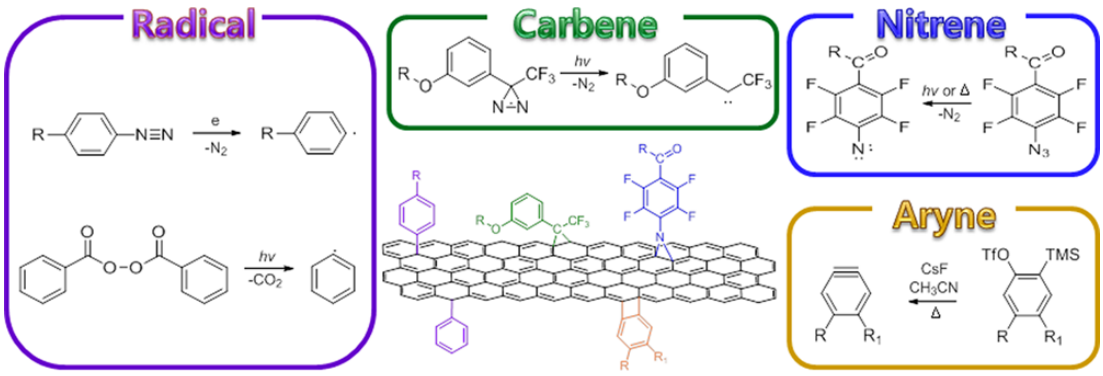

Figure 5.1 Schematic of the graphene functionalization reactions using reactive intermediates of radicals, nitrenes, carbenes, and arynes (*6*)

Photochemical Reaction

A photochemical reaction between graphene and benzoyl peroxide was reported by L. E. Brus in 2009 (*7*), which is a typical example based on free radical addition. The reaction introduces spatially localized defects into the basal plane of graphene, which are sp3 carbon centers produced by phenyl radical attack on the basal plane.

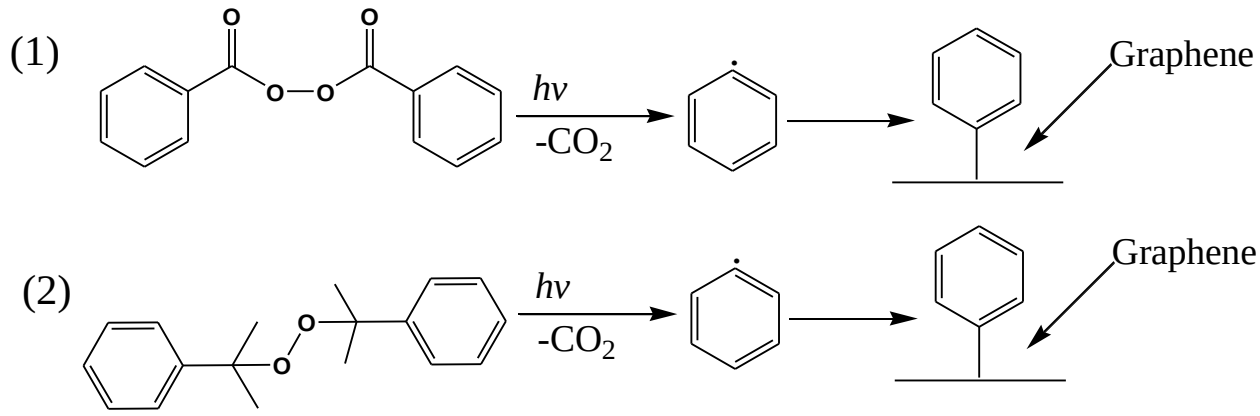

Figure 5.2 The reaction between graphene and benzoyl peroxide (*7*). (2) The synthesis route proposed for Dicumyl peroxide functionalized graphene.

Electrophilic substitution

At the same time, motived by the single adsorbed molecules modifying the band structure and affecting the electronic properties of graphene significantly, group Wendelin J. Stark found a robust and highly precise doping method to alter the electronic structure of graphene sheets (*8*). The approach to covalent graphene modification is shown in Figure 5.3. The graphene sample was first patterned by lithography, so that an unfunctionalized graphene surface would be preserved below the photoresist. The unmasked areas were functionalized by exposure to highly diluted diazonium reagents. After removal of the photoresist, the graphene surface was investigated. The chemical derivatization depends strongly on the reaction time, the concentration of the reactants, and a successful washing procedure. The reaction time and concentration control the amount of covalent derivatization of the graphene surface by dopants at a constant temperature.

To further test the validity of the Hammett correlation for graphene, they measured the surgace potential by changing the substituents from p-methoxyphenyl to p-iodophenyl, p-sulfophenyl, and p-carboxyphenyl. Then they found that there is a clearly qualitative correlation between surface potential and Hammett constant.

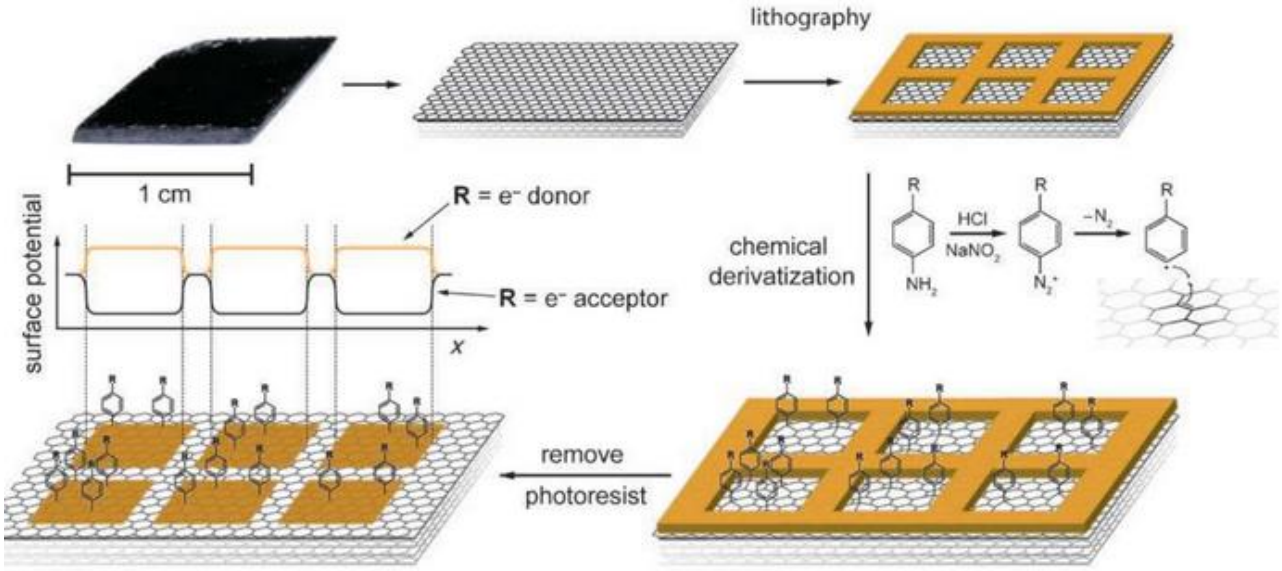

Figure 5.3 Patterned functionalization of graphene surface: First, a patterned mask is created by photo-lithography on the graphene. The unmasked regions are then exposed to adiazonium reagent. The photoresist is removed prior to analysis.

Nucleophilic addition

The Bingel reaction originated from the cyclopropanation chemistry of fullerene. It utilizes a halide derivative of the diethylmalonate moiety in the presence of a base such as 1,8-diazabicyclo[5.4.0]undec-7-ene or sodium hydride. Its finding shows the simplest reactiob conditions required in graphene chemistry. A novel and efficient solvent capable of creating stable graphene suspensions from graphite was introduced in the form of benzylamine, and its efficiency during simple sonication of intact graphite was established by N. Tagmatarchis (*9*). This allowed the use of the exfoliated graphene dispersion to covalently graft malonate moieties along the graphitic skeleton, following the Bingel reaction conditions and using microwave irradiation.

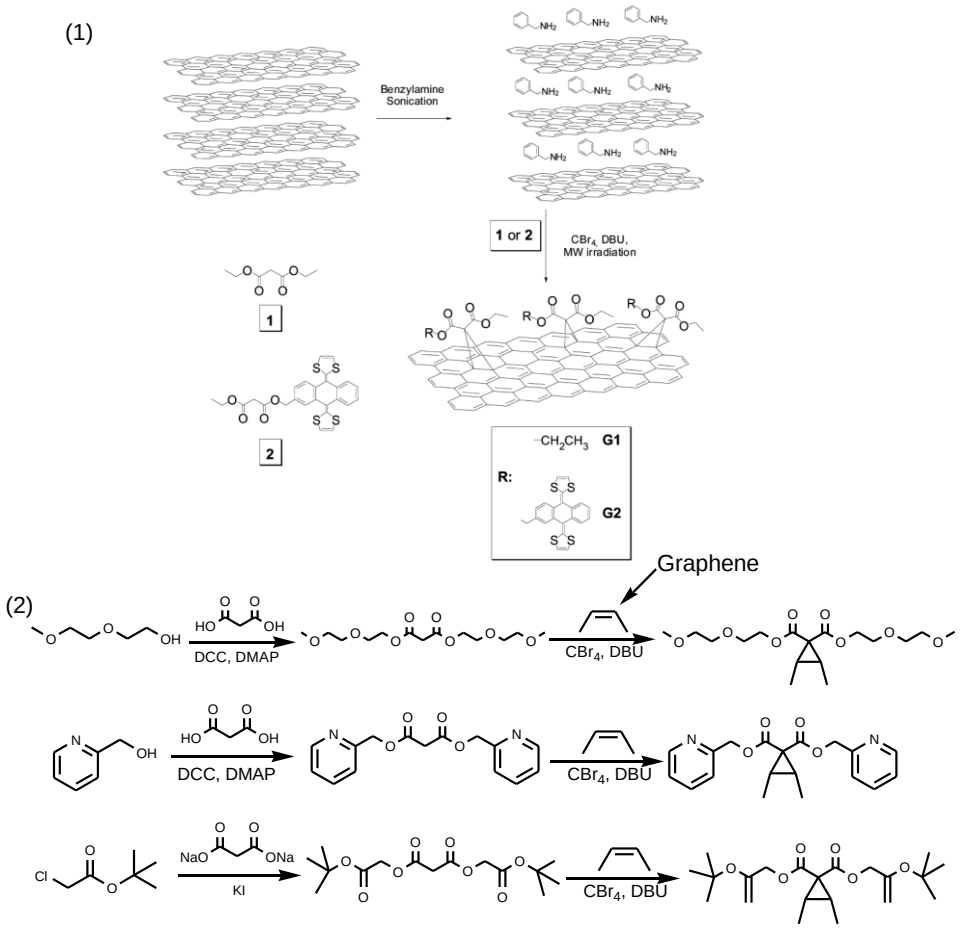

Figure 5.4 (1) Synthetic procedure affording functionalized graphene-based materials **G1** and **G2 (*9*)**. (2)The synthesis route proposed for the diethylmalonatemoiety functionalized graphene.

[3+2] Cycloaddition

1, 3-Dipolar cycloaddition has been successfully applied in the organic functionalizing of a wide range of carbon nanostructures, e.g., fullerenes, nanotubes, onions, nanohorns, affording a plethora of organic derivatives with interesting applications - in polymer composites, biotechnology, drug delivery, solar cells, etc. Figure 5.5 shows the reaction that the graphene sheets derived from dispersion of graphite in solution by a combination of extended bath sonication and careful centrifugation (*10*).

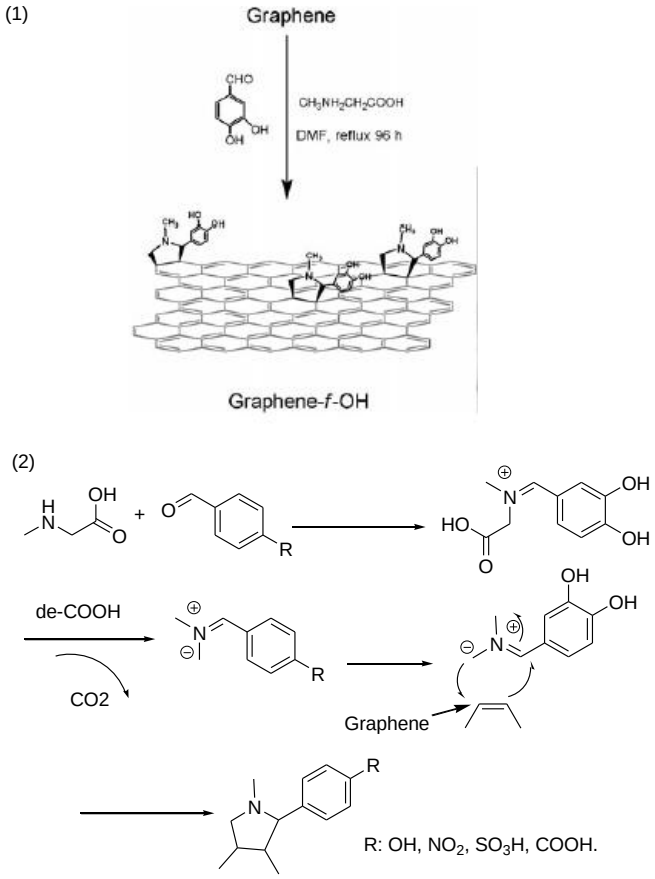

Figure 5.5 (1) Schematic representation of the 1, 3 dipolar cycloaddition of azomethineylide on graphene (*10*). (2) The synthesis route proposed for the 1, 3 dipolar cycloaddition of azomethineylide on graphene.

5.2 Chemical Nanopatterning of Graphene

Based on top knowledge and the electronic and photonic applications, we have successfully achieved periodic chemical functional graphene combing block copolymer nanolithography at Nano-scale size. The single layer graphene was first spinning coat block copolymer PS-b-P2VP, getting a periodic nanostructure after solvent annealing (*11-14*). Then the sample immersed into ethanol for a certain time to open the Nano holes. So a covered graphene surface would be preserved below the photoresist. The unmasked areas were functionalized by exposure to highly diluted diazonium reagents (Figure 5.6). After removal of the photoresist, the graphene surface was investigated by scanning electron microscopy (SEM) and atomic force microscopy (AFM) in

tapping mode to image the relative surface-potential levels of modified and native areas of the graphene surface.

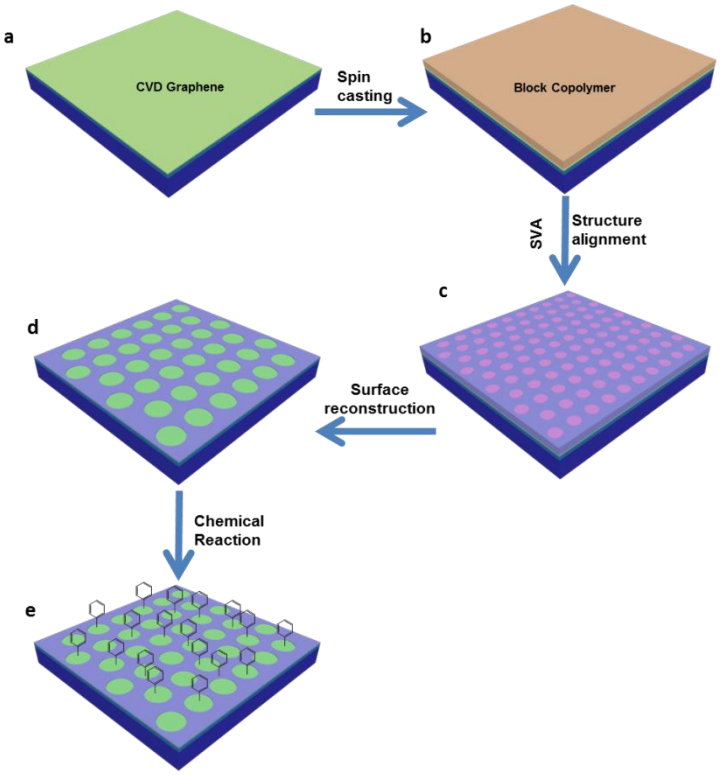

Figure 5.6 Schematic illustration of the process for chemical graphene anti-dots lattices. (a) Spin coating of block copolymer thin film directly on SiO_2/Si substrate. (b) Structure alignment via solvent vapor annealing (SVA) of block copolymer. (c) Surface reconstruction of the ordered films. (d) Selective functionalization of graphene surface via the benzoyl peroxide chemistry, UV irradiation at ambient conditions.

Here we took patterned block copolymer as mask for chemical functionalization of graphene. Each pore functioned as a Nanoreactor for the heterogeneous chemical modification of the graphene which thus create what we called chemical graphene anti-dots lattices (C-GALs). The patterned interruption of graphene conjugation in C-GALS can change its electronic properties; In addition, the mechanical strength can be better preserved in the meantime, additional function e.g. for sensing would become possible.

Mask fabrication

Several block copolymers have been developed in our group of nano-porous polymers at DTU Nanotech, such as 1, 2-polybutadine-b-dimethylsiloxane, poly (styrene-b-dimethylsiloxane), polystyrene-block-poly (ethylene oxide) and polystyrene-b-poly (2-vinylpyridine), which allows us to explore facile methods to chemically pattern graphene. Here we report on the extremely simple and efficient fabrication of thin film with highly ordered, straight nanopores by fast alignment of perpendicular cylinders in thin BCP films and the subsequent nondestructive transformation of the aligned cylinders into uniform straight pores. Amphiphilic block copolymer of cylinder-forming polystyrene-block-poly- (2-vinylpyridine) (PS-b-P2VP) films with thicknesses around 15 nm was perpendicularly aligned ultrafast in the process of spin-coating. Simply, we annealed BCP films during the spin-coating process then immerse it in ethanol for half an hour. After drying it in air, , the originally dense BCP films can be nondestructively converted into porous thin-film.

Chemical modification of graphene

Single layer graphene was purchased onto Si wafer having 90 nm of thermal oxide. The thickness of the graphene was determined using Raman spectroscopy. The graphene on the Si wafer was immersed in a quartz UV-Vis cuvette that was filled with benzoyl peroxide solution (20 mM in toluene). Photochemical reaction was carried out by focusing a laser beam (Ar-ion: 514 nm; 0,4 mW) onto the graphene flake in the solution. The spot size is ~ 0.5 µm. The defect formation can be observed in a short enough exposure time. Photoexcitation is required for this reaction. To demonstrate this, graphene on the Si wafer was immersed in a quartz UV-Vis cuvette that was filled with benzoyl peroxide solution without laser illumination. We observed no significant D band in these reactions.

The experimental approach to covalent graphene modification is shown in Figure 5. 6e, CVD graphene was first patterned by BCP self-assembly, so that (unfunctionalized) graphene surface would be preserved below the thin BCP films. The unmasked areas were functionalized by exposure to highly diluted benzoyl peroxide. During the entire reaction process, the graphene surface was characterized by scanning electron microscopy (SEM), AFM and XPS. It was found that the chemical derivatization depends strongly on the reaction time, the concentration of the reactants, and a successful washing procedure. The first two parameters control the amount of covalent derivatization of the graphene surface by dopanting at a constant temperature.

Figure 5.9 shows the SEM images of PS-b-P2VP on the same single-layer graphene before and after the photochemical reaction with absorbed benzoyl peroxide. The simple process of solvent evaporation can produce ordered arrays of cylindrical microdomains oriented normal to the surface of block copolymers with long-range lateral order (Figure 5.7a). Solvent evaporation presents a simple route not only in controlling the alignment of the microdomain morphology, but also in enhancing the lateral order of microdomains in BCP thin films. Ordered arrays of cylindrical micro domains oriented normal to the surface were obtained during spin-coating process (Figure 5.7a). When the thin film was immersed in ethanol, a good solvent for P4VP and a nonsolvent for PS, a reconstruction of the film was observed where ordered arrays of nanoscopic pores were formed (Figure 5.7b, c). Surface reconstruction is a process where, upon exposure of the BCP film to a solvent that is a good solvent for the minor component block and a nonsolvent for the major component block, the minor component is drawn to the surface of the film, and, upon drying, cylindrical nanopores are produced with dimensions comparable to the original cylindrical microdomains. The surface of the film is also covered with the minor component block. The reconstruction of the film maintains the well-developed microdomain structure and the sharpened distribution of size and center-to-center distance between the nanoscopic pores, as in the solvent

annealed films (*15*) (*17*). It should be noted that reconstruction method can be used to generate nanoscopic pores without removal of the minor component block by chemical or photolytic degradation, as is the case with some other BCPs (*17-19*). In addition, the BCP after exposure to the preferential solvent is unchanged. Because the glass transition of the PS is well above room temperature, the nanopores are maintained since the PS matrix is glassy.

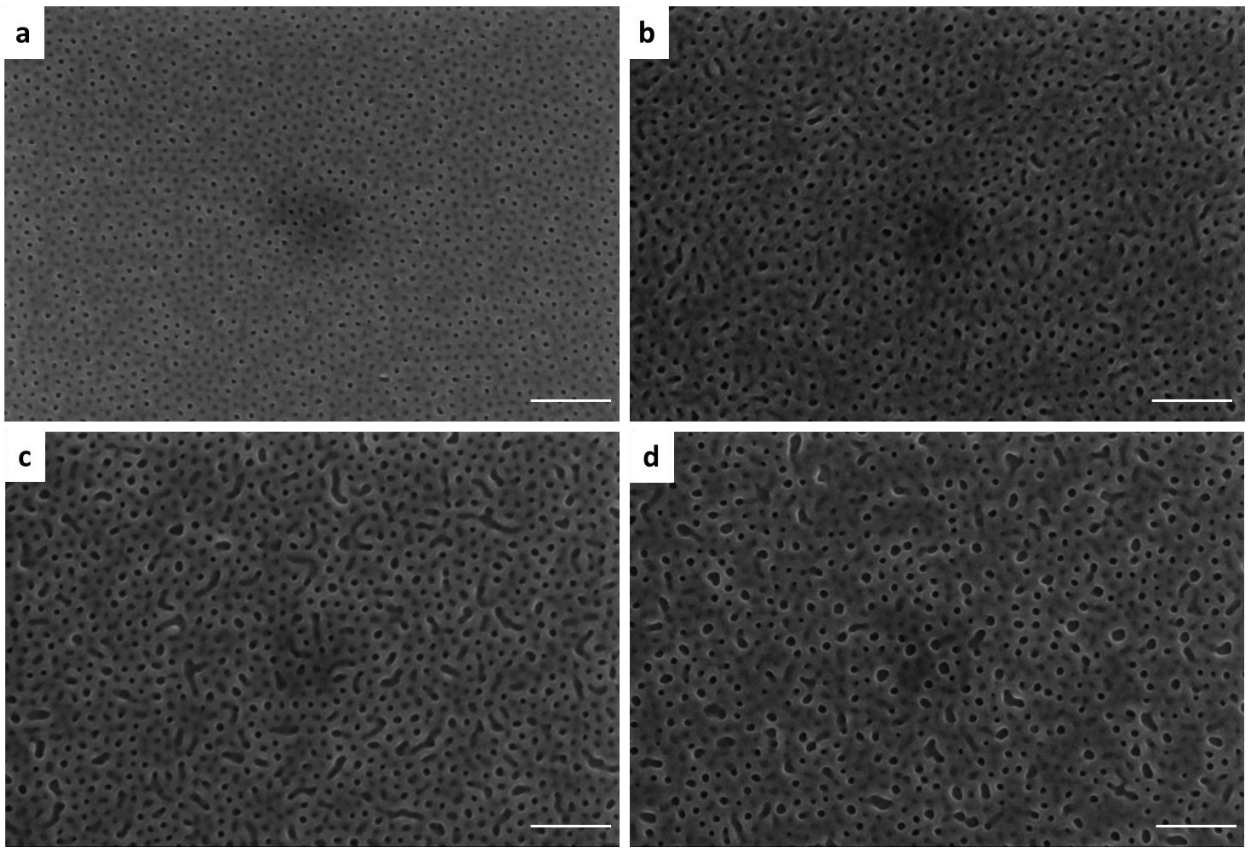

Figure 5.7 SEM images of PS-b-P2VP on the same single layer graphene before and after the photochemical reaction with absorbed benzoyl peroxide (a) 0 h, (b) 2 h, (c) 4 h and (d) 8 h. Scale bars: 200 nm.

However during our process the surface reconstruction occurred together with the photochemical reaction. We dissolved benzoyl peroxide into ethanol, then immersed graphene sample into the dissolved solution and reacted under UV irradiation. The mask morphology was unfolded (Figure 5.7 b, c, d) in certain degree due to the chemical reaction at the same time. Because of the additional

photochemical reaction happening, the mask morphology becomes more and more disorder (Figure 5.7 d).

We also used AFM to investigate the effect of masks during the reaction process (Figure 5.8 a b, c,), The similar nanostructure morphologies trend is in accordance the above SEM results. The systematic of the photochemical reaction were studied with micro Raman spectroscopy. Figure 5.8d shows the time evolution of the Raman spectrum of a single-layer graphene during the reaction, revealing the evolution of defect formation. For the pristine CVD graphene used in this study, only a very small Raman D peak is observed, indicative of its high quality. After the photochemical reaction, a prominent disorder-induced D peak appears at 1358 cm^{-1}. In addition, the double-resonance 2D peak is weakened. Additionally, the intensity ratio between Raman D and G peaks (I(D)/I(G), commonly used to characterize disorder in graphene), is observed to increase with the time of photochemical reaction. I(D)/I(G) ratio increased from 0.03 for 0 h to 0.18 for 2 h, 1,04 for 4 h, 1,69 for 8 h, and 1,92 for 16 h as shown in Figure 5.10d. It indicates that the sp^2 carbon network of graphene has been broken into nanometer sized domains.

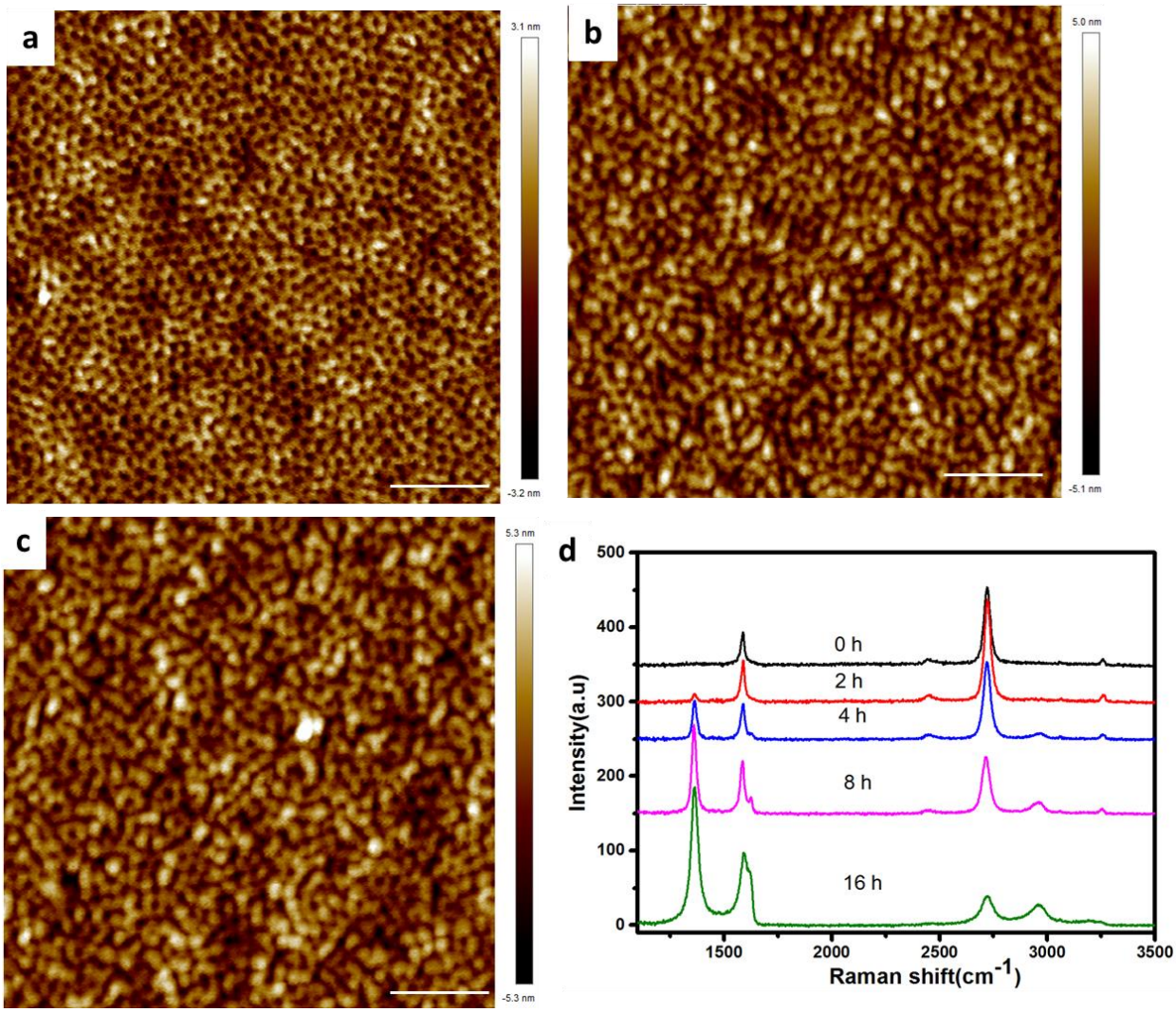

Figure 5.8 AFM images of PS-b-P2VP on the same single-layer graphene before and after the photochemical reaction with absorbed benzoyl peroxide (a) 0 h, (b) 2 h and (c) 4 h. (d) Raman spectra of the same single layer graphene before and after phenyl-functionalized graphene. Scale bars: 200 nm.

We used SEM and AFM to investigate the pristine graphene morphology (Figure 5.9a and b) and the chemical functional graphene morphology after removing the BCP mask. (Figure 5.9 c and d). We found that there were dots structures after photochemical reaction for 4 h. This agrees with the Raman data. However, the chemical functional graphene became disordered completely based on AFM and SEM images (Figure 5.9c, d). We couldn't define clearly the functional area due to the

limitation resolution by using AFM and SEM. Therefore, our next plan is to quantify how many phenyls successfully grafted on the porous area of CVD graphene by using TEM.

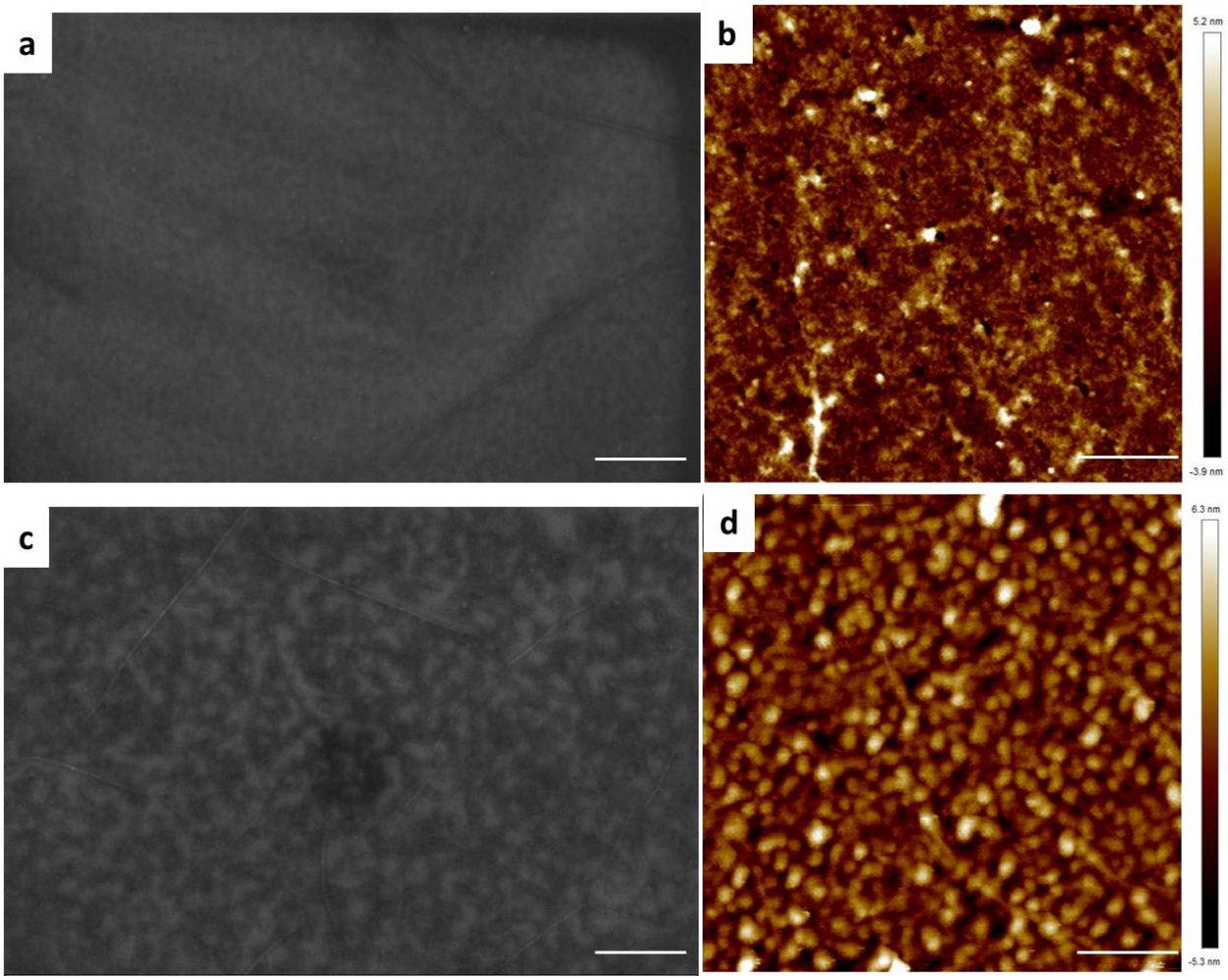

Figure 5.9 SEM image (a) and AFM image (b) of single layer graphene before the photochemical reaction with absorbed benzoyl peroxide. SEM image (c) and AFM image (d) of the same single layer graphene after 4 h photochemical reaction with absorbed benzoyl peroxide, without BCP mask. Scale bars: 200 nm.

In addition, XPS was used to characterize the crystallization of graphene by analyzing C1s spectrum. Generally, the C1s spectrum shows a broad, asymmetric tail towards higher binding energy (Figure 5.10, 0 h); while for high concentrations of sp^3-bonded carbon, the C1s peak will have a more symmetric shape and slightly shift to higher binding energy. The sp^3 carbon peak

should be 1eV higher to the binding energy side of the sp^2 component. In our case, XPS studies revealed the nature of the carbon bonds present in the sample (Figure 5.10). The CVD graphene contained sp^2 hybridized carbon atoms, showing the high quality of graphene (Figure 5.10 0 h). The sample contained sp^2 and sp^3 hybridized carbon atoms after 2 h photochemical reaction, and the rest of the carbonaceous material was protected by BCP mask. After 8 h photochemical reaction, the binding energy shifted from 284 eV to 284. 8 eV, proving most area of the sample contained sp^3 hybridized atoms. All these evidences were consisted with the hybridized theory of carbon atoms. We concluded that phenyl-functionalized graphene has contained both components of sp^2 and sp^3 C.

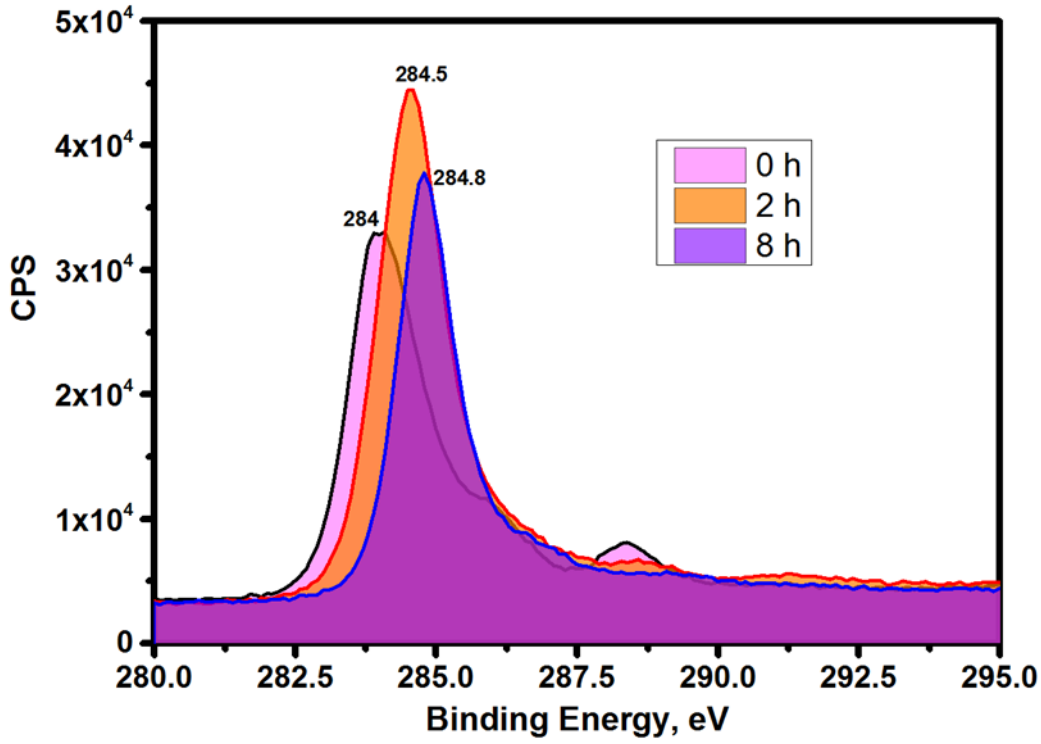

Figure 5.10 XPS of the same single layer graphene before and after phenyl-functionalized graphene.

5.4 Summary

In conclusion, a chemical reaction on graphene was achieved in the presence of a nanoporous mask of hexagonal morphology; we have shown that graphene reacts with benzoyl peroxide under intense laser irradiation, producing significant defects in the basal plane. For the first time, we adapted chemical functionalization to the nanoporous mask at nano-scale size on top of graphene. Each pore in this case functioned as a nanoreactor for the heterogeneous chemical modification of the graphene at the bottom of the pore. We propose that a hot electron initiates an electron transfer from photoexcited graphene to the physisorbed benzoyl peroxide. This electron transfer produced a transient benzoyl peroxide radical anion, which irreversibly decomposes to produce the phenyl radical, which introduces sp^3 defect centers onto the basal plane of graphene. We believe that chemical GALs offer a prospective platform for both fundamental studies of new physical phenomena and applications in revolutionary new devices in such different areas as solid state quantum computing, as thermoelectric components, and even as parallelized biomolecule sensing.

5.5 References

1. S. Stankovich *et al.*, Graphene-based composite materials. *Nature* **442**, 282 (2006).
2. C. E. Hamilton, J. R. Lomeda, Z. Sun, J. M. Tour, A. R. Barron, High-yield organic dispersions of unfunctionalized graphene. *Nano Lett* **9**, 3460 (2009).
3. M. Fang, K. Wang, H. Lu, Y. Yang, S. Nutt, Covalent polymer functionalization of graphene nanosheets and mechanical properties of composites. *Journal of Materials Chemistry* **19**, 7098 (2009).
4. J. Choi, K.-j. Kim, B. Kim, H. Lee, S. Kim, Covalent functionalization of epitaxial graphene by azidotrimethylsilane. *The Journal of Physical Chemistry C* **113**, 9433 (2009).
5. Y. Shao *et al.*, Graphene based electrochemical sensors and biosensors: a review. *Electroanalysis* **22**, 1027 (2010).
6. J. Park, M. Yan, Covalent functionalization of graphene with reactive intermediates. *Accounts of chemical research* **46**, 181 (2012).
7. H. Liu *et al.*, Photochemical reactivity of graphene. *Journal of the American Chemical Society* **131**, 17099 (2009).
8. F. M. Koehler *et al.*, Permanent Pattern‐Resolved Adjustment of the Surface Potential of Graphene‐Like Carbon through Chemical Functionalization. *Angewandte Chemie International Edition* **48**, 224 (2009).

9. S. P. Economopoulos, G. Rotas, Y. Miyata, H. Shinohara, N. Tagmatarchis, Exfoliation and chemical modification using microwave irradiation affording highly functionalized graphene. *ACS nano* **4**, 7499 (2010).
10. V. Georgakilas *et al.*, Organic functionalisation of graphenes. *Chemical Communications* **46**, 1766 (2010).
11. L. Schulte *et al.*, Nanoporous materials from stable and metastable structures of 1, 2-PB-b-PDMS block copolymers. *Polymer* **52**, 422 (2011).
12. S. Ndoni, M. E. Vigild, R. H. Berg, Nanoporous materials with spherical and gyroid cavities created by quantitative etching of polydimethylsiloxane in polystyrene− polydimethylsiloxane block copolymers. *Journal of the American Chemical Society* **125**, 13366 (2003).
13. T. Li, Z. Wang, L. Schulte, O. Hansen, S. Ndoni, Fast & scalable pattern transfer via block copolymer nanolithography. *RSC Advances* **5**, 102619 (2015).
14. T. Li, Z. Wang, L. Schulte, S. Ndoni, Substrate tolerant direct block copolymer nanolithography. *Nanoscale* **8**, 136 (2016).
15. S. Park, B. Kim, J. Y. Wang, T. P. Russell, Fabrication of highly ordered silicon oxide dots and stripes from block copolymer thin films. *Advanced Materials* **20**, 681 (2008).
16. S. Park, J.-Y. Wang, B. Kim, W. Chen, T. P. Russell, Solvent-induced transition from micelles in solution to cylindrical microdomains in diblock copolymer thin films. *Macromolecules* **40**, 9059 (2007).
17. T. Thurn-Albrecht *et al.*, Ultrahigh-density nanowire arrays grown in self-assembled diblock copolymer templates. *Science* **290**, 2126 (2000).
18. H. Mao, M. A. Hillmyer, Macroscopic samples of polystyrene with ordered three-dimensional nanochannels. *Soft Matter* **2**, 57 (2006).
19. P. Du *et al.*, Additive‐driven phase‐selective chemistry in block copolymer thin films: the convergence of top‐down and bottom‐up approaches. *Advanced Materials* **16**, 953 (2004).

6. Summary and Conclusion

6.1 Summary

The work explored and presented in this thesis is to develop self-assembly methods of block copolymer for functionalizing nano-materials especially 2D materials on the large-scale where traditional techniques are difficult to be used.

Firstly, an efficient solvent annealing process is well-developed on several kinds of BCPs. Well-ordered perpendicular cylindrical pattern can be achieved afterward. The selective of solvent, film thickness and annealing time play an important role in determining the final structure. By following we have shown that a simple reconstruction of the organic BCPs (PS-b-P2VP/PS-b-P4VP) can provide etching contrast and allow the patterning of BCP mask for subsequent pattern transferring into the underlying substrate. In addition, we have also reported a new block copolymer PF9MA-PFMMA ($PF9_{35k}F_{25}$) hexagonally packed cylinder morphology using this efficacy annealing method. These self-assembly and lithography methods for BCPs will be used in the following chapters.

Secondly, uniform graphene nanomesh and nanoribbons were fabricated using local photocatalysis of graphene sheet by the contact of vertically aligned TiO_2-covered nanopillars and nanowire arrays. AFM and SEM images illustrated formation of the graphene nanomesh with the pore size of 24 nm and neck width of 14 nm and the graphene nanoribbions with the ribbon size of 24 nm and neck width of 12 nm. Quantification analysis on graphene disorder based on Raman spectra confirmed the experimental results. The presented substrate engineering technique allows for a well-controlled periodic modification of graphene and other UV transparent thin films, enabling in perspective the construction of various graphene-based electronic and photonic devices, biosensors and extending the toolbox for studies of 2D materials superlattices.

Thirdly we have achieved large-area fabrication of nanoscale graphene disk and nanomesh arrays, which support plasmon resonances in the near-infrared regime. We have used well-ordered vertically oriented cylinder and monolayer packed sphere morphologies to pattern graphene, and the dipole resonance of the GNDs and GNMs plasmon polaritons has been pushed down to 2.0 μm and 1.7 μm, respectively, which is to our knowledge the smallest value reported for the localized GPP resonance. With some further refinements, our results facilitate graphene plasmons both for fundamental study and for potential applications in the telecommunication window.

Finally, a chemical reaction on graphene was achieved with a nanoporous mask of hexagonal morphology; we have shown that graphene reacts with benzoyl peroxide under intense laser irradiation, producing significant defects in the basal plane. For the first time, we adapted chemical functionalization to the nanoporous mask ne at nano-scale size on top of graphene. Each pore in this case functioned as a nanoreactor for the heterogeneous chemical modification of the graphene at the bottom of the pore. We believe that chemical GALs offer a prospective platform for both fundamental studies of new physical phenomena and applications in revolutionary new devices in such different areas as solid state quantum computing, as thermoelectric components, and even as parallelized biomolecule sensing.

6.2 Scope of Future Work

More experiments for graphene nanostructuring can be performed. The present work can be extended in several ways, as described.

1. Based on the nanostructuring graphene we have already functionalized, comparison on the physical functionalization versus chemical functionalization with graphene nanostructuring patterns can be performed and optimized for different applications such as sensors, OFET and plasmonics.
2. Hetreostructures of graphene and other 2D materials can be made for exploitation with tunable performances in diverse range of applications.

3. Due to the generality of the technique that we have used, the same procedure can be applied to produce nanoscale structures in other 2D materials such as hexagonal Boron Nitride and Transition metal dichalcogenide can have new perspectives for the electronic or plasmonic applications.

Appendix A

A1 Zhongli Wang, Tao Li, Kristoffer Almdal, N. Asger Mortensen, Sanshui Xiao, Sokol Ndoni. Experimental demonstration of graphene plasmons working close to the near-infrared window. Optics Letters. 2016, 41 (22), 5345–5348.

A2 Zhongli Wang, Tao Li, Lars Schulte, Kristoffer Almdal, Sokol Ndoni. Photocatalytic Nanostructuring of Graphene Guided by Block Copolymer Self-Assembly. ACS Appl. Mater. Interface. 2016, 8 (13), 8329–8334.

Appendix B

B1 Sergey Chernyy, Zhongli Wang, Jacob Judas Kain Kirkensgaard, Anders Bakke, Kell Mortensen, Sokol Ndoni, Kristoffer Almdal. Synthesis and Characterization of Ferrocene Containing Block Copolymers. Journal of Polymer Science Part A: Polymer Chemistry. 2017, 55, 495–503.

B2 Tao Li, Zhongli Wang, Lars Schulte, Sokol Ndoni. Substrate Tolerant Direct Block Copolymer Nanolithography. Nanoscale. 2016, 8 (1), 136-140.

B3 Tao Li, Zhongli Wang, Lars Schulte, Ole Hansen, Sokol Ndoni. Fast&Scalable Pattern Transfer via Block Copolymer Nanolithography. RSC Advances. 2015, 5 (124), 102619-102624.

B4 Tao Li, Kaiyu Wu, Tomas Rindzevicius, Zhongli Wang, Lars Schulte, Michael Schmidt, Anja Boisen, Sokol Ndoni. Wafer-Scale Nanopillars Derived from Block Copolymer Lithography for Surface-Enhanced Raman Spectroscopy. ACS Appl. Mater. Interface. 2016, 8 (24), 15668-15675.

B5 Zheng Zhao, Zhongli Wang, Congwu Ge, Xu Zhang, Xiaodi Yang, and Xike Gao. Incorporation of benzothiadiazole into the backbone of 1,2,5,6-naphthalenediimide based copolymers, enabling much improved film crystallinity and charge carrier mobility. Polym. Chem. 2016, 7, 573-579.

Published by:
DTU Nanotech
Department of Micro- and Nanotechnology
Technical University of Denmark
Ørsteds Plads, building 345C
DK-2800 Kgs. Lyngby